Contribution to the mechanical characterization and modelling of knitted NiTi textiles.

François Tissot

THÈSE

Pour obtenir le grade de

DOCTEUR DE LA COMMUNAUTE UNIVERSITE GRENOBLE ALPES

préparée dans le cadre d'une cotutelle entre la *Communauté Université Grenoble Alpes* et la *Czech Technical University in Prague*

Spécialité : **Matériaux, Mécanique, Génie Civil, Electrochimie**

Arrêté ministériel : le 6 janvier 2005 - 7 août 2006

Présentée par

François Tissot

Thèse dirigée par **Denis FAVIER et Miroslav KARLIK**
codirigée par **Yohan PAYAN et Nathanaël CONNESSON**

préparée au sein des **Laboratoires TIMC-IMAG et FZU-ASCR**

dans **les Écoles Doctorales I-MEP2 et**

Contribution à la caractérisation mécanique et à la modélisation des tricots de Nickel-Titane

Thèse soutenue publiquement le **10 Octobre 2016**,
devant le jury composé de :

M, Philippe BOISSE
Professeur, INSA Lyon, Lyon, Fr, Président
M, Tarak BEN-ZINEB
Professeur, Université de Lorraine, Vandoeuvre-lès-Nancy, Fr, Rapporteur
M, Xavier BALANDRAUD
Professeur, SIGMA Clermont, Aubière, Fr, Rapporteur
Mme, Bohdana MARVALOVÁ
Professeur, Technical University of Liberec, Liberec, CZ, Examinateur
M, Petr SITTNER
Professeur, Institute of Physics of the CAS, Prague, CZ, Examinateur
M, Denis Favier
Professeur, COMUE Grenoble-Alpes, Grenoble, Fr, Directeur de thèse
M, Yohan PAYAN
Professeur, CNRS, Grenoble, Fr, Co-Directeur de thèse
M, Nathanael CONNESSON
MC, COMUE Grenoble-Alpes, Grenoble, Fr, Co-Encadrant de thèse
M, Ludek HELLER
Docteur, Institute of Physics of the CAS, Prague, CZ, Co-Encadrant de thèse

To my lovely Krystel' whose support is limitless.

Acknowledgments

I would like to address my deep gratitude to my supervisors Pr. Denis FAVIER and Pr. Yohan PAYAN for you have been patient and wonderful mentors for me. I would also like to express my special appreciation to Dr. Nathanael CONNESSON, you have been a tremendous adviser and helped me handle a lot of issues I encountered during this work. I would like to thank Dr. Ludek HELLER for the exceptional times in Prague in the Institute and outside. Last but not least, I would like to thank Pr. Miroslav KARLIK for the colossal help with all the administration process at Prague University, alongside your fabulous sympathy. I would like to thank my committee members, professor Philippe BOISSE, professor Tarak BEN-ZINEB, professor Xavier BALANDRAUD, professor Bohdana MARVALOVÁ, and professor Petr SITTNER for serving as my committee members. I also want to thank you for letting my defense be an enjoyable moment, and for your brilliant comments and suggestions, thanks to you. I lastly want to address my thankfulness to all members of the team BioMMat (Christopher, Quentin, Edouard, Estephanie, Henrique, Ali, Thierry, Marie, Thierry, and Gregory) and to the whole TIMC-IMAG laboratory in general (you are too many to cite all of you!) for the great moment and the psychological environment provided by your presence and sense of humor. This work was funded by government grant *Presidence UJF* and I would like to thank the Education and Research Ministry and the Grenoble-Alpes University.

A special thanks goes to my family, my parents, brother and sister, who have always pushed me further and been patient after such long scholarship journey. I am also deeply grateful to my friends who were always there even in hardship and for their patience. I would like to thank my musical band mates as music is life and mine would have been meaningless without it, and the time spend with them was, is, and will be exceptional. At last, I would like to express my deepest gratitude and love to my wonderful girlfriend Krystel' who supported me through this work, and has always spent days and nights to help me putting together all my thoughts.

Abstract

Knitting is an ancestral textile manufacturing technique which is still commonly used nowadays. This method allows to manufacture textiles possessing high recoverable strains, an anisotropic mechanical behavior easily tuned by varying the knit loop dimensions, the ability to obtain general forms (preforms) or internal forms (holes) during the manufacturing process, and more, making those textiles particularly attractive and cost-efficient. More recently, the use of Shape Memory Alloys (SMA), notably Nickel-Titanium (Ni-Ti) wires, for producing those textiles allowed to propose textiles with new functional properties, such as very high recoverable strains, shape-shifting effects under temperature changes, high damping capacity, *etc*.

However, such SMA knitted textiles mechanical behavior remains relatively unknown, and even if a certain number of studies have dealt with the knitted textiles mechanical characterization, the application to NiTi knitted textiles remains insufficiently done.

In this work, a set of experimental and numerical tools have been developed to study knitted NiTi textiles deformation, especially to evaluate the influence of material parameters, knit geometry, friction, *etc*., on the mechanical behavior. An experimental setup has been developed to characterize such textiles in biaxial tension. It is inspired by methods developed for soft membranes aiming at obtaining strain fields as uniform as possible in the sample working area. Furthermore, its conception as well as a dedicated image processing software allow measuring boundary forces distributions and knit loops morphology during deformation.

The knitted textile mechanical behavior has been modeled using numerical homogenization method by performing finite elements numerical simulation of a representative knit loop under periodic conditions. Simulations predictions are validated in regard to experimental results obtained on knitted NiTi textiles, in simple tension and biaxial tension in course and wale directions. They are then used to analyze the importance of different deformation mechanisms depending on the loading case studied.

Contents

Acknowledgments **iv**

Abstract **v**

I General Introduction and Objectives **1**
1 Context 1
2 Thesis objectives 1
3 Content 2

II Literature review **3**
1 General presentation of SMA 3
2 Nickel-Titanium Alloys 3
2.1 Phase Transformation in NiTi alloys 3
2.2 Shape Memory Effects 4
2.2.1 One-way shape memory effect 6
2.3 Superelasticity 6
2.4 Elasto-Plasticity 7
2.5 R-Phase 8
3 Knitted textiles 8
3.1 Knitting techniques 9
3.2 General properties of knitted textiles 11
3.3 SMA textiles review 12
4 Experimental and numerical analysis of knitted textiles 14
4.1 Experimental analysis 14
4.1.1 Uniaxial tension 14
4.1.2 Biaxial tension 16
4.1.2.i) *Out-of-plane biaxial tests (bulge test)* 16
Flat specimen 16
Cylinder specimen 16
4.1.2.ii) *In-plane biaxial tests* 17

4.2 Numerical and analytical analysis . . . 18
4.2.1 Analytical analysis . . . 18
4.2.2 Numerical analysis . . . 20
5 Conclusion . . . 21

III Experimental analysis tools **22**
1 Introduction . . . 22
2 Kinematic fields measurement . . . 22
2.1 2D Digital Image Correlation . . . 22
2.2 In-house software for knitted textiles image tracking . . . 25
2.2.1 Displacement field . . . 25
2.2.2 Wire detection and loop geometry . . . 27
2.2.3 Post-processing . . . 28
2.2.3.i) *Dimensional parameters* . . . 28
2.2.3.ii) *Morphological parameters* . . . 28
2.2.3.iii) *Mechanical analysis* . . . 28
2.3 Illustration example . . . 28
3 Method to determine wire friction coefficient . . . 29
4 Biaxial experimental setup . . . 32
4.1 Introduction . . . 32
4.2 Principle of the experimental setup . . . 32
4.3 Experimental setup method . . . 32
4.3.1 Method . . . 33
4.3.2 Definition of measures . . . 34
4.3.2.i) *Spring loads* . . . 34
4.3.2.ii) *Resulting load* . . . 34
4.3.2.iii) *Stresses* . . . 34
4.3.2.iv) *Sample strains* . . . 35
4.3.3 Specimen . . . 36
4.4 Experimental Results . . . 37
4.4.1 Macroscopic behavior . . . 37
4.4.2 Force distributions . . . 37
4.4.3 Comparison of macroscopic strains . . . 39
4.4.4 Strain Fields . . . 40
4.5 Analysis . . . 40
4.5.1 Macroscopic behavior . . . 40
4.5.2 Strain fields . . . 42
4.5.3 Finite Elements model . . . 42
4.5.4 Improvement perspectives . . . 45
4.6 Conclusion . . . 46
5 General conclusion . . . 47

IV Numerical analysis tool **48**
1 Introduction . . . 48
2 Stitch finite elements model . . . 48

2.1 Material Model . . . 49
2.2 Loop geometry and shape parameters . . . 50
2.2.1 Geometry equations . . . 50
2.2.2 Finite elements stitch geometry . . . 51
2.3 Beam finite elements . . . 52
2.3.1 Beam theory . . . 52
2.3.2 Beam finite elements . . . 52
2.4 Periodic boundary conditions . . . 54
2.4.1 3D continuum . . . 54
2.4.2 Application to knit loop model . . . 55
2.5 Contact management and resolution method . . . 57
2.5.1 Implicit resolution method . . . 58
2.5.2 Explicit resolution method . . . 58
2.5.3 Mass scaling and kinetic energy . . . 59
2.6 Conclusion . . . 60

V Knitted NiTi textile characterization **62**
1 Introduction . . . 62
2 Samples . . . 62
2.1 Wire composition and behavior . . . 63
2.2 Knit pattern and representative geometry . . . 65
3 Experimental results . . . 68
3.1 NiTi wires friction coefficient . . . 68
3.2 Uniaxial tension . . . 69
3.2.1 Stress-strain relations . . . 70
3.2.2 Representative loop geometry under loading . . . 71
3.2.3 Boundary force distributions . . . 74
3.3 Biaxial tension . . . 78
3.3.1 Stress-strain relations . . . 78
3.3.2 Representative loop geometry under loading . . . 80
3.3.3 Boundary force distributions . . . 81
4 Numerical simulations . . . 83
4.1 Model parameters . . . 83
4.1.1 Boundary conditions . . . 83
4.1.2 Material behavior models . . . 84
4.2 Uniaxial tension . . . 84
4.2.1 Macroscopic behavior . . . 85
4.2.2 Influence of Young's modulus . . . 88
4.2.3 Influence of friction coefficient . . . 90
4.3 Biaxial tension . . . 91
4.3.1 Macroscopic behavior . . . 92
4.3.2 Influence of Young's modulus . . . 96
4.3.3 Influence of friction coefficient . . . 96
5 General conclusion . . . 97

VI Conclusion & discussion **99**
1 Conclusion and improvements 99
1.1 Conclusion 99
1.2 Improvement perspectives 100
2 Discussion and perspectives 102

Bibliography **103**

List of Figures

II.1 Crystal structure of austenite, martensite, and R-phase for NiTi SMA. 4
II.2 Crystal structure of austenite and martensite (top) and corresponding stress-strain curves (bottom) [1]. 5
II.3 Typical σ versus T diagram of nitinol with stress-temperature loading path to obtain the shape-memory effect or the superelasticity. 5
II.4 Typical stress-strain superelastic behavior of nitinol showing the different phases and characteristic physical quantities. 7
II.5 Typical elasto-plastic mechanical behavior observed in NiTi when $T > T_p$ in the a) Stress-Strain plane, b) Stress-Temperature plane. 8
II.6 Tensile test on NiTi wire (Fort Wayne Metals, NiTi#1) showing A-R transformation. Horizontal axis is expanded before 2% to improve visibility. 9
II.7 Several knit patterns, from simple (left) to complex (right) for both weft knitting (top) and wale knitting (bottom) directions. 10
II.8 Knitting techniques: a) manual hand knitting, b) flat bed semi-automatic machine, c) fully automated flat bed (top) and circular bed (bottom) machines, from [2]. 10
II.9 Mechanical behavior of a jersey knit textile made of 100% acrylic yarns, with two different loop shapes (left and right) (courtesy of Eberhardt (1999) [3]), showing anisotropic behavior and strong dependence to the stitch shape. 12
II.10 Stitch geometry of a stainless steel knitted textile showing shape defects due to the wire plasticity during knitting process. 12
II.11 Theoretical uniaxial tension test (left) and dog-bone specimen (right). 15
II.12 Knit uniaxial tension test devices, reproduced from a) Abel *et al.* (2012) and b) Komatsu *et al.* (2008). 15
II.13 Bulge tests methods on disk specimen (left) and tubular specimen (right). 16
II.14 Bulge test on knitted textile with impermeabilizer, reproduced from Heller *et al.* (2012). 17
II.15 Plane biaxial test - common specimen shapes and grips: a) cruciform [4], b) square with solid grips [5], c) square with point grips [6], and d) square with point grips and pulleys [7, 8]; hatching represents grips. 18

II.16 Analytical models for plain weft knitted textiles from Wada *et al.* (1997) (left) and Araujo *et al.* (2003) (right). 19
II.17 Numerical models from a) Araujo *et al.* (2004), b) Bekisli *et al.* (2009), and c) Demircan *et al.* (2011). 20

III.1 Representation of AOI, Subset, and subset Step used in DIC analysis (left) and representation of subsets center M_i grid 23
III.2 Schematic representation of initial image with initial subset (left) and successive image with tested subset movement (right) 24
III.3 Picture of a tested knitted textile with zoom on wire and a typical subset for knitted textiles (green dash) 25
III.4 A knit loop "hole" (left) and tabular organization of loop labels (right) 26
III.5 Centroid placed in line (left) and three possible centroid architecture (right) 26
III.6 Previous and current position of loops centroid superimposed on previous image . . . 26
III.7 Knit loop singular points and associated loop dimensions (left), and the corresponding segments and singular points in actual textile image (right) 27
III.8 Starting point for wire neutral axis detection and wire segments numbering (left) and circular mask and barycenter of subset for neutral axis detection (right) 28
III.9 Displacement fields, in pixels, obtained by the in-house software (top) and differences with VIC2D measurements, in pixels, (bottom) during uniaxial tensile loading in walewise direction (y) 29
III.10 Principle schematic of the wire friction coefficient measurement device developed. Top: the mobile in the random state within friction cone; Bottom: mobile axis along the friction cone depicted limit angle φ_l and angles notation used to compute friction cone angle φ. 30
III.11 Principle sketch of the setup in initial state. 32
III.12 Pictures of a) the biaxial tensile machine with experiment set up and the two cameras "Cam0" and "Cam1", b) "Cam0" picture, and c) linkage and associated target design. 33
III.13 Notations and labels used in the experimental setup. 35
III.14 Monotonic unixial test data of silicone and identification of a Neo-Hookean behavior model. 36
III.15 a) Grips displacement (left scale) and resulting reaction forces (right scale), b) Stress/strain macroscopic behavior. 37
III.16 Normal forces along specimen boundaries with 19 springs. A: $\epsilon^E_{max} = 9\%$, B: $\epsilon^E_{max} = 17.5\%$, C: $\epsilon^E_{max} = 26\%$, D: $\epsilon^E_{max} = 35\%$. 38
III.17 Tangential forces along specimen boundaries with 19 springs. A: $\epsilon^E_{max} = 9\%$, B: $\epsilon^E_{max} = 17.5\%$, C: $\epsilon^E_{max} = 26\%$, D: $\epsilon^E_{max} = 35\%$. 38
III.18 Ratio of tangential over normal springs forces on sample boundaries. A: $\epsilon^E_{max} = 9\%$, B: $\epsilon^E_{max} = 17.5\%$, C: $\epsilon^E_{max} = 26\%$, D: $\epsilon^E_{max} = 35\%$. 39
III.19 a) Comparison of macroscopic strains measurements and b) stress/strain relations calculated from grip measured forces and summed spring forces. 40
III.20 i, ii, and iii) Strain field components (%), iv) absolute difference of the strain field components ϵ_{xx} and ϵ_{yy} (%), v) normalized absolute difference of the strain field components. A: $\epsilon^E_{max} = 9\%$, B: $\epsilon^E_{max} = 17.5\%$, C: $\epsilon^E_{max} = 26\%$, D: $\epsilon^E_{max} = 35\%$. . . 41

III.21 Geometry of finite elements models with a) experimental hooks disposition and b) ideal hooks disposition. 42
III.22 Comparison of stress/strain relations between experiment and FE model with experimental hooks disposition. 43
III.23 Comparison of spring normal forces between experiment (symbols), FE model with experimental hooks disposition (solid lines), and FE model with ideal hooks disposition (dash lines). A: $\epsilon^E_{max} = 9\%$, B: $\epsilon^E_{max} = 17.5\%$, C: $\epsilon^E_{max} = 26\%$, D: $\epsilon^E_{max} = 35\%$. 44
III.24 Comparison of macroscopic strains calculations using the FE model with ideal hooks placement. 44
III.25 Strain field components (%) for the finite element model with experimental hooks disposition. A: $\epsilon^E_{max} = 9\%$, B: $\epsilon^E_{max} = 17.5\%$, C: $\epsilon^E_{max} = 26\%$, D: $\epsilon^E_{max} = 35\%$. . . 45
III.26 Strain field components (%) and normalized absolute difference of the strain field components for the finite element model with ideal hooks disposition. A: $\epsilon^E_{max} = 9\%$, B: $\epsilon^E_{max} = 17.5\%$, C: $\epsilon^E_{max} = 26\%$, D: $\epsilon^E_{max} = 35\%$. 46

IV.1 Aurrichio behavior model used to model the NiTi superelastic-plastic mechanical behavior. 49
IV.2 Left: Multiple repeating unit cell of a knit loop (red & green) or cut unit cell (dash squares); Right: Knit loop geometry and shape parameters 50
IV.3 Creation of the finite elements model knit loop geometry and reference points for periodic boundary conditions. 51
IV.4 Schematization of initial (left) and deformed (right) beam according to Euler-Bernoulli (top) and Timoshenko (bottom) 52
IV.5 Beam bending benchmark performed to compare beam finite elements and standard 3D brick elements. 53
IV.6 Illustration of the integration points organization and numbering in the section using default 3x8 integration (left) and user-defined 9x8 integration points (e_r x e_θ) (right) 53
IV.7 Bending moment versus curvature using 3x8 (red dash), 9x8 (green crosses), and 15x8 (blue line) integration points along $\vec{e_r}$ and $\vec{e_\theta}$ respectively. 54
IV.8 Repetition of a 2D periodic pattern in initial state (a), and in any deformed state (b) [9] 54
IV.9 Representation of a cubic volume and corresponding points pair for periodic boundary conditions 55
IV.10 Knit loop model presenting boundary points and master nodes E and F. 56
IV.11 Illustration of the contact management between a node and a beam element in Abaqus using implicit resolution method. 58
IV.12 Illustration of contact management between beam finite elements using explicit resolution method. 59
IV.13 Kinetic energy (top) and reaction force at the beam free end (bottom) for different values of material damping. 60

V.1 Simple tensile test of a NiTi wire, composition of 50.8 at% Ni and $\varnothing 0.1$ mm diameter (Fort Wayne Metals, NiTi#1) 63
V.2 Knitted NiTi textile set-up in the biaxial tensile test experimental apparatus 64
V.3 Springs placement in the wale direction and symmetry defect due to the knit loop wire curvature. 64

V.4 Knit loop dimensional parameters. 65
V.5 Distribution maps of knit loop dimensions L, H, and d_y in the initial state (left) and population distributions and gaussian fit with mean value and standard deviation (right) 66
V.6 Distribution maps of knit loop widths W_1 and W_2 in the initial state (left) and population distribution and gaussian fit with mean value and standard deviation (right) . . 67
V.7 Distribution maps of knit loop opening $\alpha_1 + \alpha_2$ and warping $\alpha_1 - \alpha_2$ in the initial state (left) and population distribution and gaussian fit with mean value and standard deviation (right) 68
V.8 Initial geometry identified on experimental picture created using parametric equations presented in Chapter 2.2 69
V.9 Total friction cone angle measurement between two nitinol wires plotted versus time 69
V.10 Demi-friction cone angle obtained with a set of three measurements, mean value $\phi_m = 0.186\ rad$ and a standard deviation $\sigma = 0.016\ rad$ 70
V.11 Mechanical behavior of knitted NiTi textile in uniaxial tension; lineic force - axial strain relations (top), and transversal strain - axial strain (bottom) 71
V.12 Loop dimensions variations during loading cycles in wale-wise tension 72
V.13 Loop dimensions variations during loading cycles in course-wise tension 72
V.14 Deformation of a random knit loop during wale-wise tensile loading (top) and course-wise tensile loading (bottom) 73
V.15 Correspondence between global area of interest strains and local loops dimensions variations in wale-wise tension (top) and course-wise tension (bottom) 74
V.16 Schematic representation of the ZoI deformed shape in uniaxial tension. 75
V.17 Boundary forces measurement along edges E1 (top) and E4 (bottom) during wale-wise tension, normal component N is on the left side, and tangent component T on the right side; Values are given at strain increments A, B, C, and D 75
V.18 Tangent component T over normal component N ratio (in %) along edges E1 (left) and E4 (right) during wale-wise tension; Values are given at strain increments A, B, C, and D 76
V.19 Boundary forces measurement along edges E1 (top) and E4 (bottom) during course-wise tension, normal component N is on the left side, and tangent component T on the right side; Values are given at strain increments A, B, C, and D 77
V.20 Tangent component T over normal component N ratio (in %) along edges E1 (left) and E4 (right) during course-wise tension; Values are given at strain increments A, B, C, and D 77
V.21 Representation of the textile working area (green outline) and Zone of Interest (ZoI - orange outline) 78
V.22 Strains measurements of the sample working area (lines) and ZoI (symbols) in principal directions. 79
V.23 Macroscopic behavior of the sample ZoI in force (left scale, lines) and strains (right scale, symbols) in time. 79
V.24 Loop dimension variations during loading cycles in biaxial tension 80
V.25 Correspondence between global area of interest strains and local loops dimensions variations in biaxial tension 81

V.26 Boundary forces measurement along edges E1 (top) and E4 (bottom) during biaxial tension, normal component N is on the left side, and tangent component T on the right side; Values are given at strain increments A, B, C, and D 82
V.27 Ratio of tangent component T over normal component N (in %) along edges E1 (left) and E4 (right) during biaxial tension; Values are given at strain increments A, B, C, and D 82
V.28 Initial geometry identified on experimental picture created using parametric equations presented in Chapter 2.2 83
V.29 Loading steps for the finite elements model depending on the tensile direction. 84
V.30 Material behavior models used in the numerical analysis using a linear elastic material (red) and Aurrichio model (blue dash) fitted on wire tension experimental results (black). 85
V.31 Comparison between FE model and experimental results in uniaxial wale-wise tension using simple elastic material model. 86
V.32 Comparison between linear elastic (triangles) and superelastic (asterisks) material behavior models with experimental results (lines) in uniaxial wale-wise tension. 87
V.33 Comparison between FE model and experimental results in uniaxial course-wise tension using simple elastic material model. 88
V.34 Comparison between linear elastic (diamonds) and superelastic (crosses) material behavior models with experimental results (lines) in uniaxial course-wise tension. . . . 89
V.35 Maximum mises stress (top) and contact pressure (bottom) in the wire section along normalized curvilinear abscissa between points M_4 and M_2 (left) and points M_1' and M_4' (right) using linear elastic material during uniaxial wale-wise tension at strains increments A, B, C, and D. 89
V.36 Maximum mises stress (top) and contact pressure (bottom) in the wire section along normalized curvilinear abscissa between points M_4 and M_2 (left) and points M_1' and M_4' (right) using linear elastic material during uniaxial course-wise tension at strains increments A, B, C, and D. 90
V.37 Influence of Young's modulus on the mechanical behavior of the knit loop in wale-wise tension. 91
V.38 Influence of Young's modulus on the mechanical behavior of the knit loop in course-wise tension. 92
V.39 Influence of the wire friction coefficient on the knit loop mechanical behavior in wale-wise tension. 93
V.40 Influence of the wire friction coefficient on the knit loop mechanical behavior in course-wise tension. 94
V.41 Comparison between experimental (lines) and numerical lineic forces using linear elastic material (asterisks) during a biaxial loading cycle. 94
V.42 Comparison between experimental (lines) and numerical lineic forces using linear elastic material (asterisks) and superelastic material (circles) during a biaxial loading cycle. 95
V.43 Maximum mises stress (top) and contact pressure (bottom) in the wire section along normalized curvilinear abscissa between points M_4 and M_2 (left) and points M_1' and M_4' (right) using superelastic material during biaxial tension at strains increments A, B, C, and D. 95

V.44 Influence of Young's modulus on the lineic forces response of the knit loop in biaxial tension. 96
V.45 Influence of the wire friction coefficient on the knit loop lineic forces response in biaxial tension. 97

CHAPTER

I General Introduction and Objectives

1 Context

Textiles are present in a large number of industrial applications, from composites materials industry to individual protection equipment, including the biomedical field (prostheses, ortheses, sensors, *etc*.). Knitting textiles in particular have seen their applications field widen due to their particular mechanical properties and their easy manufacturing.

Common woven textiles possess, schematically, the same mechanical behavior as their constitutive wires when loaded along their weaving axis (weft and warp). Knitted textiles, however, show a mechanical behavior drastically different from the constitutive wire due to the undulating shape of the wire and the high mobility of the latter within the textile. This induces large recoverable strains for small local strains, allowing to use stiff elastic material such as stainless steel, for example. Furthermore, this high mobility induces friction between knit loops which confers the textile with significant damping capacity. Finally, the internal knitted morphology provides the textile with anisotropic mechanical behavior which can be finely tuned by adapting the knit loop geometry. The knitted textiles mechanical properties allow to consider knitted textiles as excellent candidates for biomimetic materials production.

Recently, Shape Memory Alloys (SMA) wires have been used to produce textiles possessing enhanced or new mechanical properties and capacities. Thus, knitted textiles produced from Nickel-Titanium (NiTi) wires have been created to propose textiles possessing large recoverable strains (greater than 50%). The NiTi alloy also possesses an intrinsic damping capacity, which adds to the natural damping capacity of the knitted textile. The NiTi mechanical behavior dependence on temperature confers this textile the capacity to ajust its mechanical behavior to the temperature it is subjected to, or even to change shape to create an actuator.

2 Thesis objectives

In order to develop industrial applications for knitted NiTi textiles, it is inevitable to fully understand and to be able to analyze numerically their mechanical behavior. Many studies have been performed on the NiTi alloy to propose several material behavior models. The model proposed by Aurrichio is commonly used nowadays. Knitted textiles, in a general way, have also been

studied in a certain number of studies, which propose experimental or analytical and numerical approaches to study their mechanical behavior.

However, few studies dealt with knitted NiTi textiles. Few methods mixing experimental analysis and numerical have been proposed, and those methods are usually limited to study the textiles macroscopic mechanical behavior.

In order to characterize these particular NiTi textiles mechanical behavior, a complete characterization method is proposed. This method also provide means to determine a knitted NiTi textiles properties (knit loop dimensions, wire diameter and properties, *etc.*) depending on the application desired.

3 Content

In Chapter II, the shape memory alloy Nickel-Titanium is presented to provide the reader with the base knowledge linked to this alloy specific material behavior. A summary regarding knitted textiles, their specific properties as well as the state of the art about SMA textiles is drawn. The chapter is concluded by the state of the art on the experimental and analytical and numerical characterization techniques for knitted textiles.

Chapter III presents the experimental characterization method developed to study knitted NiTi textiles and a jersey-type knit. The method is composed of an image processing software, allowing to measure kinematic fields within the sample zone of interest, as well as computing at each time the knitted textile loop morphology. A wire-to-wire friction coefficient measurement method is then presented in order to characterize the impact of friction on the textile mechanical behavior. Finally, a biaxial testing setup is presented, providing a strain field as uniform as possible within the sample, together with the ability to perform direct boundary conditions measurement applied to the sample. The system ability to provide uniform strain field is studied on soft isotropic membranes, and the boundary conditions measurement precision is discussed.

The numerical analysis method for knitted NiTi textiles is then presented in Chapter IV. This method is inspired by different methods presented in literature. Beam elements are used to model the thin wire, and periodic boundary conditions are used to simulate the strain field within the sample zone of interest. Encountered difficulties and hints used for successful model implementation are discussed at the chapter end.

In Chapter V, the methodology previously presented is applied to a knitted NiTi textile sample. The wire mechanical behavior is first studied, then the textile knit loop representative geometry is computed in the initial state to feed the numerical model. The textile is then experimentally characterized in uniaxial and biaxial tension, and the change in knit loop representative geometry dimensions are studied during loading thanks to the dedicated image processing software. The loading case performed experimentally are numerically modeled and the macroscopic behavior obtained is compared with experimental results to validate the method. The model is finally used to study the influence of various material parameters on the textile macroscopic behavior. Critics are ventured afterward regarding the results obtained and errors related to the characterization method.

CHAPTER

II Literature review

1 General presentation of SMA

In the first half of the 20th century, Swedish chemist Arne Oländer discovered that the gold-cadmium (Au-Cd) alloy possesses the particularity to be able to recover its original shape after permanent deformation by heating the material above a characteristic temperature T_c. Later on, other alloys are discovered with the same shape recovery property. This shape recovery property gave the name Shape Memory Alloys (SMA) to this class of metallic alloys.

SMAs possess a second particular property, namely superelastic behavior. Those two properties are consequences of the material phase transformation at solid state between two stable phases, called the *martensitic transformation*. The first phase is the austenite phase α, stable above the characteristic temperature T_c. The second phase is the martensite phase β, stable below T_c.

To trigger such transformation, temperature or stress changes are required. The transformation from martensite to austenite is performed by heating the material from an initial temperature $T_0 \leq T_c$ to a final temperature $T_f \geq T_c$. This transformation triggers the shape memory effect.

The transformation from austenite to martensite is obtained in two ways, when starting with the material with an initial temperature above T_c: upon cooling the material to a final temperature lower than T_c, or upon applying stress to the material. In the second case, the martensitic phase created is called Stress Induced Martensite (SIM), and is conveniently oriented compared to the applied stress. During such loading, the particular mechanical response of the alloy is observed.

2 Nickel-Titanium Alloys

2.1 Phase Transformation in NiTi alloys

In this paragraph, phase transformation mechanism will be explained in a simple way. For more detailed lectures about SMA and phase transformation, the reader is invited to refer to literature [10–14].

The most used SMA is the near equiatomic Nickel-Titanium alloy (NiTi). In NiTi, the austenite phase is an ordered cubic centered crystalline structure B2 of high symmetry, while the martensite is a phase with monoclinic structure B19' of lower symmetry (Figure II.1). Given that atoms

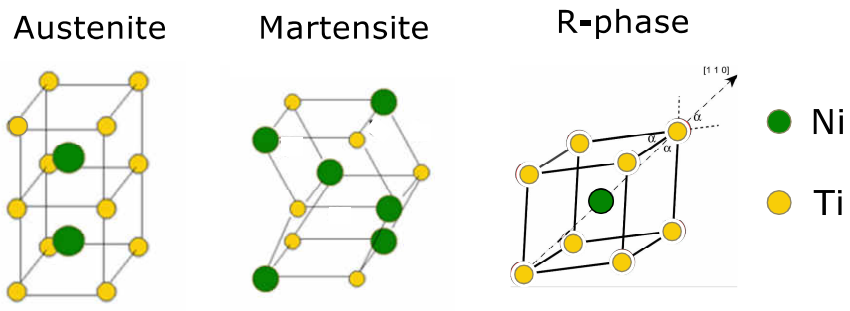

Figure II.1. Crystal structure of austenite, martensite, and R-phase for NiTi SMA.

move in an highly coordinated and cooperative way and without diffusion, a particular atom always retains its neighborhood. This neighborhood is also conserved when martensite transforms back to the parent phase. Each atom returns back exactly where it was before the first transformation, and the shape is thus retained. This deformation is derived from a change in lattice shape, thus the maximum strain can be calculated for each transformation in ideal single crystals. Wires in tension can reversibly deform up to 10%. In polycrystals, grains orientation and texture come into play thus influencing maximum reachable strain in a specific direction.

Figure II.1 represents the NiTi phases and their respective atomic structures, and Figure II.2 represents these structures depending on the thermomechanical loading applied. The phase transformation can be triggered either by temperature or stress changes. During thermal cycling, the transformation from austenite to martensite (A-M) starts at M_s and ends at M_f. Similarly, the transformation from martensite to austenite (M-A) starts at A_s and ends at A_f.

At a temperature below M_f, the material presents a pseudoplastic mechanical behavior, and if heated above A_f after releasing the load, the material presents the *shape memory effect* (Figure II.2, bottom i)). When a mechanical loading is applied at a temperature above A_f, the transformation A-M starts at a critical stress $\sigma_{Ms} < \sigma_p$, and the *superelasticity* is observed (Figure II.2, bottom ii)). The temperature T_p corresponds to the temperature at which the transformation stress σ_{Ms} equals the yield stress σ_p. At such temperature and above, the plastic flow of austenite occurs before transformation, and an *elastoplastic* mechanical behavior is observed (Figure II.2, bottom iii)).

Those three mechanical behaviors and their respective mechanisms are briefly described in following paragraphs 2.2, 2.3, and 2.4.

2.2 Shape Memory Effects

There are two categories of shape memory effect:

- One-way shape memory effect
- Two-way shape memory effect

The two-way shape-memory effect is not presented in this thesis, and the reader is encouraged to refer to literature for further reading on this shape memory effect [15].

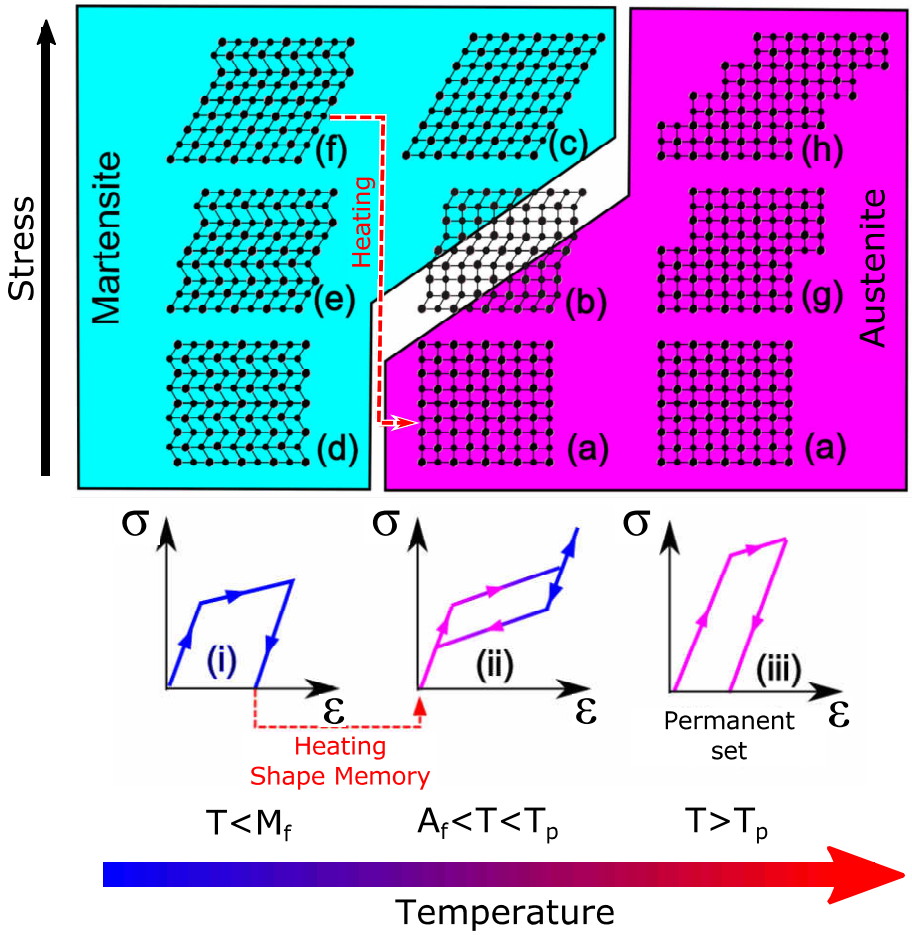

Figure II.2. Crystal structure of austenite and martensite (top) and corresponding stress-strain curves (bottom) [1].

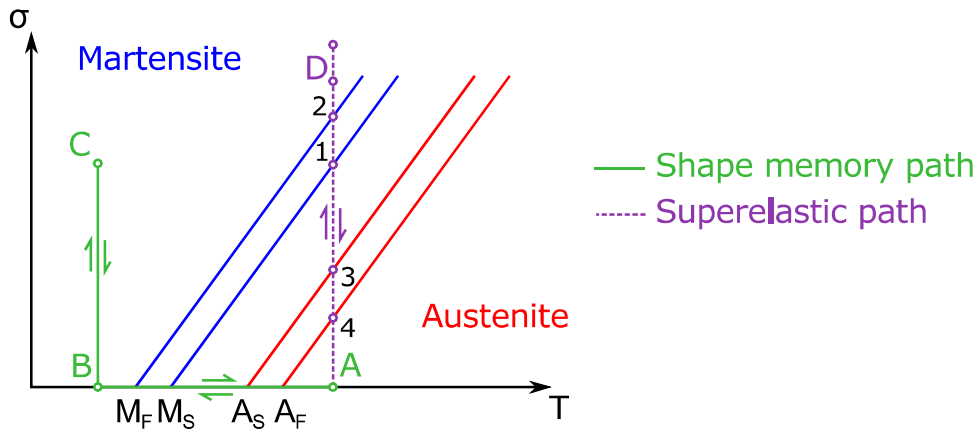

Figure II.3. Typical σ versus T diagram of nitinol with stress-temperature loading path to obtain the shape-memory effect or the superelasticity.

2.2.1 One-way shape memory effect

This effect can be observed after a particular loading on the alloy decomposed in three sequences (Figure II.3):

- A-B: Zero stress cooling ($\sigma = 0$) from an initial temperature $T_i > A_F$ to a final temperature $T_f < M_F$
- B-C-B: Loading and unloading involving residual strain at constant temperature $T_f < M_F$
- B-A: Heating back to a temperature $T > A_F$ at zero stress ($\sigma = 0$)

During the mechanical loading of the material in the second step, the SMA behaves like a standard metallic alloy, with mechanical characteristics corresponding to those of the martensite itself. The loading is composed of a linear part up to the yield stress (σ_e). Detwinning then happens, and a residual strain is observed upon removing the load.

The one-way shape memory effect is observed for a thermomechanical loading corresponding to the previous sequence A-B + B-C-B + B-A (Figure II.3). During the first sequence, martensite is formed, but the transformation strain is null. During the second sequence, no transformation is observed but a reorientation of martensite variants formed during cooling, going along with a residual strain. In the last sequence, the crystalline network returns to the associated austenitic state, and as no slip of atomic plane occurs during twinning of martensite, the parent shape is recovered.

The term one-way shape memory effect comes from the fact that a mechanical loading is necessary to induce the residual strain in the martensitic state, to be recovered later upon heating.

2.3 Superelasticity

The second remarkable property of SMA after shape memory effect is the superelasticity. Unlike other metallic alloys, SMA exhibits a large recoverable strain of up to 10% in tension, *i.e.* 40 times greater than most steel based alloys. This effect is derived from, like the shape memory effect, the phase transformation between martensite and austenite. This property may yet be observed only during mechanical loading at high temperature, *i.e.* at $T > A_F$, while for shape memory effect, the alloy must be mechanically loaded at low temperature ($T < M_F$).

To observe such mechanical behavior, the material must first be heated to a temperature $T > A_F$ at zero stress. While keeping constant temperature, a loading/unloading mechanical cycle can be applied to the material. The relation between stress and strain will present three remarkable sequences corresponding to the following sequences of the stress-temperature diagram (Figure II.3):

- A-1 : austenitic phase elasticity
- 1-2 : transformation from austenite to martensite
- 2-D : martensitic phase elasticity and plasticity (after reaching point D)

And three similar sequences are found upon unloading, namely sequence D-3 (martensite elasticity), sequence 3-4 (reverse phase transformation), and sequence 4-A (austenite elasticity).

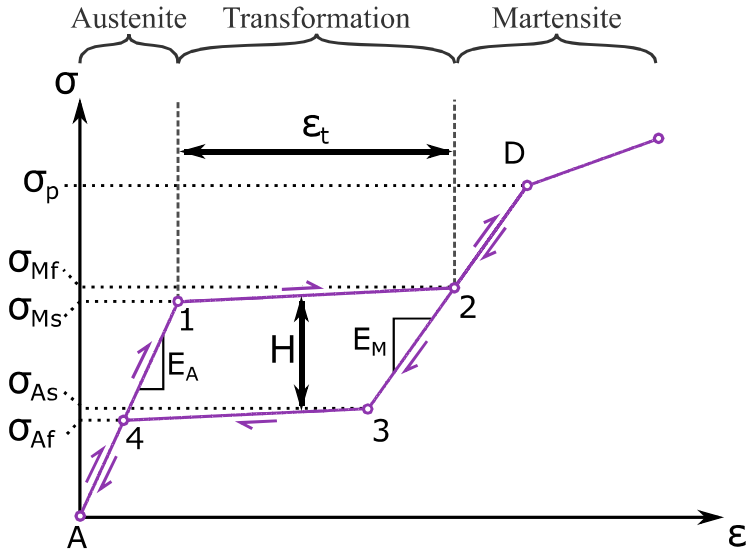

Figure II.4. Typical stress-strain superelastic behavior of nitinol showing the different phases and characteristic physical quantities.

A schematic representation of SMA superelastic mechanical response, depicting the three steps presented above, is given in Figure II.4. From such mechanical behavior, it is possible to calculate a set of parameters that defines the superelastic behavior, namely:

- σ_{Ms}: stress at which the austenite to martensite transformation starts
- σ_{Mf}: stress at which the austenite to martensite transformation finishes
- σ_{As}: stress at which the martensite to austenite transformation starts
- σ_{Af}: stress at which the martensite to austenite transformation finishes
- E_A: Young's modulus of austenite
- E_M: Young's modulus of martensite
- ϵ_t: transformation strain
- H: mechanical hysteresis, computed as $\sigma_{Ms} - \sigma_{As}$ (or $\sigma_{Mf} - \sigma_{Af}$)

During unloading, the curve is similar to that of loading, noting only a mechanical hysteresis H, generally with a magnitude about 300 MPa for nickel-titanium alloys. It is worth noting that the transformation from austenite to martensite and the reverse transformation happens under the effect of applied stresses. The martensitic phase induced in that case is known as Stress Induced Martensite (SIM).

2.4 Elasto-Plasticity

When the alloy is mechanically loaded at an initial temperature $T_i > T_p$, the material is in the austenitic phase. As the loading carried, the normal stress first reaches the yield stress σ_e before the transformation stress σ_{Ms}. Hence, the plastic flow of the austenite occurs before the transformation A-M, and a typical elasto-plastic behavior is observed (Figure II.5).

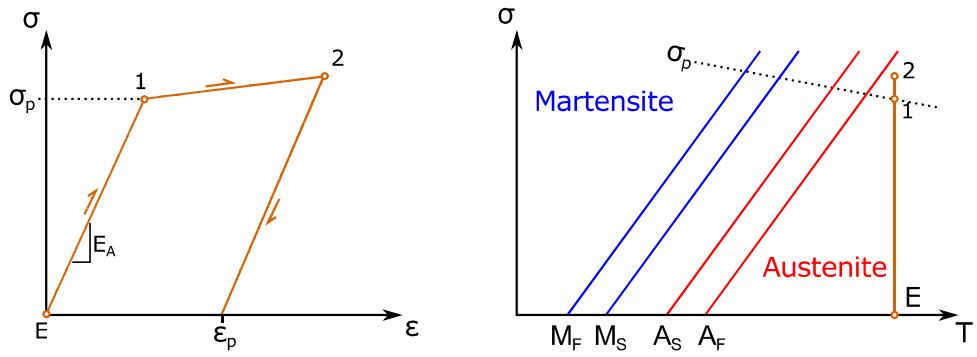

Figure II.5. Typical elasto-plastic mechanical behavior observed in NiTi when $T > T_p$ in the a) Stress-Strain plane, b) Stress-Temperature plane.

After releasing the load on the material, permanent strain remains and can not be recovered by heating.

2.5 R-Phase

A third phase may be induced in NiTi alloys during a thermomechanical loading. This phase is called the R-phase as it was initially thought to have a rhomboedric crystalline structure. This phase is, in fact, triclinic and originates from a distortion of the austenite along a diagonal (Figure II.1) [16].

This phase is observed in certain alloys depending on its chemical composition and the temperature of the test.

In such state, the mechanical behavior is very similar to that presented in paragraph 2.3, with however a first transformation plateau of small strain amplitude which appears during the elastic deformation of austenite (Figure II.6). Hence, a first elastic slope is observed, with an elastic module corresponding to that of the austenite (E_A, Figure II.6 green dash line). Then, the austenite is transformed into the R-phase at low stresses. A second elastic slope is then observed after complete transformation of the austenite with an elastic modulus of the R-phase (E_R, Figure II.6 blue dash line) corresponding to the elastic deformation of the R-phase. Once the transformation stress σ_{Ms} is reached, the R-phase transforms into martensite, and the material then behaves as described in the previous paragraph.

During unloading, the martensite phase may, in some cases, transform back into R-phase, or simply transform to austenite, completely skipping the R-phase. This transformation path during unloading depends on the chemical composition and material heat-treatment.

3 Knitted textiles

Knitted textiles are obtained with a unique wire interlocking with itself in a looping manner, opposing woven textiles which are obtained from a large amount of yarn bundles running from one side to another and cut. In this section, knitting techniques, general properties of knitted textiles and a few SMA textiles applications will be reviewed. For a detailed lecture on knitted textiles and relative technologies, the reader is invited to refer to books from Horrocks A. & Anand S. (2000) [17] and D. Spencer (2001) [2].

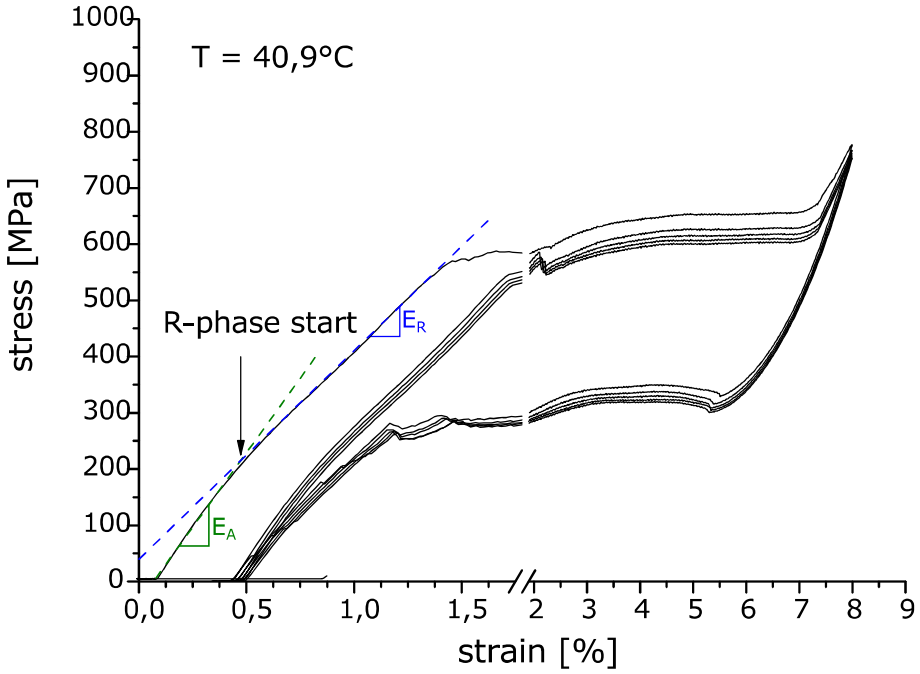

Figure II.6. Tensile test on NiTi wire (Fort Wayne Metals, NiTi#1) showing A-R transformation. Horizontal axis is expanded before 2% to improve visibility.

3.1 Knitting techniques

There exists a wide variety of interlocking patterns to create a knitted textile, from the most simple loop structure ("jersey" type) to more complex shapes (laid-in structure, interlocked warp knit, *etc.*) (Figure II.7) [2, 17, 18]. Complex three-dimensional shapes can also be obtained from specialized knitting patterns [19]. There are two specific directions in knitted textiles, namely course and wale.

To obtain such textiles, there exist three main knitting techniques, from the most ancient to most recent: i) manual needle knitting, ii) knitting bench, and iii) automatized knitting machine.

The first technique is the most basic and most commonly known (Figure II.8a). Two needles (the sinker and the jack) are manually handled to intertwine wires and to form loops. This technique allows obtaining easily simple loop shapes, but may also produce complex shapes, such as 3D volumes (clothes).

Knitting bench uses the manual needles technique semi-automatized (Figure II.8b). A succession of hooks and needles placed face to face on each side of the machine allows to grasp the wire as it passes by in the trolley. This technique is referred as semi-automatic as the trolley is moved back and forth manually by the operator. Each time the trolley completes a length, a row (course) is completed, and the next row will be one step above (wale).

Thanks to past centuries industrialization and automation, industrial knitting machines have appeared (Figure II.8c).Thus, machines dedicated to forming tubular knit structures of infinite length and constant diameter have been created. For flat knit structures, flat bed machines have been created to perform knitting row by row (course), making it possible to vary each course length to obtain non-square textiles.

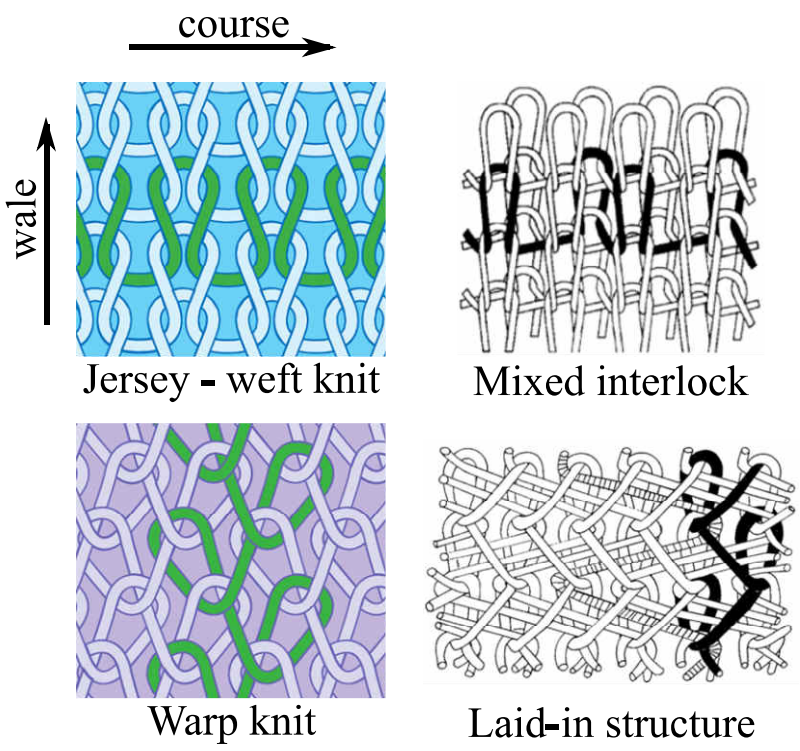

Figure II.7. Several knit patterns, from simple (left) to complex (right) for both weft knitting (top) and wale knitting (bottom) directions.

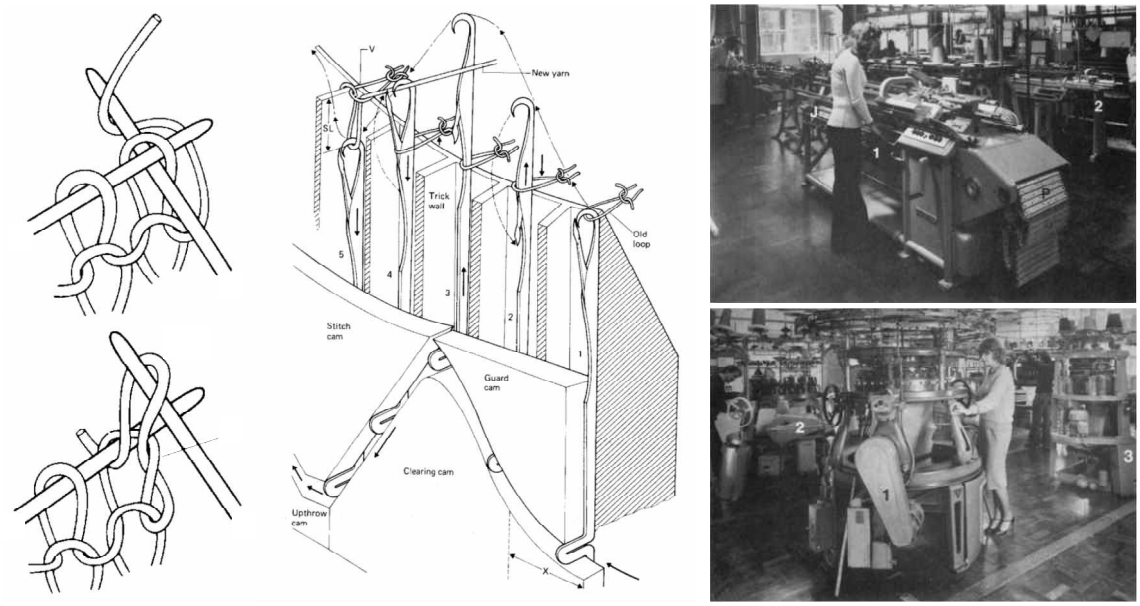

Figure II.8. Knitting techniques: a) manual hand knitting, b) flat bed semi-automatic machine, c) fully automated flat bed (top) and circular bed (bottom) machines, from [2].

3.2 General properties of knitted textiles

Due to their particular inner structure, knitted textiles possess a wide variety of properties specific to that kind of structure. The first remarkable property is the large recoverable strain during uniaxial tensile loading. Using standard steel wires to manufacture a jersey knit sample, Heller *et al.* [20] shows that such textile exhibits recoverable up to 20%, while the wire possesses only 0.2% elastic strain. This large recoverable strain arises from the knit loops high mobility against each other, leading to a ratio of local maximum strain to global maximum strain comprised between 1/5 and 1/50 approximately. Furthermore, from this high internal mobility arises another interesting property, namely damping. The large stress hysteresis, added to the natural material hysteresis, provides energy dissipation during loading/unloading cycles [21]. The movement between course rows induces wire to wire friction, affecting directly the damping efficiency of the textile. Finally, the textile internal mobility allows for high formability, *i.e.* such textile can comply with non-uniform surfaces such as organs, bones and articulations, composites molds, *etc.* [22–25]. This property is particularly interesting for composites where the reinforcement formability is one of the crucial problems encountered with woven textiles where corners and sharp edges show high local stresses and shape defects [24, 26–29].

The knit structure is also highly porous, *i.e.* large air volumes are present within the textile which provides the textile with low density. For example, the low density allows for light construction panels [22]. For another example, porosity also improves biomedical applications of knitted textiles as it allows for cell ingrowth in and around the implant, to increase cohesion between implant and surrounding tissues and the healing process in the case of scaffold [25, 30]. In this context, porosity also allows for body fluids to flow through the implant as it would in porous bones or organs, increasing the implant osteointegration [25, 31]. The textile porosity is also primordial when used as composite reinforcements, as the matrix material is able to flow easily through the textile. This tends notably to decrease the risk of air cavity defects often found with woven reinforcements. Finally, the fabric porosity induces a quasi absence of compression resistance, allowing such textile to be fitted in small cavities and used as filler if needed.

Another knitted textile characteristic to be mentioned is the mechanical anisotropy, as presented in Figure II.9. This property refers to the loading curves differences when unaxially loading the sample in its principal directions, namely course and wale directions.

Further advantage of knitted textiles is the wide range of mechanical behavior available simply by tuning the knit loop dimensions, or directly changing the knit pattern. This characteristic allows for high flexibility of applications fields.

Due to the manufacturing process of knitted textiles, it is also possible to directly preform specific shapes within the fabric, for example holes can be knitted directly during the fabrication process, removing unraveling defects when internal shapes are cut inside the fabric, in the case of woven fabrics for example. This advantage also implies that no secondary fabrication steps are required to create such cuts, and therefore reduces manufacturing costs.

Yet unraveling is a major drawback to knitted textiles due to the fact that the fabric consists in a single wire being interlocked with itself. A single cut can lead to a complete textile disintegration.

Furthermore, during knitting process, it has been shown that high local strains are induced within the wire [32]. This implies loop shape defects and non-uniformity when a low elastic strain wire is used, such as stainless steel wire (Figure II.10).

Finally, it has been found that knitted textiles porosity may lead to adhesion problems in some

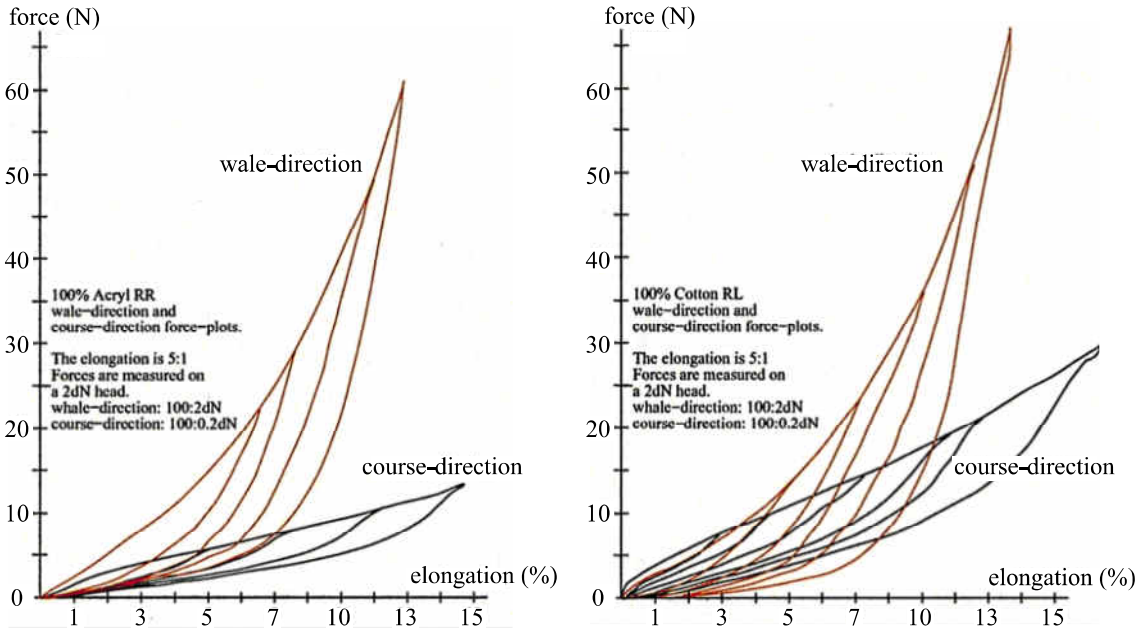

Figure II.9. Mechanical behavior of a jersey knit textile made of 100% acrylic yarns, with two different loop shapes (left and right) (courtesy of Eberhardt (1999) [3]), showing anisotropic behavior and strong dependence to the stitch shape.

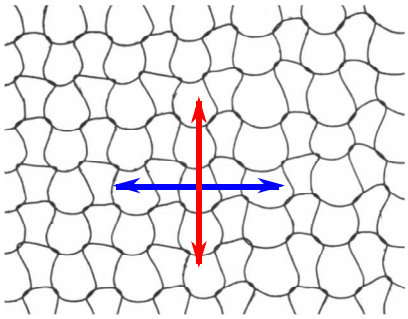

Figure II.10. Stitch geometry of a stainless steel knitted textile showing shape defects due to the wire plasticity during knitting process.

biomedical applications, as in the case of anterior crucial ligament scaffolds [25]. To overcome such cohesion problems, in this particular case, the wire has been replaced by microfibers yarns that, due to the rough surface of the yarn, provides better adhesion with surrounding tissues.

3.3 SMA textiles review

From a general point of view, textiles using shape memory alloys are few and concealed to relatively specific field of applications. Yvonne Chan thesis work [33] has established an exhaustive list of several SMA usages in textiles, mostly oriented toward interior decoration elements and aesthetics aspects those wires can provide [34–36]. Yet often, those textiles are restrained to standard textiles (polymer yarns, cotton or wool fiber yarns, *etc.*) with SMA wires inserted in-between and not directly integrating SMA wires into textile patterns. SMA wires integrated into textiles improve or create new properties, such as increased damping and impact resistance [37–40], shape memory and wrinkle recovery capabilities triggered by temperature change or SMA superelasticity [35, 41–45], or increased fabric stiffness [20], to name a few.

SMA knitted textiles have yet been proposed or are currently used for few specific applications, and some of them are presented thereafter. In the biomedical field, knitted nitinol stents have been produced and studied for external veins reinforcement [46, 47]. A tubular spiral knit can be easily manufactured with knitting machines presented in Section 3.1 with a SMA wire, and uses the specific properties of knitted textiles to match the mechanical behavior of the patient artery (anisotropy, non-linear response, *etc.*). Furthermore, it is known that every tissue in every patient behaves differently, and therefore implants may need to be tuned to the desired behavior easily, without the need of a broad set of stents with distinct dimensions. SMA knitted stents uses the shape setting capability of knitted SMA textiles to allow preforming stents to the corresponding behavior and implant size, making it a cost efficient solution. A similar product is proposed for esophageal closure pathology [48] and is obtained from a tubular knitted stent wrapped in a fabric cover (Ultraflex stent, Boston Scientific).

Still in the biomedical field, a multimaterial internal vein stent has been proposed by Tokuda *et al.* [49]. The stent is knitted in a spiral tubular motion, as previously presented stents, from two distinct wires at the same time, alternate one knit row to the other (wale direction, tube axis). The first material is a nitinol wire, and the second a bioresorbable polyparaphenylene-benzobisoxazole (PBO) multifilament fiber. The nitinol wire provides superelasticity, as in standard nitinol stents for their insertion into small catheters. The catheter is then introduced through the patient femoral artery usually, up to the delivery point where the stent is released from the catheter. The superelasticity returns the stent back to its original shape, opening the previously closed artery. During the artery healing process, the PBO wire degrades, and its degradation time is tuned to the healing time. This lead to a fully degraded wire after the healing is complete, leaving only a free nitinol filament to be removed from the patient artery, reducing drastically post-operative complications.

In another field, knitted NiTi textiles have been proposed as the response for high stroke contractile actuators, yet light, small, simple and cost-efficient [50]. Most hydraulic, magnetic, electric, *etc.* common solutions prove efficient for high stroke/hig force solutions, yet are generally large and heavy, and for certain applications may be prohibitive, or can be even unusuable due to environment restriction (temperature, pressure, radiations, *etc.*). Knitted nitinol textiles can be electrically driven, heated by Joule effect. These textiles provide high stroke/high forces (stroke up to 100% and forces between tens to hundreds Newtons) with limited size and energy consumption. Their activation temperature can also be tuned to fit external temperature restrictions thanks to the wire chemical composition and heat treatment. In addition, the damping capabilities of knitted nitinol textiles have been studied in vibration damping solutions [21]. A particularity of knitted textile is the high internal mobility, inducing prominent friction energy dissipation. Using nitinol wires not only allows for higher sliding strokes but also provides a second source of energy dissipation, namely the superelastic mechanical hysteresis. Coupling such two main nitinol properties allows for knitted textiles to be high damping materials compared to knitted or woven textiles made of stainless steel, carbon-fiber, glass fiber, *etc.*

Finally, knitted NiTi textiles have been thought about for spatial counter-pressure suit for astronaut [51]. This suit aims at providing pressure to the astronaut's body to counteract outer space vacuum that tends to inflate indefinitely the astronaut's body. Yet their use has been rejected due to difficulties to use recoverable strain to act as counter-pressure. This underlines the lack of knowledge around knitted nitinol textiles and the lack of tools to fully understand the deformation mechanisms and mechanical behavior of such textiles. Few analytical and numerical models for

knitted textiles are presented thereafter.

4 Experimental and numerical analysis of knitted textiles

Analysis tools have been proposed to study knitted textiles. They can be divided into experimental, numerical, and analytical analysis. Experimental tools allow to perform mechanical tests on textile samples. Numerical and analytical tools provide a way to analyze the mechanical behavior of a knitted textile depending on the loop and sample geometries and wire properties.

4.1 Experimental analysis

Experimental tools dedicated to knitted textiles allow to apply various loading situations to specimens, such as uniaxial tension and biaxial tension.

4.1.1 Uniaxial tension

During uniaxial tensile test, a sample is stretched along a principal direction. This test is particularly useful to characterize isotropic material; those materials require to characterize mechanical properties in only one direction of space to entirely characterize the material.

A stretch λ_{max} is imposed along a direction of the specimen (Figure II.11). The reaction force is recorded and allows the stress state inside the sample working area to be computed. The stress state is usually assumed to be uniform. The relation between stress and strain is analyzed to provide parameters depending on the chosen behavior model (elastic-plastic, viscoelastic, superelastic, *etc.*). Finally, by measuring the section variations normal to the tensile direction, the material Poisson's coefficient can be computed.

In the working area, the following Cauchy stress tensor is expected for any point M in the working area:

$$\underline{\underline{\sigma}}(M) = \begin{bmatrix} \sigma_{xx} & 0 & 0 \\ 0 & 0 & 0 \\ 0 & 0 & 0 \end{bmatrix}_{(x;\vec{y},\vec{z})} \tag{II.1}$$

This particular tensor is obtained due to St Venant principle, and free edges in y and z directions.

To obtain such stress tensor, the sample is clamped in a jaw at each end to stretch the sample in the desired direction. This griping method yet constrains all three displacements at once in the grips. To reduce the impact of grips and boundary effects on the stress field distribution, the working area is generally slender as opposed to the clamping area, drawing a "dog-bone" shape (Figure II.11). Yet this specimen shape is not obtainable for materials such as knitted textiles due to unraveling. Furthermore, to have a representative mechanical behavior in the working area of an architectured materials, the ratio between sample section width and RVE size is a crucial parameter. For porous metallic foams, a minimal ratio of seven have been defined before the ultimate stress is significantly modified [52]. In that case, the sample needs either to have a very long x dimension to keep the aforementioned hypothesis [53], or gripped by a system providing free y displacement, assuming a plane stress case (z direction neglected) [50].

To allow such free transverse displacement, a system of metallic rings piercing through the knit loops holes and thread around a stiff rod has been proposed [50] (Figure II.12a). One rod is

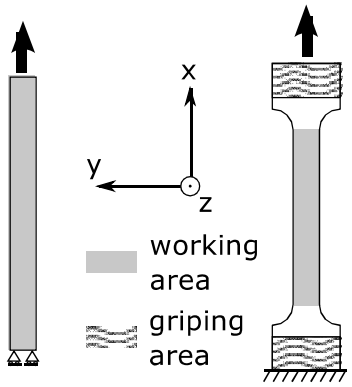

Figure II.11. Theoretical uniaxial tension test (left) and dog-bone specimen (right).

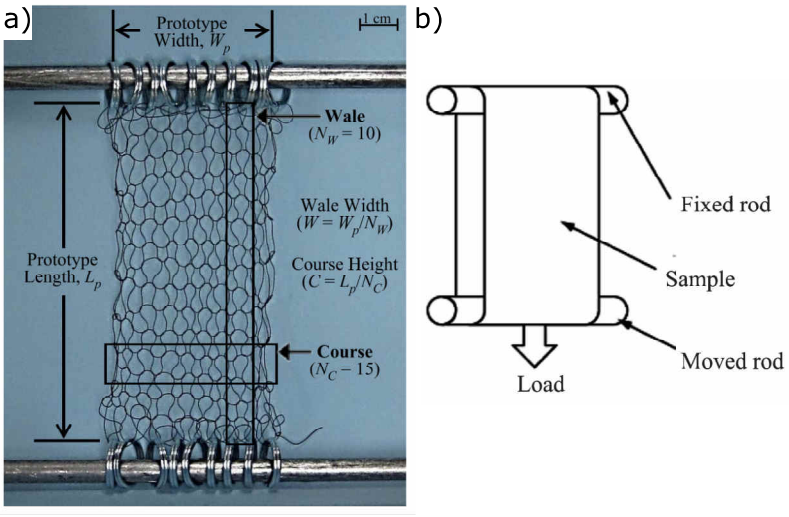

Figure II.12. Knit uniaxial tension test devices, reproduced from a) Abel *et al.* (2012) and b) Komatsu *et al.* (2008).

fixed while the second is moved out to stretch the specimen. The rings used to attach the specimen to the rods can slide, allowing the specimen to contract when stretched. However, this system is highly sensitive to friction between rings and rods. The width reduction is therefore not totally free and affects the measured mechanical behavior.

Another system of uniaxial tension for knitted textiles uses tubular knit structure [54]. Two rigid rods are inserted in the inner hollow of the knitted tube, and fixed in grips (Figure II.12b). The specimen is then stretched and the tube is then equivalent to testing two flat specimens at once. This prevents most stress field non-uniformities induced by the griping method. Yet transverse displacements of the textile remain constrained by friction between textile and rods. Furthermore, only wale direction may be tested as tubular knits can not be manufactured with the wale direction aligned with circumferential direction.

For both methods, the textile unraveling imposes to have a closing straight wire on the sample edges running along the wale direction. This wire is stretched during tensile test on the knitted structure and stiffens the specimen. This wire can be however removed yet the integrity of the structure becomes compromised, as seen in Figure II.12a.

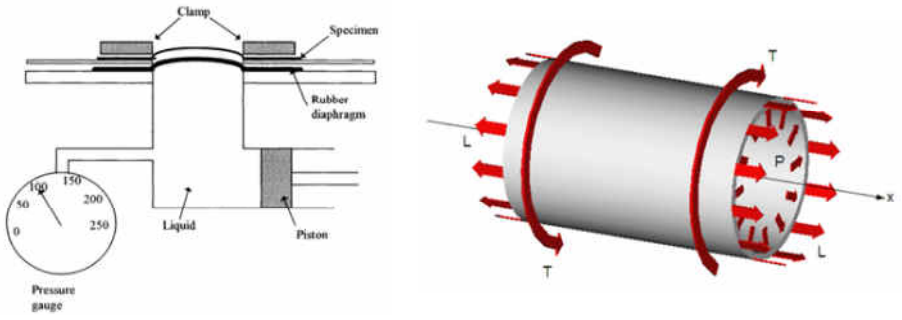

Figure II.13. Bulge tests methods on disk specimen (left) and tubular specimen (right).

4.1.2 Biaxial tension

As knitted textiles show high degree of anisotropy and a strong dependence of mechanical behavior on loading path, the simple tensile test is not enough to totally characterize their mechanical behavior. Biaxial tensile tests are thus preferable to characterize such materials as they allow for more complex and closer to reality loading cases. Several methods to apply biaxial loading to specimens have been proposed during past decades.

Two main categories of biaxial tension exist: i) out-of-plane biaxial tests, and ii) in-plane biaxial tests.

4.1.2.i) *Out-of-plane biaxial tests (bulge test)* This test is realized by holding a sample between grips and inflating the sample with a fluid under pressure. This technique can be applied to tubes [55, 56] or membrane specimens [57–59]. For both specimen shapes, the strain field on the outer surface is computed thanks to Digital Image Correlation (DIC). The sample respects the membrane hypothesis (negligible bending in the sample thickness)

Flat specimen In this case, the specimen is held between two flanges (Figure II.13). An hydraulic or pneumatic pressure system is used to inflat the sample, and the pressure is recorded during the test. Two cameras record the full strain field on the outer surface of the sample. Using the membrane hypothesis (negligible bending in the sample thickness) and the hypothesis of axisymmetry (isotropic material and circular sample working area) the stress state inside the sample can be deduced from pressure and sample curvature.

To test knitted textiles in such a way, a waterproof addition has to be used due to the textile porosity. A soft silicone membrane is usually placed under the knitted textile [20] (Figure II.14). The silicone stiffness has to be small compared to the knitted textile to lower its impact on the overall mechanical behavior.

However, the use of such a membrane generates “bubbles” of silicone through the textile and strongly impacts the system mechanical behavior. Such a test presents drawbacks such as non-uniform stress distribution induced by clamping method, and the impossibility to control the loading path which depends on sample geometry and mechanical properties [60]. Eventually, due to the textile anisotropy, stress state cannot be computed within the sample.

Cylinder specimen For that type of bulge tests, the tubular specimen is held at each tube ends by dedicated hollow grips (Figure II.13). The sample axial stretch and torsion are

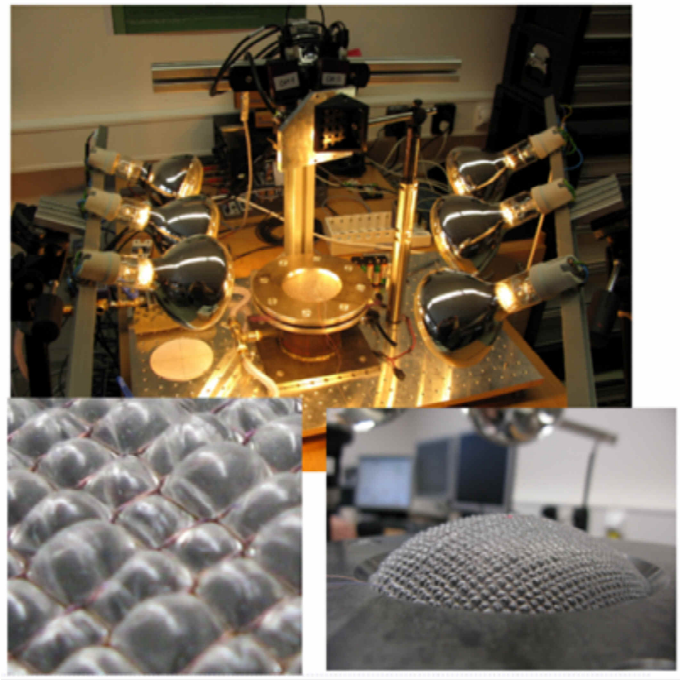

Figure II.14. Bulge test on knitted textile with impermeabilizer, reproduced from Heller *et al.* (2012).

usually controlled. The applied load-case history can therefore be highly complex. Similarly to the aforementioned disk bulge test, a soft membrane has to be used to overcome the textile porosity. In this test, the axisymmetry hypothesis is also necessary to compute the stress state inside the sample. A set of two cameras allows the strain field to be computed on approximately one third of the tube.

However, as for the first bulge test method presented, "bubbles" appear and impact the mechanical behavior of the textile. Furthermore, stress gradients are observed across the tube wall unlike in planar biaxial tests preventing computing the exact stress state within the sample [60].

4.1.2.ii) *In-plane biaxial tests* Regarding the in-plane biaxial tensile test, different experimental setups have been proposed throughout the years. Several griping methods and corresponding specimen shapes have thus been developed (Figure II.15, grips represented hatched).

A first common experimental setup uses cruciform specimens griped at the end of each arm (Figure II.15a). This method is mostly used for massive or metallic plates and is an extension of dog-bone shaped specimens used in uniaxial tensile tests [60–66]. Specific specimen shapes have been designed to improve strain uniformity on the specimen zone of interest [62, 67–73].

Some specific materials, such as knitted textiles or living tissues, yet prevent the use of cruciform shaped specimen due to the nature of their inner structure. In those cases, square samples are mandatory, and the mounting setup must be adapted. For such specimens, three main types of setups are used [74] (Figure II.15b-d). The first one uses a single grip along each edge of the square (Figure II.15b) [5, 75]. For this griping method, displacements transverse to tensile directions are prevented in the grips, constraining the sample expansion in those directions.

For soft membranes, a modification of the previous method has been proposed, removing the constraint on transverse displacements. This method uses multiple attachment points along each edge instead of a single rigid grip (Figure II.15c-d) [6, 54, 74, 76–81]. The attachment points can

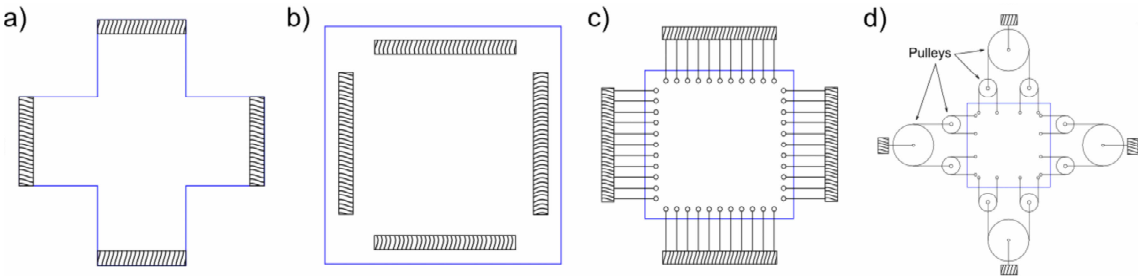

Figure II.15. Plane biaxial test - common specimen shapes and grips: a) cruciform [4], b) square with solid grips [5], c) square with point grips [6], and d) square with point grips and pulleys [7,8]; hatching represents grips.

either be directly the fixation points of small grips [71, 82] or the extremities of linkages between the specimen and grips [6, 76, 80, 81, 83]. For example, the commercial device BioTester 5000 test system (CellScale Biomaterials Testing, Waterloo, Ontario, Canada) uses a set of rigid bars piercing through the sample; those links allow free rotation of each attachment point in the sample. As a limitation, forces distributions along the specimen edges are unknown.

Further improvements of previous setup led to the use of pulleys sets to link pairs of attachment wires in order to balance boundary forces on each edge (Figure II.15d) [7, 8, 84]. Low friction in pulleys rotation axes implies identical forces at each attachment point. This method yet limits the number of attachment points.

4.2 Numerical and analytical analysis

The experimental analysis tools described earlier allow existing textiles to be characterized macroscopically, yet do not provide local stress state in the wire section. To perform local wire studies, two methods are available: i) analytical analysis, and ii) numerical analysis.

4.2.1 Analytical analysis

Analytical analysis applied on a single loop proposes to solve static or dynamic equilibrium equations in regard to the loop geometry and boundary conditions. Due to the small wire diameter compared to curve length, the approximation of beam theory is commonly used to simplify models.

The loop geometry can be described by a set of parametric equations proposed by Leaf & Glaskin (1955) [85]. Several analytical models are found in literature, and three of them have been selected to illustrate such diversity.

The first analytical model presented has been proposed by Wada *et al.* (1997) [86] where a complete loop is studied. The loop geometry has been chosen so as the contact points in the wale direction are in the RVE (Representative Volume Element) (Figure II.16). Crossing points $A - B$ and $A' - B'$ are used to define the contact line of action L_a and L'_a. Then, contact points $C - D$ and $C' - D'$ are defined on each segment $A - B$ and $A' - B'$. These points are initially placed halfway to crossing points. Points C and D are linked by two springs. One is orthogonal to the line of action (AB) to define the radial stiffness of the contact. The second spring is defined collinear to (AB) to represent the sliding friction. Forces are then simply applied on the loop ends to stretch in the knit principal axes. This model has been shown to represent accurately the

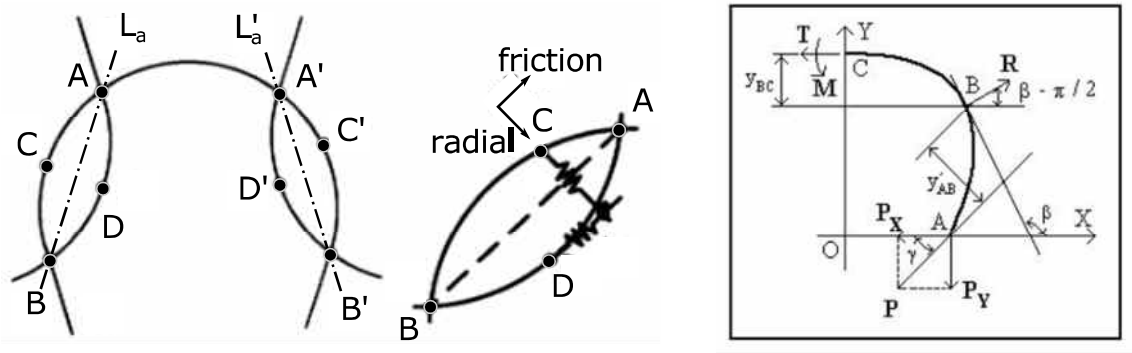

Figure II.16. Analytical models for plain weft knitted textiles from Wada *et al.* (1997) (left) and Araujo *et al.* (2003) (right).

mechanical behavior of a knitted textile over small deformations, when the geometry of loops does not change much. However, this model is limited in terms of maximum deformation and loading path, restricted to the textile principal axes.

Araujo *et al.* (2003) [87] considered half a loop and assumed symmetrical boundary conditions along the vertical axis. Then, considering the central symmetry of the loop geometry, the hypothesis that each yarn presents identical stress state as the other is proposed. The problem is reduced to one half yarn from the whole loop (Figure II.16). A few hypotheses regarding the yarn behavior are also necessary (incompressible yarns, no friction between fibers, inextensible yarns, *etc.*). This model has been shown to fit accurately the mechanical response of a knitted textile stretched in the wale direction, but under-estimates the response in the course direction. This model has also the advantage to fit for maximum strains up to 27% in the wale direction and 65% in the course direction. However, like the previous model, only loadings in the principal directions are allowed.

Lastly, Abel *et al.* (2012) [50] extended the model proposed by Araujo *et al.* (2003) [87] to knitted textiles made of NiTi wires. NiTi material allows the hypothesis regarding yarns incompressibility in the general model to be removed: the superelastic mechanical behavior of the material is approximated by a succession of three linear elastic behavior, considering a full austenitic or martensitic material when appropriate (no mixed state is allowed). This model has been extended to take into account the possible activation of the NiTi due to the shape memory effect and the thermomechanical cycle. Therefore, this model is able to take into account the textile loading history. This model has proven to precisely reproduce the mechanical behavior of a knitted NiTi textile in fully austenitic and in fully martensitic state during a wale-wise uniaxial tensile loading after calibration of the friction coefficient of NiTi wires. However, this model has not been tested on course-wise loading.

Those models have been shown to simulate accurately the behavior of a knitted textile in specific loading cases. However, limitations exist regarding the loop geometry, the loading path, *etc.*: the loop geometry from Leaf & Glaskin (1955) is restrictive since this geometry is centered symmetric, while textile loops can have arbitrary geometries. These analytical models also do not aim at analyzing the local behavior of the wire during tests.

Therefore, other analysis tools should be used to study biaxial loading cases and local wire behavior. This will help to understand the mechanical behavior of knitted textiles.

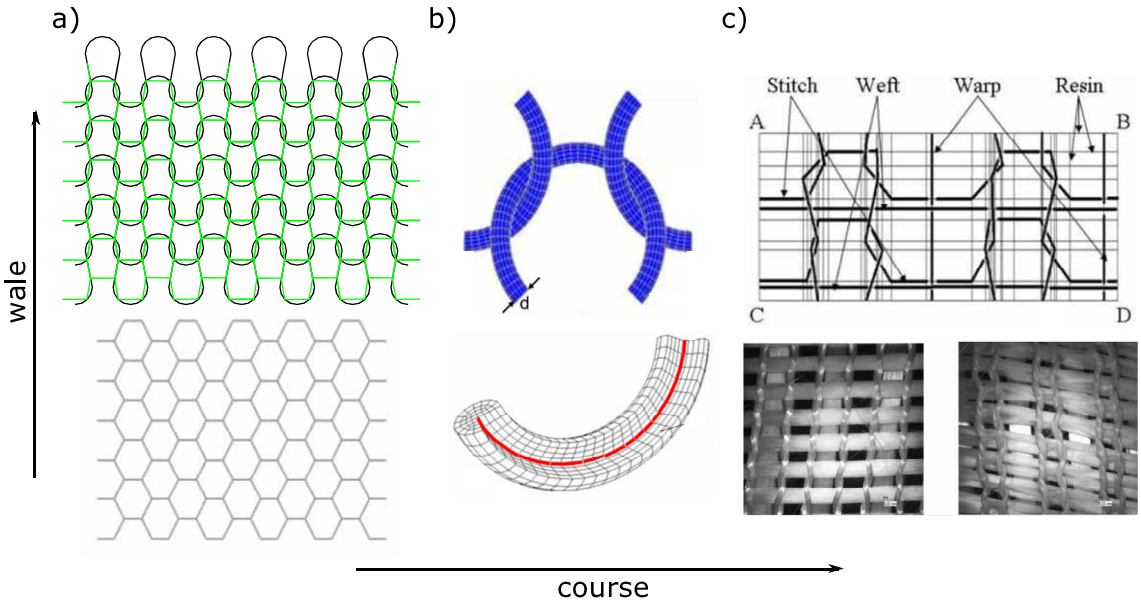

Figure II.17. Numerical models from a) Araujo *et al.* (2004), b) Bekisli *et al.* (2009), and c) Demircan *et al.* (2011).

4.2.2 Numerical analysis

Numerical analysis tools using finite elements allow to study any chosen loop shapes and complex loading cases. They propose to study a large sample by simplifying the textile architecture or to study a single loop using homogenization method. The single loop models also enable to study friction influence between wires and provide insight in the local stress state of the wire. However, calculation times can drastically lower the applicability of such tools. Three different finite element models are described hereafter.

Araujo *et al.* (2004) [88] proposed to simplify the knitted textile looping geometry by a regular hexagons mesh (Figure II.17a). Curved yarn segments are represented by straight truss elements. Two truss properties are defined, one used for elements aligned in the course direction, and one used for elements in the wale direction. In that way, a large sample can be modeled. This model has been shown to reproduce accurately the mechanical behavior of a plain weft knitted textile in both wale-wise and course-wise uniaxial tensile tests, up to 25% deformation. The formability over a rigid sphere has also been presented to highlight the high formability of such textiles. As opposed to its analytical counterpart, this model is reliable in both wale-wise and course-wise directions. Furthermore, as the whole sample is modeled, boundary conditions impact is less critical and strain fields non-uniformities are simulated. The use of the simplified structure allows calculation costs to be reduced drastically. However, this model does not allow to study the local behavior of the wire, weak spots around contact, and friction gliding phenomena during tests.

In Bekisli *et al.* (2009) [18], a finite element model dedicated to study plain weft knitted textiles made of glass fibers yarns composites is proposed (Figure II.17b). The studied loop geometry is taken from Leaf & Glaskin (1959) presented earlier yet is not restricted to such geometry. The yarn neutral fiber is modeled using 3D beam elements which drives the yarn mechanical behavior. The volume occupied by the yarn is modeled using 3D elements and represents the yarn volume change during loading. Finally, the contact is managed by surface elements on the outer surface of the yarn volume elements. This complex model is made over a few loops in the course direction

and periodic boundary conditions are applied in the wale direction. This model has been shown to be able to predict the stretch at which locking occurs for several knit samples. At this point, loops do not glide anymore, and yarn segments between contact zones extend in their axial direction. However, this model remains specific to uniaxial loading case in wale-wise direction.

Demircan *et al.* (2011) [89] studied the mechanical behavior of a composite made of a vinyl ester resin and a knitted glass fibers textile reinforcement. The interest has been drawn towards the different Young's moduli of the composite depending on the loading direction (course and wale). Beam elements have been used to model the reinforcement, and the remaining volume of the RVE was filled with 3D elements for the matrix (Figure II.17c). This simplified model allowed an estimation error of less than 3.1% of the Young's moduli of two composites made of knitted textile reinforcement. The failure stress of the studied specimen has also been properly predicted. However, this model was tested only in uniaxial wale-wise tension.

5 Conclusion

A large number of analysis tools has already been proposed in literature to study knitted textiles mechanical behavior in an experimental or analytical/numerical way. However, few of them are able to study the wire internal and contact stresses during textile loading. Furthermore, only one analytical model can account for thermomechanical behavior of nitinol wires.

In order to better understand the mechanical behavior of knitted textiles, a versatile numerical tool is developed in this work and is inspired by these models. Relevant experimental results will also be provided to validate such numerical model. The required numerical model should be able to predict the behavior of the knitted NiTi textile while keeping computational times as low as possible. Different model hypotheses will be analyzed and confronted with experimental data one by one.

CHAPTER

III Experimental analysis tools

1 Introduction

To experimentally study knitted NiTi textiles, a complete method has been proposed in this work. This method consists of a knitted textiles dedicated image analysis software, a biaxial tension setup, and a method to characterize the friction coefficient between two NiTi wires.

2 Kinematic fields measurement

To perform experimental kinematic fields measurement, two options are available: Digital Image Correlation (DIC), and an in-house developed software. In this section, the DIC principle is first briefly described and application examples on knitted textiles pictures are presented (Section 2.1). Due to limitation of DIC compared to the required data to extract, a software has been developed in-house specifically for knitted textiles studies (Section 2.2). Lastly, an illustration example of kinematic fields is given on an experimentally obtained picture (Section 2.3).

2.1 2D Digital Image Correlation

Digital Image Correlation (DIC) is an optical method that employs tracking and image registration techniques for accurate 2D and 3D measurements of changes in images. This technic is often used to measure 2D/3D displacements and is widely applied in many areas of science and engineering [1]. Thereafter is presented two-dimensional DIC method used in the study of planar samples for analysis of displacement and associated strain fields.

A few definitions are required for the following sections (Figure III.1):

Subset: square part of the initial image centered on point M_i to be tracked, size $n \times n$ pixels;

Area of Interest (AOI): zone of the image where tracking points M are of interest;

Step: distance in pixel between centers M_i of two neighbors subsets;

Speckle: random marks realized on the sample surface used to track the subset;

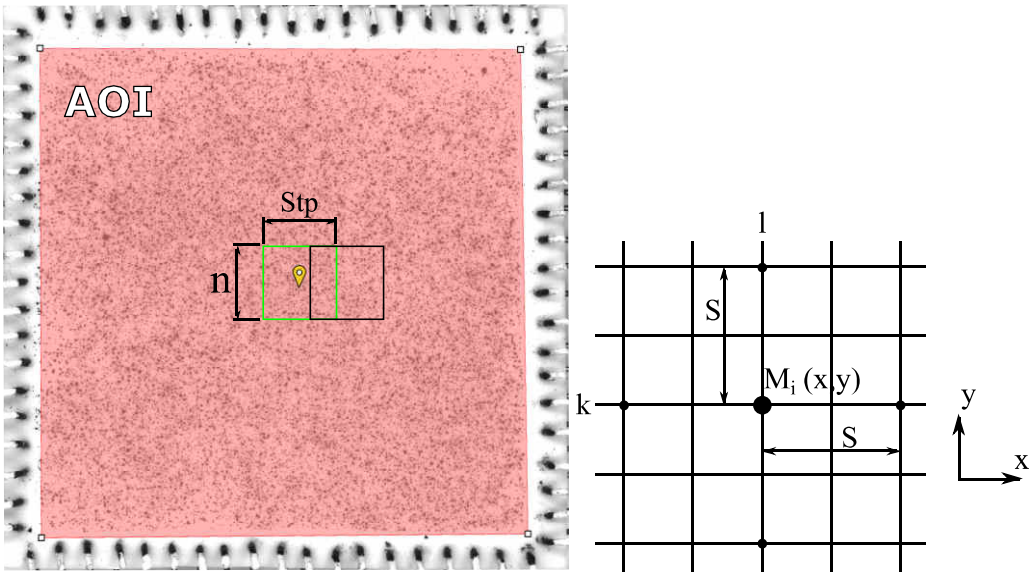

Figure III.1. Representation of AOI, Subset, and subset Step used in DIC analysis (left) and representation of subsets center M_i grid

The speckle pattern is usually realized with spray paint of contrasting color. In order to track each point M_i, the subset speckle is required to be specific (the speckle needs thus to be as random as possible and contains at least 7 to 9 specks). Each subset will then be tracked in each successive image. The area of interest is decomposed in a regular grid of subsets, whose centers M_i are separated by a distance equal to the chosen step. The size of the subset is usually chosen such as the ratio between step and subset size is equal to 1/3.

Subset and step sizes are important parameters: a small subset size implies a better resolution as more points M_i displacements will be obtained over the AOI. However, the subset needs to be large enough so that the subset speckle is unique. The step size ratio with subset size refers to the overlap of subset and the redundancy of data. A small ratio will prevent loss of data as the same speck will be contained in many subset. However, the smaller the step size, the longer the calculation and the smothered the data.

The DIC operational principle can be decomposed in 3 main successive steps:

- Placement of initial subsets in the initial image (img 0)
- Detection of the new position of each subset in next images
- Calculation of various quantities from subsets center M_i position

To perform the image correlation analysis, the pattern of a group of pixels in subset S_i is correlated to the new position of the subset in the following image (Figure III.2). Positions around the initial coordinates are tested by matching the pixels gray scale value. A correlation factor is calculated at different possible positions $M_i'(x+u, y+v)$ as:

$$C(x,y,u,v) = \sum_{i,j=-(n-1)/2}^{(n-1)/2} [I_0(x+i, y+j) - I_p(x+u+i, y+v+j)]^2 \qquad \text{(III.1)}$$

[1] One very common application is for measuring the motion of an optical mouse.

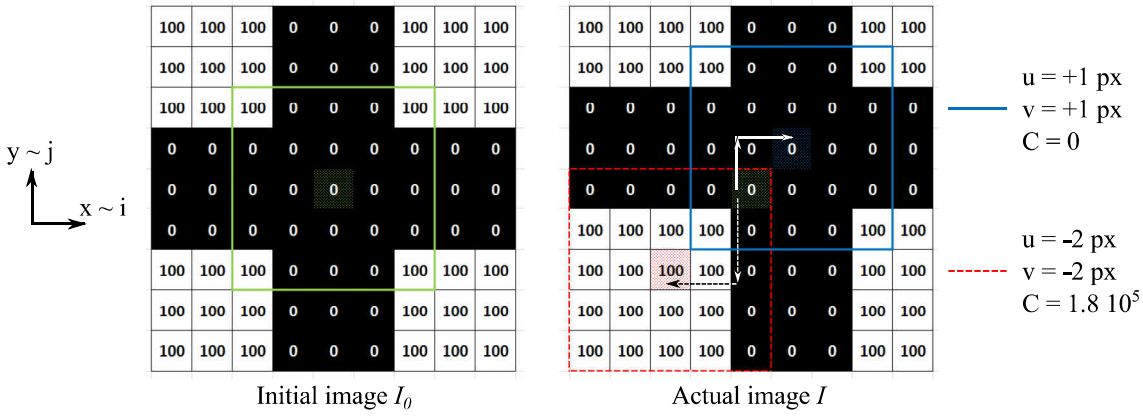

Figure III.2. Schematic representation of initial image with initial subset (left) and successive image with tested subset movement (right)

where I_0 and I_p are the reference and current images respectively; (x,y) are the subset center M_i coordinates in initial image I_0 and (u,v) are its displacements in the actual image I_p; *n* is the subset width; and (i,j) are indexes that cover pixels in the subset

The correlation factor C is computed for neighbor possible couple (u, v) in the image I. The sought displacement corresponds to the lowest value of C (Eq. III.1).

To search for the subset S in successive images, two options are available: initial correlation or incremental correlation. For initial correlation, the deformed subset S_p in image I_p is correlated in reference to the initial subset S_0 in image I_0. During incremental correlation, the deformed subset S_p in image I_p is correlated in reference to the subset S_{p-1} in image I_{p-1}. This method provides with correlation where subsets are largely deformed. However, computation precision decreases as errors in successive image stack on each other. Furthermore, the loss of a subset in image I_p induces the loss of the subset in next images.

After the image analysis is complete, grid displacements are obtained from the subsets center M_i position. Several quantities can be computed, such as interpolated displacement field in the camera axis. For the strain fields computation, the distance variation between subsets center M_i is used: let a regular grid be indexed with *k* for row index and *l* for column index (Figure III.1, right). Each point M_i of such grid is indexed $M_i(k, l)$ and possesses a set of initial coordinates (x, y) and deformed coordinates $(x + u, y + v)$. A step *S* is defined as the difference in index *k* or *l* around the point of interest. The gradient at a point $M_i(k, l)$ is defined as:

$$\begin{aligned} \Delta_x(M_i(k,l)) &= u(M_i(k,l+S)) - u(M_i(k,l-S)) \\ \Delta_y(M_i(k,l)) &= v(M_i(k+S,l)) - v(M_i(k-S,l)) \end{aligned} \tag{III.2}$$

Then, the calculation of strain components can be performed using the distance variation (Eq.III.2) and the desired formulation of strain (engineering, Hencky, Lagrange, *etc.*).

To perform DIC analysis on knitted textile pictures, the wire structure itself constitutes the pattern used as speckle. The subset is defined to include almost 2 knit loops (Figure III.3). This method coupled with incremental correlation when high loops deformation occurs allowed displacements and associated strain fields to be computed for the textile at the scale of few loops. Such data does not provide with explicit data about the wire slipping, curvature changes, *etc*.

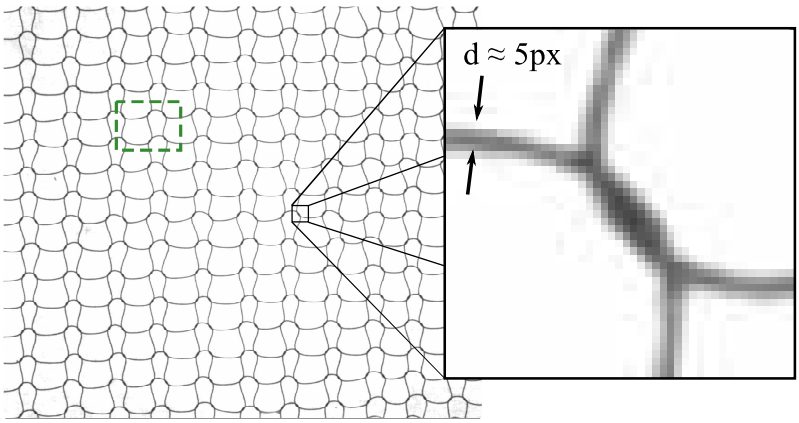

Figure III.3. Picture of a tested knitted textile with zoom on wire and a typical subset for knitted textiles (green dash)

2.2 In-house software for knitted textiles image tracking

2.2.1 Displacement field

A software dedicated to the knitted textiles study has been coded in-house. The software aims at providing displacement fields measurement for the textile and local wire curvature and slipping during loading. The basic functioning is as follows:

1) Detection and numbering of knit loops,

2) Building map of the textile loops structure,

3) Tracking versus time of loops centers,

4) Computation of loops singular points,

5) Estimation of each wire 2D shape,

6) Post-processing of data (displacement, strain, shape, *etc*.).

Initially, captured images are treated to reinforce contrast in order to strongly dissociate wire from background. Contrast function used for such leveling is user-defined.

The knit loops detection is first performed (Figure III.4). A function [2] detects closed area of same pixels value and labels those areas with a random number. Knit loops are therefore distinguished and referenced uniquely.

On the reference image, the position of loops centroid is computed. From the position of such center points, the neighboring loops are detected and organized in line in the wale direction (Figure III.5a). Possible rhomboidal textile structures are then automatically built and user selected (Figure III.5b).

The centroids position in image I_p is transferred in image I_{p+1} (Figure III.6). The new position of loops centroid is updated and the tracking of each loop centroid can be performed. This method yet implies that the maximum displacement increment between two successive images is small compared to the loop size.

[2] *bwlabel* function in Matlab

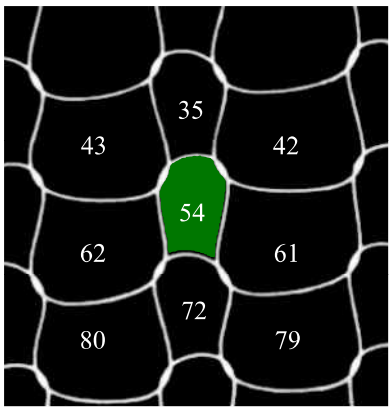

	43	35	42
	62	54	61
	80	72	79

Figure III.4. A knit loop "hole" (left) and tabular organization of loop labels (right)

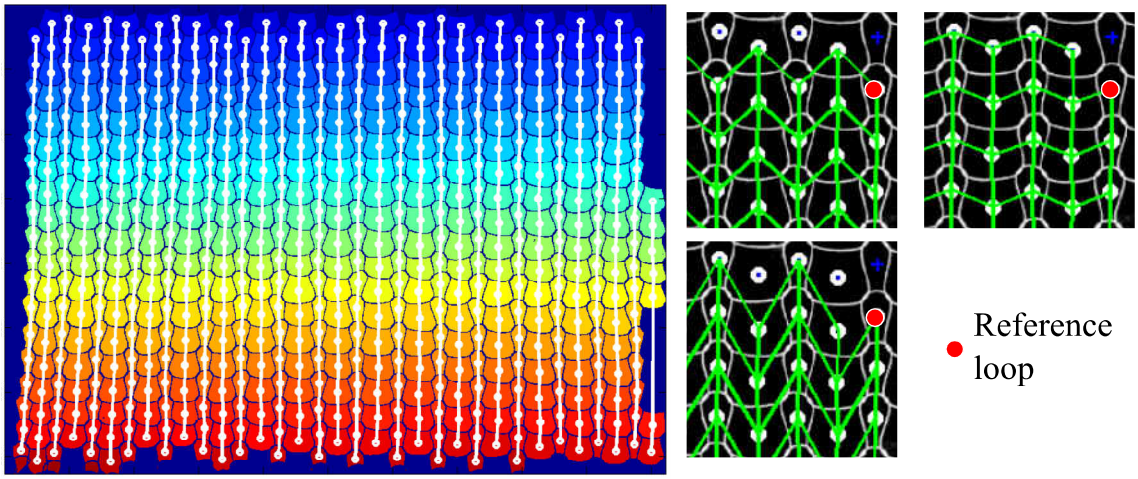

Figure III.5. Centroid placed in line (left) and three possible centroid architecture (right)

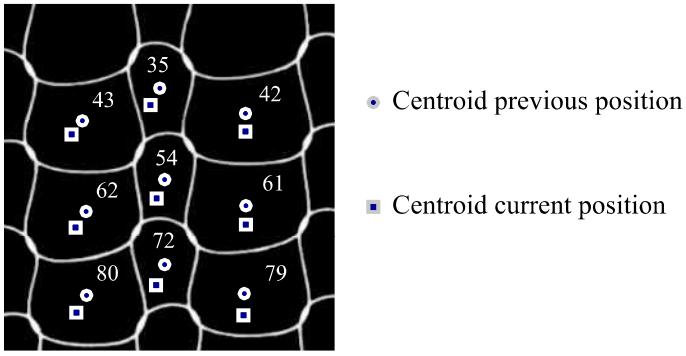

Figure III.6. Previous and current position of loops centroid superimposed on previous image

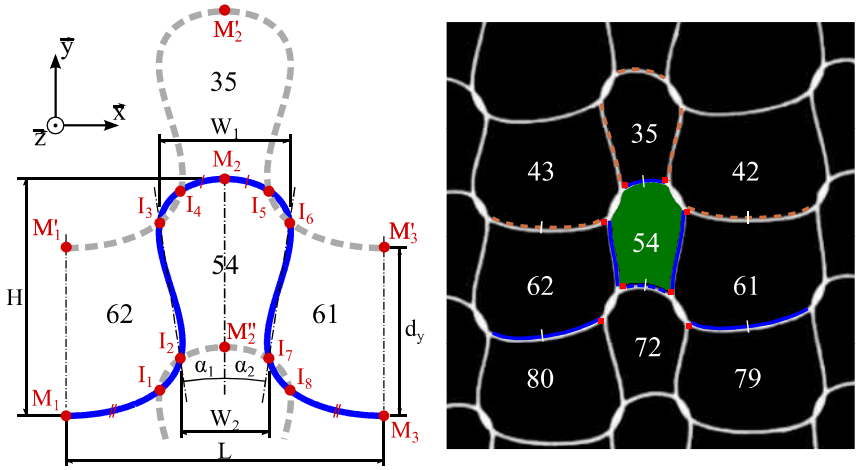

Figure III.7. Knit loop singular points and associated loop dimensions (left), and the corresponding segments and singular points in actual textile image (right)

2.2.2 Wire detection and loop geometry

The tracking of loops centroid allows displacement fields to be computed inside the textile. Yet, this information is limited, and images contain more information that can be deduced by tracking wire organization and shape. Wire sliding, curvature, and loop dimensions can be computed thanks to such tracking. The loop dimensions are described by 7 parameters, namely L, H, d_y, W_1, W_2, α_1, and α_2 (Figure III.7, left).

The loops are composed of wire segments and contact zone between two wale rows. The wire segments are named as follows:

- S_1 between I_2 and I_7,
- S_2 between I_6 and I_7,
- S_3 between I_4 and I_5,
- S_4 between I_2 and I_3.

Hence, the first step is to compute the loop wire structure and segments. Intersection points I_1 to I_8 are approximated as the closest pixel (red squares) of the loops area (green area) between neighbor loops, using the rhomboidal structure defined (Figure III.7, right).

Then, to identify wire segments S_1 to S_4, the color difference between background and wire is used. For each segment, a straight line is created between the two intersection points I delimiting the segment (Figure III.8). Two points are then created on this line, one in the middle and a second one shifted two pixels aside on the line. These points serve as an initial guess of the first points on the wire neutral axis.

The wire local center of mass is then computed into a circle centered on the initial guess (Figure III.8). The same process is applied on the second starting point to provide a second point on the wire neutral axis. Then, points are firstly guessed by extrapolating the position from the two previous points found. The same method is applied afterward to find points that define the neutral axis.

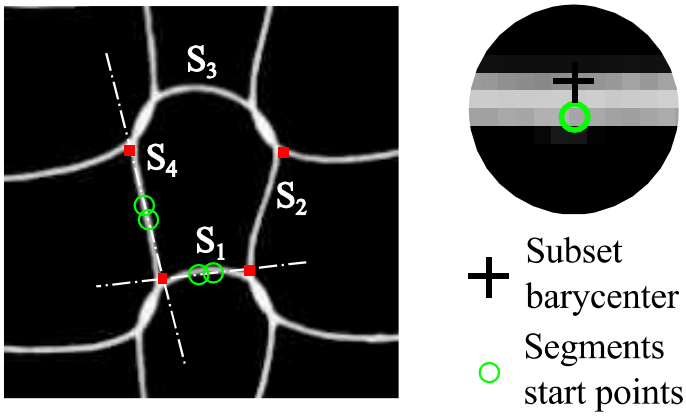

Figure III.8. Starting point for wire neutral axis detection and wire segments numbering (left) and circular mask and barycenter of subset for neutral axis detection (right)

This method is applied along the segment until the point I_s is found in the circle. When an extremity has been found, the wire is scanned in the opposite direction, starting from the two first points detected, up to the second intersection point.

2.2.3 Post-processing

Morphological parameters variations are computed after tracking each loop shape versus time. Dimensional parameters (L, H, and d_y) and morphological parameters (W_1, W_2, α_1, and α_2) are computed.

2.2.3.i) *Dimensional parameters* To perform the loop dimensional parameters, mid points in the sense of the curvilinear abscissa are defined, named M_1, M_2, and M_3. The knit loop length L is defined as the distance between points M_1 and M_3, belonging to adjacent loops. The knit loop height is defined as the distance between the straight line (M_1, M_3) and the point M_2. Lastly, the distance between two knit rows d_y is computed as the distance between M_2'' and M_2.

2.2.3.ii) *Morphological parameters* The loop widths are calculated as the distances between the intersection points: the loop larger width W_1 is the distance between I_3 and I_6; and the smaller width is the distance between I_2 and I_7.

To measure the characteristic angles of the loop i, the loop theoretical symmetry axis is defined as the line (M_2'', M_2). Then, angles α_1 and α_2 are defined as $(\vec{I_2I_3}, \vec{M_2''M_2})$ and $(\vec{I_7I_6}, \vec{M_2''M_2})$ respectively.

2.2.3.iii) *Mechanical analysis* The textile displacement fields $\underline{\underline{U}}$ and corresponding global strain fields $\underline{\underline{\epsilon}}$ are computed using loops centroid positions. The sliding between loops is computed using the variation of curvilinear length of segment 1 (course oriented) versus segment 2 and 3 (wale oriented).

2.3 Illustration example

Displacement fields $\underline{\underline{U}}$ have been calculated on experimentally obtained pictures of a knitted NiTi textile subjected to wale-wise uniaxial tension ($\vec{y}$) to serve as an illustration example.

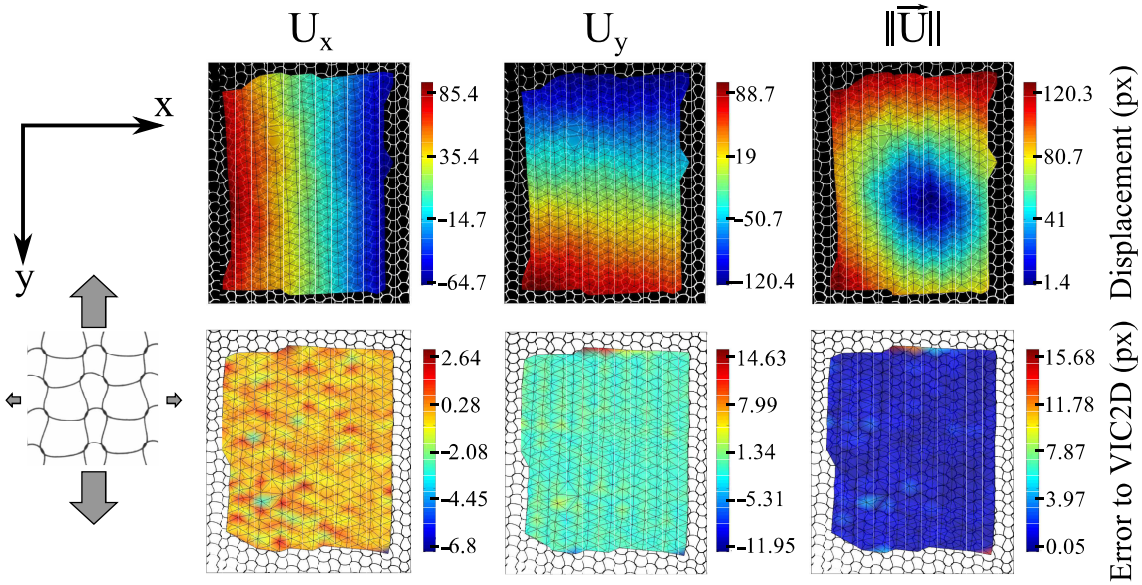

Figure III.9. Displacement fields, in pixels, obtained by the in-house software (top) and differences with VIC2D measurements, in pixels, (bottom) during uniaxial tensile loading in walewise direction (y)

The software developed in-house and presented in Section 2.2 computes displacement fields alongside several other data. Displacement fields obtained with such software are compared with results obtained using image correlation software VIC2D (Section 2.1) and presented in Figure III.9.

The first line of Figure III.9 presents displacement fields in pixel obtained with the software along x and y directions, and displacement vectors norm. The second line presents the difference between fields obtained by the software and by VIC2D. Error fields are scarce and random, showing only critical points in the sample zone of interest borders, where measurements tend to lack precision for both methods. However, the random repartition of error values indicates that no error are induced by loops movement and that those errors, being of the order of 2 pixels, are solely due to post-processing errors, either imputed to VIC2D and to the in-house software. At the zone of interest edges, high errors are found on few points, which are due to DIC measurement errors and therefore neglected. Errors are found less or equal to 5%, which is considered satisfactory.

3 Method to determine wire friction coefficient

During textile stretching, knit loops segments slide along each other. Friction thus has a preponderant impact on the mechanical behavior and energy damping capability of the knitted textile.

The friction coefficient between nitinol wires has not been widely studied throughout litterature. Many studies focus on friction forces intensity, mainly for orthodontic applications. Few studies provide a friction coefficient, and found values are scarce, ranging from 0.04 [90] to 0.13 [50] for the static friction coefficient to 0.51 for the dynamic friction coefficient [91]. An experimental setup has thus been developed to estimate the friction coefficient between two wires. The proposed principle is drawn in figure III.10.

To measure the friction cone angle, the orientation of the reaction force $\vec{R}$ between two NiTi wires is measured. When the reaction force $\vec{R}$ lies within the cone, no gliding occurs. When wires

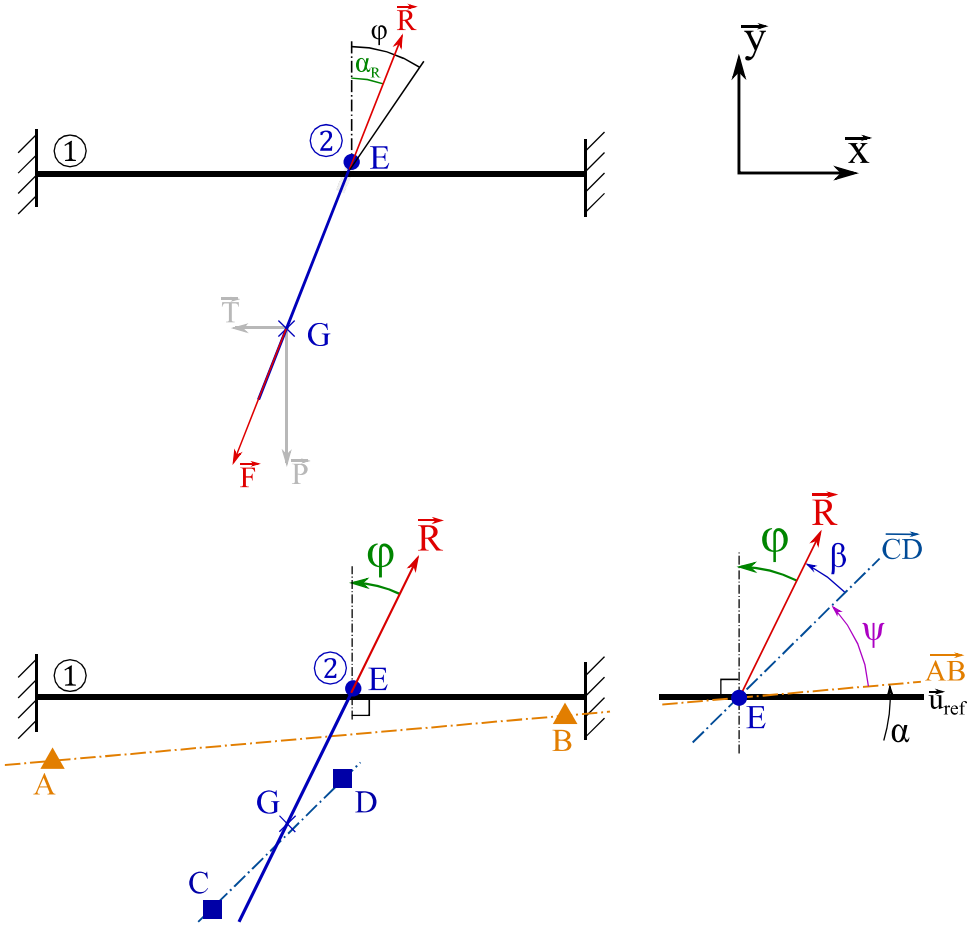

Figure III.10. Principle schematic of the wire friction coefficient measurement device developed. Top: the mobile in the random state within friction cone; Bottom: mobile axis along the friction cone depicted limit angle φ_l and angles notation used to compute friction cone angle φ.

start sliding, the reaction force is held on the friction cone surface. The friction cone angle can thus be deduced from the reaction force $\vec{R}$ orientation compared to the fixed wire when sliding occurs. The reference wire (1) is held horizontal and the second wire (2) is held perpendicularly. This wire is gripped into a mobile at point E. The mobile is articulated at its extremities (E and G) and submitted to two forces, namely wire reaction force $\vec{R}$ and mobile weight $\vec{P}$. Hence, the two forces are equal in norm and opposed directions, collinear to vector $\vec{EG}$. To vary the force $\vec{R}$ orientation in order to place it on the friction cone surface, an horizontal force $\vec{T}$ is applied to the mobile at point G. The reaction force $\vec{R}$ then becomes $\vec{R} = -(\vec{T} + \vec{P})$. The friction cone angle φ can then be computed. The associated friction coefficient f is equal to $f = \tan\varphi$.

To perform the reaction force $\vec{R}$ orientation measurement, two pairs of points have been introduced. Pair (A,B) defines the reference wire orientation. Pair (C,D) defines the mobile orientation. Those points are the centroid of targets that can be tracked in pictures during tests. The targets may not be exactly aligned with their respective reference. Therefore, error angles α and β have been introduced between wire 1 and line (AB) and between mobile axis $\vec{EG}$ and line (CD), respectively (Figure III.10, Bottom). The angle measured is the angle between (AB) and (CD), named ψ. The friction angle φ and the measured angle ψ are linked by the relation:

$$\alpha + \psi + \beta + \varphi = \frac{\pi}{2} \tag{III.3}$$

To remove from the calculation angles α and β, two sets of measures are realized, with opposite sign for the tension $\vec{T}$. In such case, two values of ψ are obtained, named ψ^+ and ψ^-, for $\vec{T} > \vec{0}$ and $\vec{T} < \vec{0}$ respectively. Hence, equation III.3 becomes:

$$\begin{aligned} \alpha + \psi^+ + \beta - \varphi &= \frac{\pi}{2} \\ \alpha + \psi^- + \beta + \varphi &= \frac{\pi}{2} \end{aligned} \tag{III.4}$$

Substracting both equations of Eq. III.4 results in the following relation between measured angles and friction cone angle:

$$2\varphi = \psi^+ - \psi^- \tag{III.5}$$

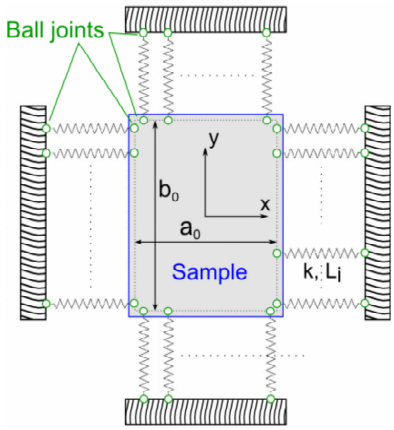

Figure III.11. Principle sketch of the setup in initial state.

4 Biaxial experimental setup

4.1 Introduction

Preliminary tensile tests have been performed on knitted textiles and deformations obtained range from 0% to 40%. The corresponding lineic force level has been measured to 0.2 $N.mm^{-1}$ approximately. During biaxial tests, strain fields heterogeneities in the specimen may be caused by boundary conditions distributions or the textile intrinsic architecture heterogeneities. Therefore, the experimental setup boundary conditions heterogeneities are studied on homogenous soft silicone membranes. The membranes have been chosen for the strain range required. The membranes thickness has been chosen to result in a corresponding lineic force level at maximum strain as knitted NiTi textiles provided.

A description of the principle of the new proposed experimental method is first presented (Section 4.2). An experimental setup based on this principle is then presented (Section 4.3.1 to 4.3.2.ii)). Specimen and fabrication process used to test the device are then introduced (Section 4.3.3). Finally, results are presented (Section 4.4) and analyzed (Section 4.5) before concluding (Section 4.6).

4.2 Principle of the experimental setup

The aim of the setup proposed in this work is to combine both methods *c* and *d* advantages (Figure II.15 c and d). To do so, attachment wires used in setups *c* and *d* have been replaced by elastic elements (Figure III.11). Pictures of springs and specimen zone of interest are acquired by cameras during tests. The displacement and strain fields inside the sample zone of interest are then obtained by DIC analysis. Elongations of the elastic elements are analyzed to provide boundary loads distributions.

4.3 Experimental setup method

The proposed experimental setup will be first further described in Section 4.3.1. The boundary loads calculation method is then presented in Section 4.3.2, followed by the definition of physical quantities used to characterize and to analyze samples mechanical behavior (Sec-

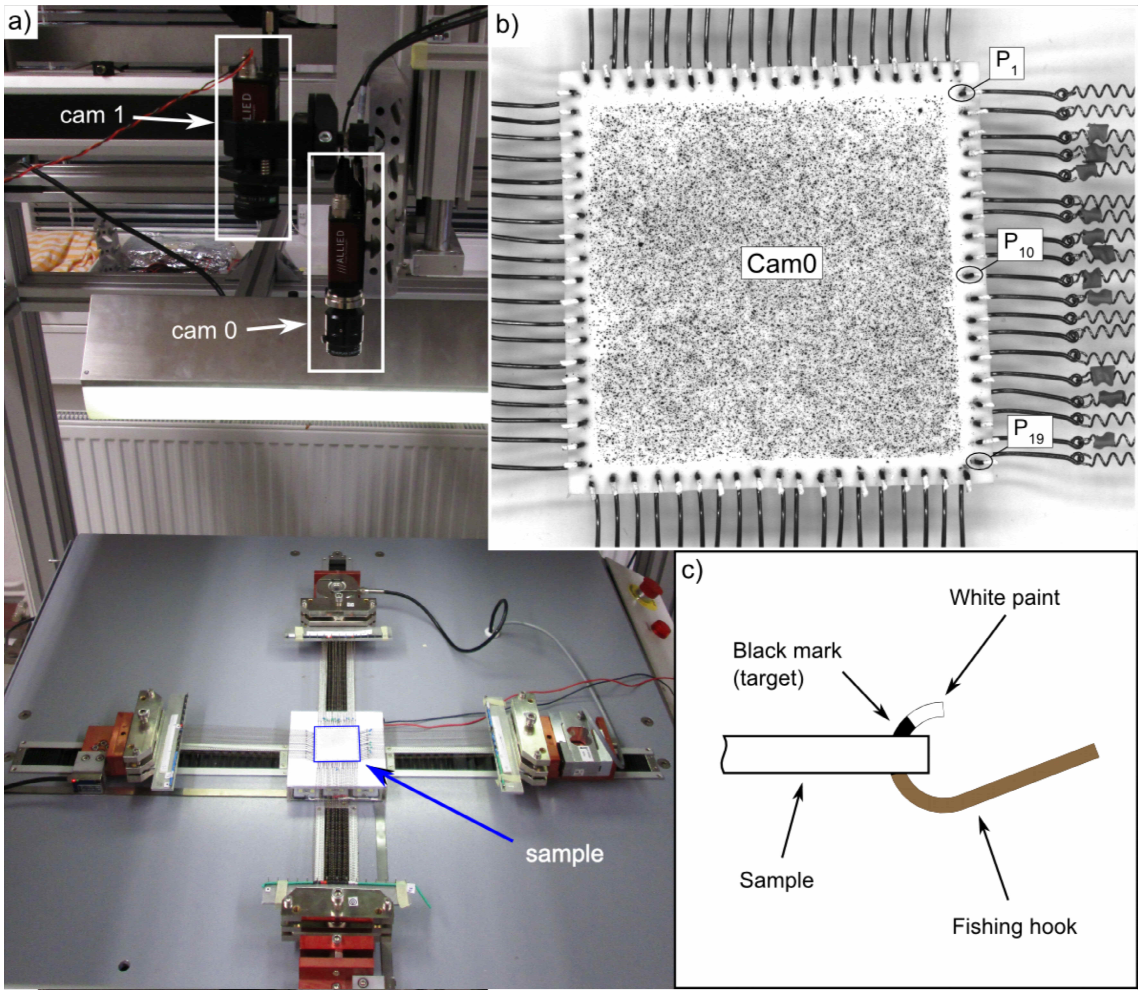

Figure III.12. Pictures of a) the biaxial tensile machine with experiment set up and the two cameras "Cam0" and "Cam1", b) "Cam0" picture, and c) linkage and associated target design.

tion 4.3.2.ii)). Lastly, the material preparation and the samples fabrication procedure are described (Section 4.3.3).

4.3.1 Method

The biaxial tensile machine (C&B Tessile, Cinisello Balsamo, Italy) used is composed of two pairs of grips, moving symmetrically compared to the machine origin (Figure III.12a). One grip per direction is equipped with a load-cell with maximum force of 500N and a resolution of 0.1N.

In this work, small diameter helicoidal steel springs were used to measure force distributions on the sample boundaries: one spring end is fixed into the grip while the other end is hooked onto the sample (Figure III.11). The sample zone of interest is delimited by the springs attachment points. Its dimensions have been noted $a_0 \times b_0$, and its thickness e_0. Each spring has an initial length L_i and a stiffness k (Table 4.3.1). Springs link between the sample edge and the grip are equivalent to ball joints: springs have been attached to the sample using fishing hooks. Targets have been painted on each hook tip so as to be used as specific tracked points (Figure III.12c). The helicoidal springs outside diameter is reduced to allow a maximum number of springs on the

Table III.1. Springs parameters

n	D (mm)	d (mm)	L_i (mm)	k ($N.mm^{-1}$)
19	1.6	0.28	153	0.21

sample edges without interference. Moreover, a higher number of attachment points is expected to provide a more uniform strain field inside the sample area of interest [83, 92].

To measure the required displacements, two cameras have been used (Stingray F-504B/C, Allied Vision Tech., Stadtroda, Germany) (Figure III.12a). Camera "Cam 0" is used to record images of the sample zone of interest (Figure III.12b). A Digital Image Correlation (DIC) analysis of the strain fields inside the sample is processed with these pictures (VIC 2D, Correlated Solution, US). Camera "Cam 1" provides images of the setup on which grips and springs hook targets displacements have been tracked. "Cam 0" and "Cam 1" have been synchronized by an acquisition software (Mercury RT, Sobriety s.r.o., Czech Republic).

4.3.2 Definition of measures

4.3.2.i) *Spring loads* Each spring i develops a force $\vec{F}_i^{Ej}$ proportional to its length variation (Figure III.13), which can be written:

$$\vec{F}_i^{Ej} = k(\| \vec{p_i g_i} \| - L_i) \frac{\vec{p_i g_i}}{\| \vec{p_i g_i} \|} \tag{III.6}$$

where each spring is indexed with the letter $i \in [1, n]$. Each specimen edge is noted Ej ($j \in [1, 4]$). p_i refers to the spring attachment point on the sample along edge Ej and g_i to the spring end hooked onto the grip Gj. Grips have been noted Gj with the number j corresponding to the sample edge Ej to which they are linked.

Eventually, each spring force $\vec{F}_i^{Ej}$ can be seen as the sum of its two components:

$$\vec{F}_i^{Ej} = \vec{N}_i^{Ej} + \vec{T}_i^{Ej} \tag{III.7}$$

where $\vec{N}_i^{Ej}$ is the force component normal to edge Ej, and $\vec{T}_i^{Ej}$ is the force component tangent to edge Ej (Figure III.13-detail A).

4.3.2.ii) *Resulting load* To characterize the sample mechanical behavior, macroscopic stress quantities are required and defined.

The force measured by grips load-cell is noted $\vec{F}_{Gj}$ and will be compared to the corresponding macroscopic force measured via the springs system $\vec{F}_{spring}^{Ej}$ defined as:

$$\vec{F}_{spring}^{Ej} = \sum_i \vec{F}_i^{Ej} \tag{III.8}$$

4.3.2.iii) *Stresses* The nominal stress (Piola-Kirchoff stress) is computed using macroscopic forces $\vec{F}_{Gj}$ provided either by the grips load-cell or the springs system $\vec{F}_{spring}^{Ej}$. Using the force provided by the grip load-cell $\vec{F}_{Gj}$, a first definition of stress components have been chosen:

$$\sigma_{xx}^G = \frac{\left\| \vec{F}_{G4} \right\|}{b_0 \; e_0} \text{ and } \sigma_{yy}^G = \frac{\left\| \vec{F}_{G1} \right\|}{a_0 \; e_0} \tag{III.9}$$

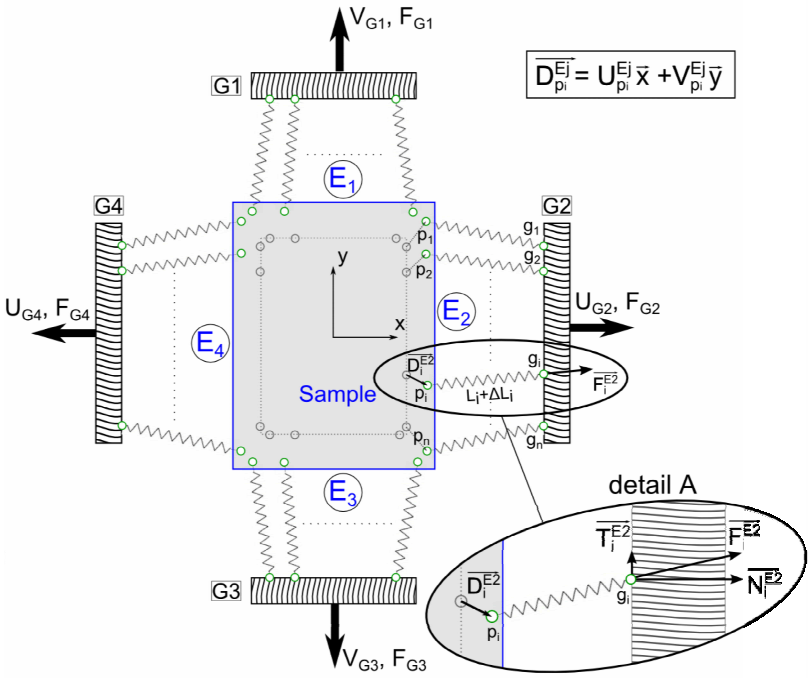

Figure III.13. Notations and labels used in the experimental setup.

Similarly, using the force measured by the springs system $\overrightarrow{F}^{Ej}_{spring}$, another Piola-Kirchoff stress can be defined in a similar way:

$$\sigma^E_{xx} = \frac{\left\| \overrightarrow{F}^{E4}_{spring} \right\|}{b_0\ e_0} \quad \text{and} \quad \sigma^E_{yy} = \frac{\left\| \overrightarrow{F}^{E1}_{spring} \right\|}{a_0\ e_0} \tag{III.10}$$

4.3.2.iv) *Sample strains* Strains used in this paper are logarithmic strains (Hencky formulation) to assess for large deformations. Attachment points spatial coordinates have been noted $x^{Ej}_{p_i}$ and $x^{Ej}_{0p_i}$ along the X axis and $y^{Ej}_{p_i}$ and $y^{Ej}_{0p_i}$ along the Y axis at current and initial times, respectively.

Likewise, grip spatial coordinates have been noted x_{Gj} and x_{0Gj} along the x axis and y_{Gj} and y_{0Gj} along the y axis at current and initial times, respectively. Grips displacements can be defined as (Figure III.13):

$$U_{Gj} = x_{Gj} - x_{0Gj} \quad \text{and} \quad V_{Gj} = y_{Gj} - y_{0Gj} \tag{III.11}$$

The DIC analysis performed on pictures of the sample loaded area provides the local strain field components ϵ_{xx} and ϵ_{yy}. The averaged values ϵ^{DIC}_x and ϵ^{DIC}_y can be computed as:

$$\epsilon^{DIC}_x = mean(\epsilon_{xx}) \quad \text{and} \quad \epsilon^{DIC}_y = mean(\epsilon_{yy}) \tag{III.12}$$

Other macroscopic strains have been defined using the mean distance between attachment points edge to edge, as:

$$\epsilon^E_x = \ln(1 + \frac{mean(x^{E2}_{p_i} - x^{E4}_{p_i})}{a_0}) \quad \text{and} \quad \epsilon^E_y = \ln(1 + \frac{mean(y^{E1}_{p_i} - y^{E3}_{p_i})}{b_0}) \tag{III.13}$$

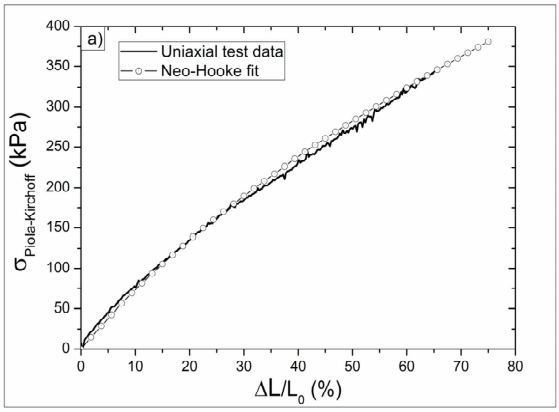

Figure III.14. Monotonic unixial test data of silicone and identification of a Neo-Hookean behavior model.

A third calculation of the sample macroscopic strains ϵ_x^G and ϵ_y^G has been proposed using only machine measurements (grips displacements U_{G4} and V_{G1} and grips forces $\vec{F}_{G4}$ and $\vec{F}_{G1}$ as:

$$\begin{aligned} \epsilon_x^G &= \ln\left(1+\frac{\Delta L_X}{a_0}\right) \text{ where } \Delta L_X = 2\times\left(U_{G4}-\frac{\left\|\vec{F}_{G4}\right\|}{K_{eq}}\right) \\ \epsilon_y^G &= \ln\left(1+\frac{\Delta L_Y}{b_0}\right) \text{ where } \Delta L_Y = 2\times\left(V_{G1}-\frac{\left\|\vec{F}_{G1}\right\|}{K_{eq}}\right) \end{aligned} \tag{III.14}$$

where K_{eq} is the springs equivalent stiffness used to evaluate the averaged springs length variation. Assuming that the springs remain parallel and normal to their attachment edge during testing, the approximate equivalent stiffness is given by $K_{eq} = n \times k$ (Eq. III.14).

Those three macroscopic strains definitions have been compared to assess the accuracy of the proposed control methods. The error associated to the equivalent stiffness K_{eq} approximation has also been studied in Section 4.4.3.

4.3.3 Specimen

A charged silicone elastomere RTV 3428 (BlueStar Silicone, Saint-Fons, France) has been used and prepared using the methodology of Machado *et al.* and Rey *et al.* [93, 94]. This silicone is highly resistant to tearing and possesses recoverable strains up to 300%, low viscoelasticity, and is initially isotropic. The material has been formerly mixed with a hardener with a weight ratio of 1/10, degased, and injected into a mold under near vacuum atmosphere. The 2.2 mm thick membrane is then cured in an oven at 70^{o}C during 4 hours. The silicone mechanical behavior in uniaxial tension is drawn in solid line in Figure III.14.

The sample used for biaxial test was of 50x50 mm area and cut from the membrane with a precision knife. A black paint speckle has been realized on the inner zone of interest with an airbrush, delimiting a centered zone of interest of 44x44 mm (Figure III.12b). This speckle will be used to experimentally compute the sample strain fields using DIC.

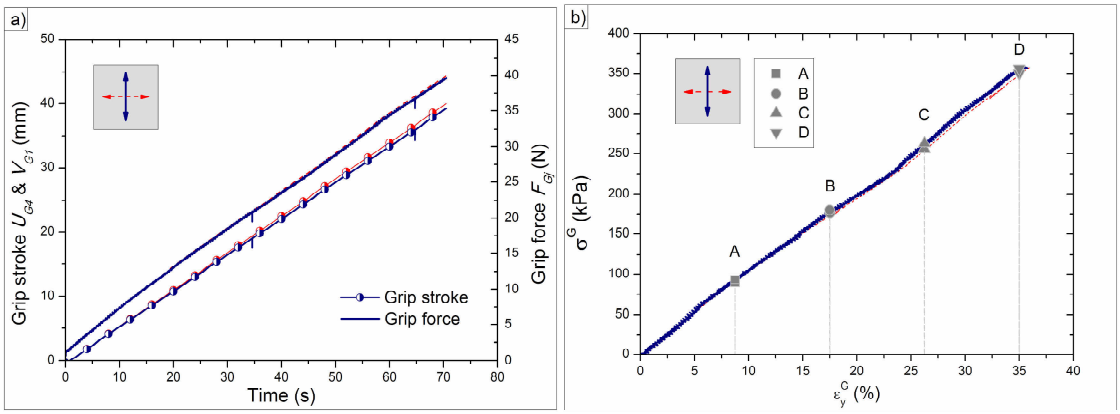

Figure III.15. a) Grips displacement (left scale) and resulting reaction forces (right scale), b) Stress/strain macroscopic behavior.

4.4 Experimental Results

4.4.1 Macroscopic behavior

The loading cycle has been controlled using the sample macroscopic strains ϵ_x^E and ϵ_y^E (Eq. III.13). The measurement of ϵ_x^E and ϵ_y^E has been performed in real time using a target tracking software linked with the machine pilot software. An optimal solution would be to use the strain provided by DIC measurement inside the sample ϵ_x^{DIC} and ϵ_y^{DIC} (Eq. III.12). However, DIC measurement can not be performed in real time by our system; the values ϵ_x^{DIC} and ϵ_y^{DIC} can not be used to control the test.

A specimen has been stretched via 4 sets of 19 springs. An equibiaxial loading cycle is performed on the virgin sample (no Mullins effect [57]) up to a maximum logarithmic strain $\epsilon_{max}^E = 35\%$ at a strain rate of 0.48 s^{-1} in both directions. The reaction forces from load cells $\vec{F}_{Gj}$ (Figure III.15a) and grip displacements allow to compute the macroscopic stress σ^G versus strain ϵ^G relations using Eqs. III.9 and III.14 (Figure III.15b). The curves overlap; the sample mechanical response is identical in both directions due to isotropy and equibiaxial loading. Only results on the vertical direction will be retained for further macroscopic studies.

Four specific times have been presented in this section. These specific times have been referred to as states A, B, C, & D corresponding to macroscopic strains ϵ_y^E of 9%, 17.5%, 26%, and 35% respectively.

Force distributions along the specimen edges have been first investigated in Section 4.4.2. The results of the three different macroscopic strains definitions are then compared in Section 4.4.3 before presenting the obtained experimental strain fields in Section 4.4.4.

4.4.2 Force distributions

The distributions of normal $\overrightarrow{N}_i^{Ej}$ and tangential $\overrightarrow{T}_i^{Ej}$ components of spring forces $\vec{F}_i^{Ej}$ (Eq. III.7) along the specimen boundaries are first presented (Figures III.16 & III.17).

The normal force distribution $\overrightarrow{N}_i^{Ej}$ presents an increase at each sample corner (Figure III.16). Springs number 1 and 19 differ from the mean value by 12% and springs 2 and 18 by 6.5% approximately at every step time A to D. The force distributions between springs 3 to 17 remain

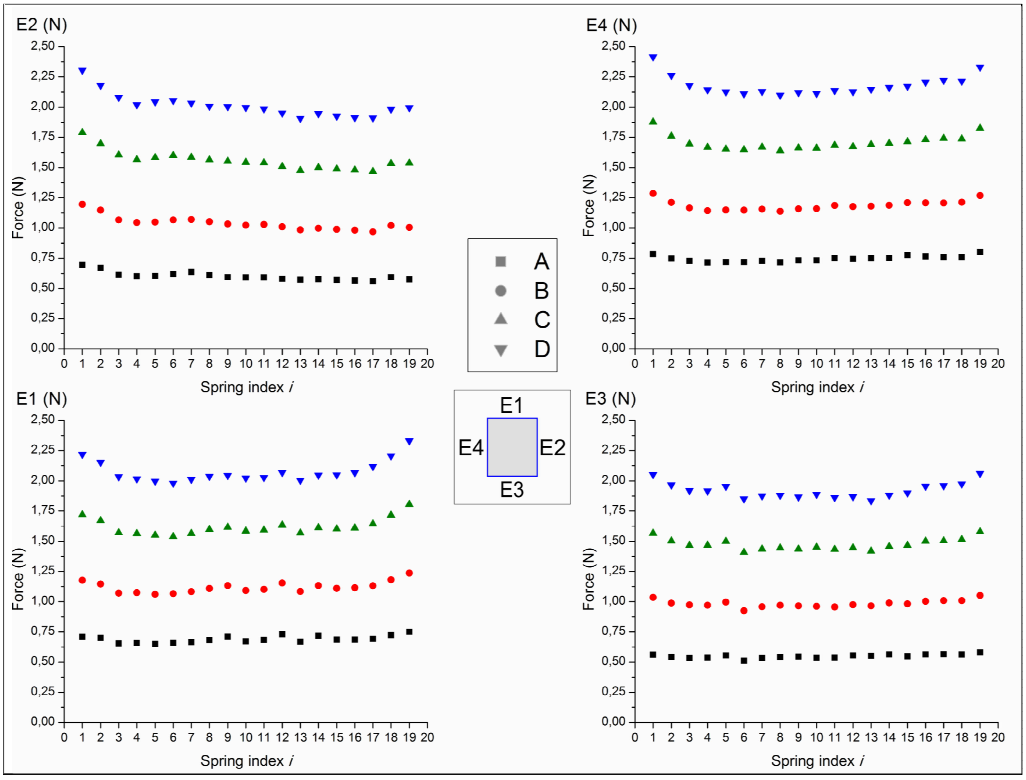

Figure III.16. Normal forces along specimen boundaries with 19 springs. A: $\epsilon^E_{max} = 9\%$, B: $\epsilon^E_{max} = 17.5\%$, C: $\epsilon^E_{max} = 26\%$, D: $\epsilon^E_{max} = 35\%$.

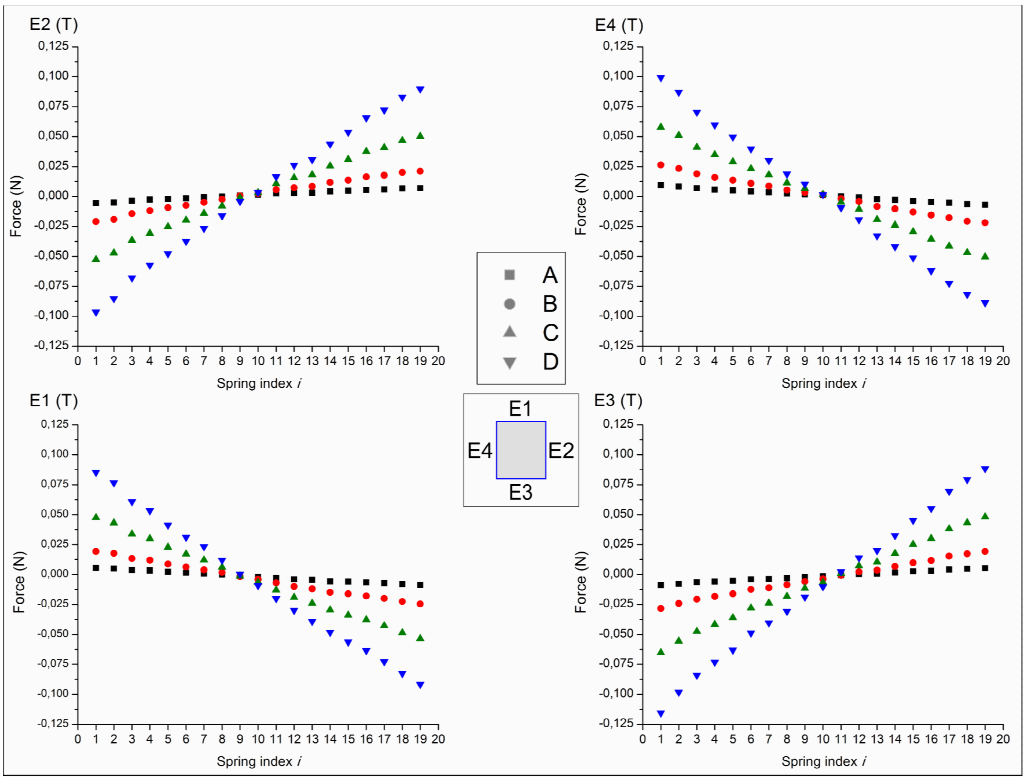

Figure III.17. Tangential forces along specimen boundaries with 19 springs. A: $\epsilon^E_{max} = 9\%$, B: $\epsilon^E_{max} = 17.5\%$, C: $\epsilon^E_{max} = 26\%$, D: $\epsilon^E_{max} = 35\%$.

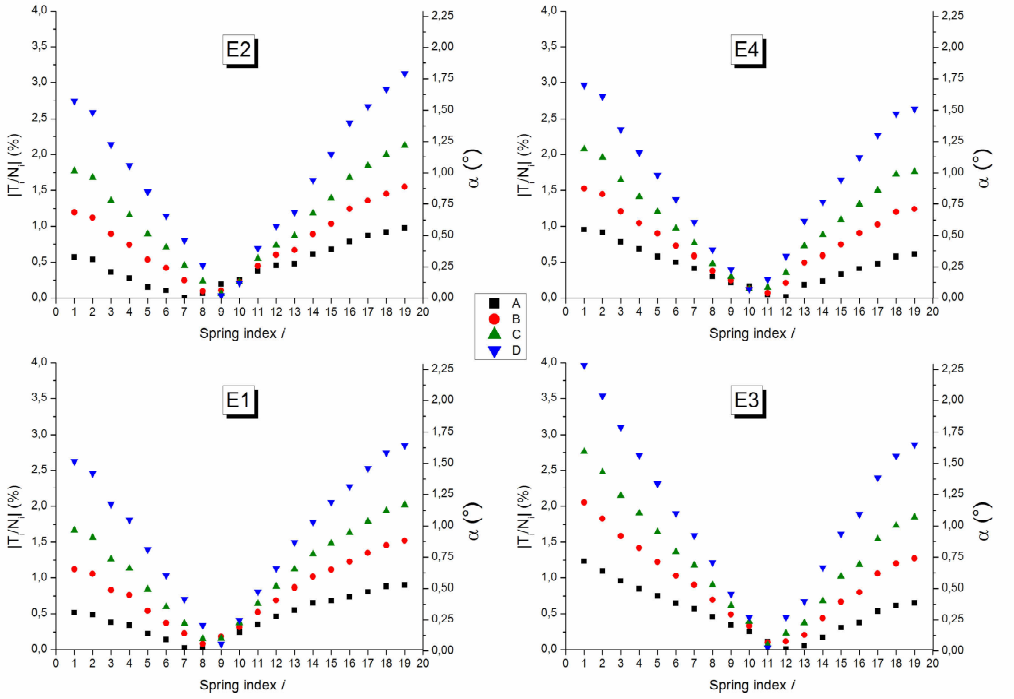

Figure III.18. Ratio of tangential over normal springs forces on sample boundaries. A: $\epsilon^E_{max} = 9\%$, B: $\epsilon^E_{max} = 17.5\%$, C: $\epsilon^E_{max} = 26\%$, D: $\epsilon^E_{max} = 35\%$.

uniform with a standard deviation inferior to 3%.

As expected, the central spring tangential force $\overrightarrow{T_i}^{Ej}$ is equal to zero (Figure III.17): the tangential force distributions are symmetrical due to sample, mounting, and grips displacement symmetries. In theoretical biaxial tests, only normal forces should be applied on sample edges. Therefore, the influence of tangential force shas been qualified using a criterion R defined as:

$$R = \frac{\left\| \overrightarrow{T_i}^{Ej} \right\|}{\left\| \overrightarrow{N_i}^{Ej} \right\|} \tag{III.15}$$

The ratio R presents a symmetrical distribution along each edge, with a maximum value of 4%, which is considered negligible (Figure III.18).

4.4.3 Comparison of macroscopic strains

The experimental results obtained with the three definitions of the sample macroscopic strains have been compared (Figure III.19a). The strains measured with DIC analysis ϵ^{DIC} present lower values than strains measured via grip displacements ϵ^G and targets positions ϵ^E, with a maximum relative difference of 7.7% relatively to ϵ^{DIC}. The target and grip strains ϵ^E and ϵ^G overlap. These macroscopic strains have been used to control the test targeted strain by compensating the deviation with respect to the DIC strains ϵ^{DIC}.

Then, stresses obtained from grip forces and displacements $\sigma^G_{yy} = \left\| \vec{F}_{G1} \right\| / S_0^{E1}$ (Eq. III.9) and spring forces $\sigma^E_{yy} = \left\| \sum_i \overrightarrow{F_i}^{E1} \right\| / S_0^{E1}$ (Eq. III.10) have been plotted versus the sample macroscopic strains ϵ^G_y and ϵ^E_y, respectively, and compared (Figure III.19b). The macroscopic stress σ^E_{yy}

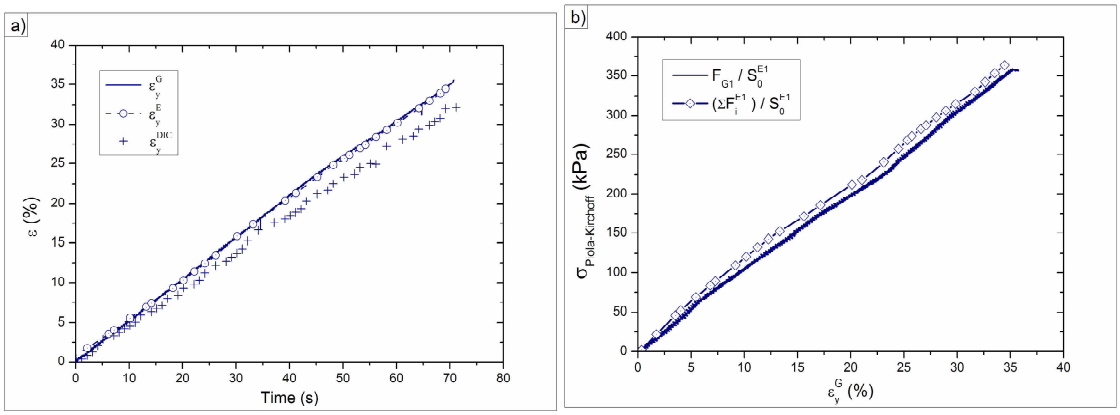

Figure III.19. a) Comparison of macroscopic strains measurements and b) stress/strain relations calculated from grip measured forces and summed spring forces.

measured by the spring system overestimates the macroscopic stress σ_{yy}^G measured using grips forces by 15% at 12% strain and 3.7% at 35% strain, maximum and minimum errors respectively.

4.4.4 Strain Fields

The DIC strain fields maps have been plotted for each time A, B, C, and D, in order to assess the strain uniformity inside the sample working area (Figure III.20). The three in-plane components have been plotted (*i)* to *iii)*), with the same scale for ϵ_{xx} and ϵ_{yy}. To study the equibiaxiality of the strain field components observed on the macroscopic behavior of the sample (Figure III.15b), the absolute difference $|\epsilon_{xx} - \epsilon_{yy}|$ is also computed (*iv)*). This absolute difference is then normalized using the mean DIC strains ϵ_x^{DIC} and ϵ_y^{DIC} (Eq. III.12) as:

$$h = \frac{|\epsilon_{xx} - \epsilon_{yy}|}{(\epsilon_x^{DIC} + \epsilon_y^{DIC})/2} \tag{III.16}$$

This calculation has been performed to highlight zones where strains are uniform relatively to the mean strain (*v)*). Areas where strains are matching the criterion $0\% \leq h \leq 5\%$ have been countoured in white. The size of such areas relatively to the zone of interest area has been marked into these areas.

4.5 Analysis

4.5.1 Macroscopic behavior

The measurement of macroscopic strains estimated from grip load-cell forces and displacements ϵ_x^G (Eq. III.14) and targets position variations ϵ_x^E (Eq. III.13) overlaps (Figure III.19a). Either data set used to control the macroscopic strain level during the test will provide the same control quality.

However, mean DIC strains ϵ_y^{DIC} (Eq. III.12) return a lower value than grips and targets measured strains ϵ_y^G and ϵ_y^E. This difference is explained by the deformation of attachment holes. These holes deformations induce a lower strain state inside the sample compared to the strain computed directly from attachment points displacements.

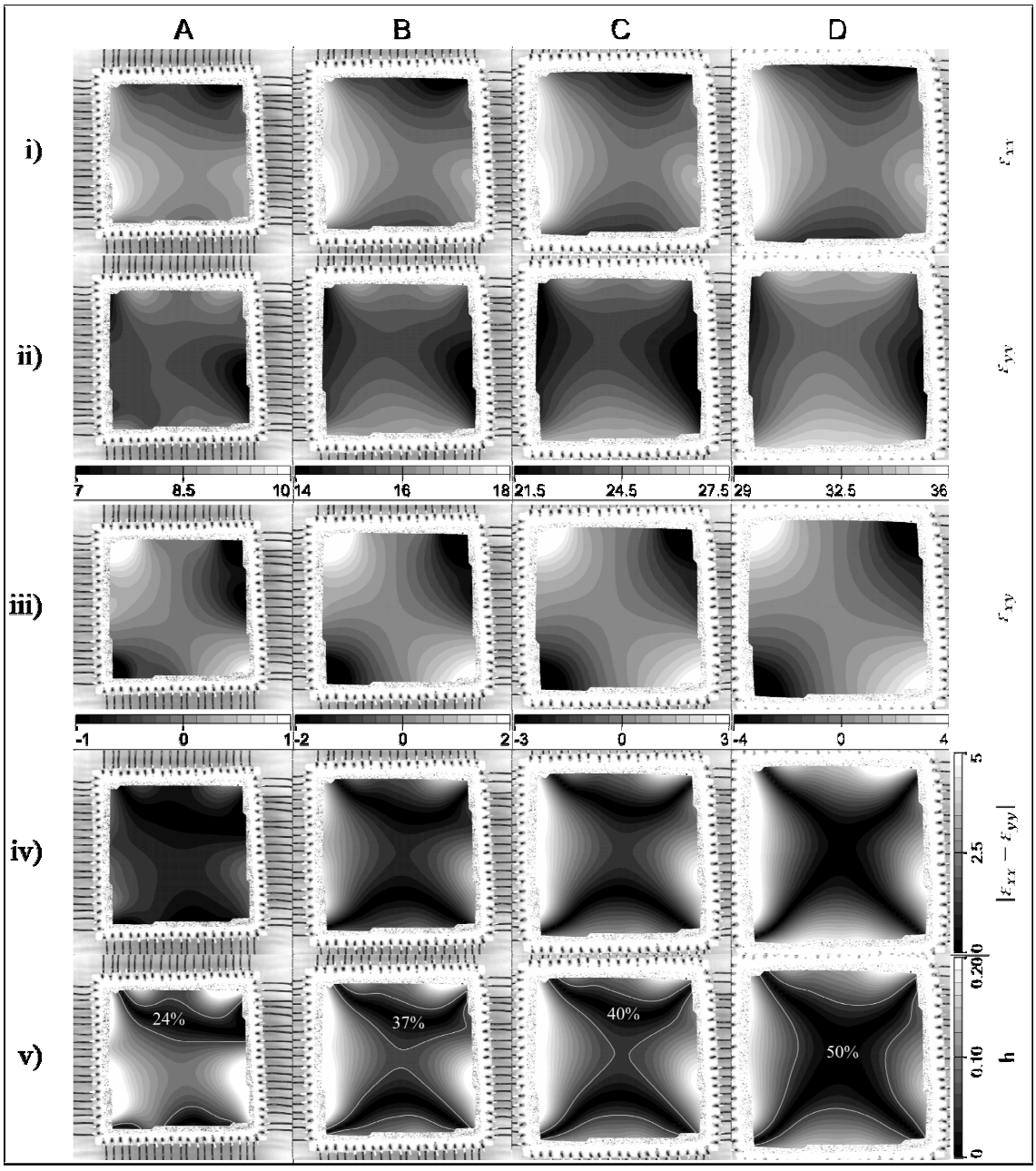

Figure III.20. i, ii, and iii) Strain field components (%), iv) absolute difference of the strain field components ϵ_{xx} and ϵ_{yy} (%), v) normalized absolute difference of the strain field components. A: $\epsilon^E_{max} = 9\%$, B: $\epsilon^E_{max} = 17.5\%$, C: $\epsilon^E_{max} = 26\%$, D: $\epsilon^E_{max} = 35\%$.

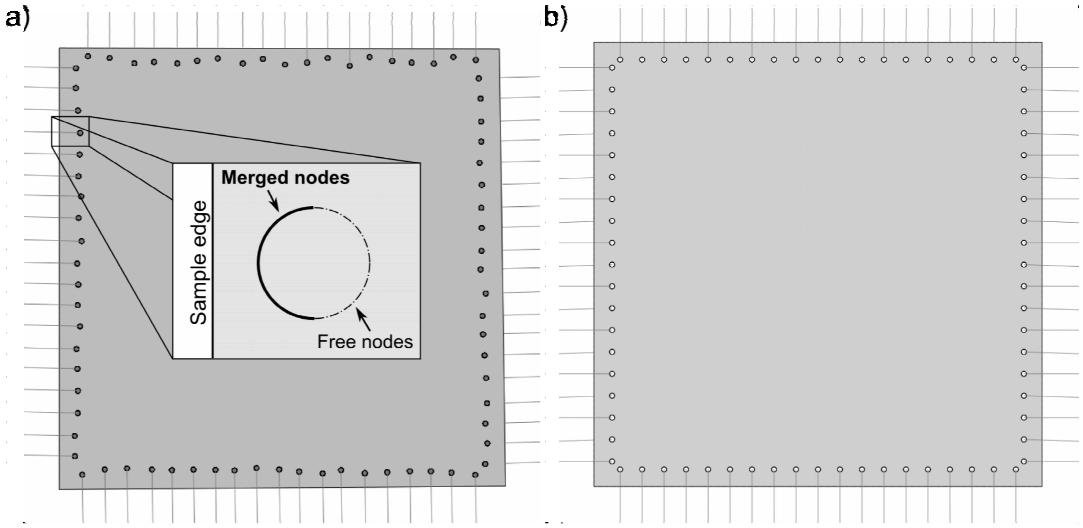

Figure III.21. Geometry of finite elements models with a) experimental hooks disposition and b) ideal hooks disposition.

Moreover, as expected, stresses deduced from grip forces σ_{yy}^{G} (Eq. III.9) and springs macroscopic forces σ_{yy}^{E} (Eq. III.10) are similar and validate the measurement of spring forces (Figure III.19b).

4.5.2 Strain fields

Despite the applied equibiaxial boundary conditions, the strain field components ϵ_{xx} and ϵ_{yy} are not perfectly symmetrical, which is underlined by the difference $|\epsilon_{xx} - \epsilon_{yy}|$ (Figure III.20, lines i), ii), iv) respectively). This difference is caused by symmetry defects of attachment points placement, springs characteristics deviations, and sample internal defects. The error on attachment points placement impact will be further analyzed in Section 4.5.3.

Strain field uniformity has been characterized using relative strain h maps (Eq. III.16, Figure III.20 v). Strain field is considered uniform where $h \leq 0.05$. The area where this criterion is verified is outlined in white and observed firstly on the upper third of the sample, and then grows as the sample is stretched. At maximum stretch, this zone covers approximately 50% of the sample speckled area, in accordance with literature [83]. The increasing stress produces a more uniform strain field inside the sample zone of interest.

4.5.3 Finite Elements model

Finite elements models have been created using a finite elements software (Abaqus, DDS Dassault Systemes, France). The model aimed at proposing a simple yet effective simulation to enable optimizing experimental parameters such as springs characteristics, specimen shape, *etc.* This model also provides insight to study the impact of springs attachment points placement on boundary forces distributions and strain field uniformity. Models using perfect and experimental hooks implantation schemes have been first realized (Figure III.21).

Hooks circular sections have been defined as rigid bodies and their perimeter nodes have been merged with specimen nodes on the outward pointing semicircle to study holes deformation upon

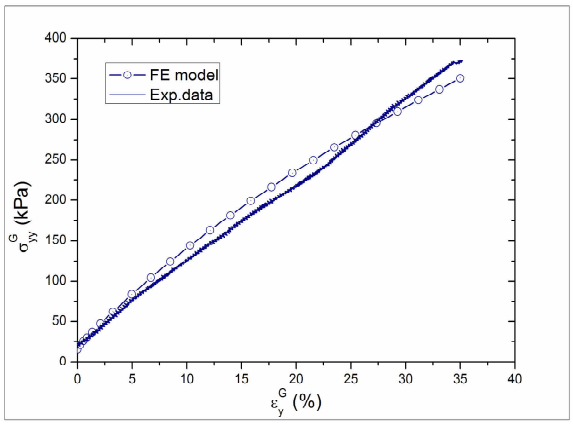

Figure III.22. Comparison of stress/strain relations between experiment and FE model with experimental hooks disposition.

loading as observed experimentally.

A Neo-Hookean hyperelastic material model has been used to simulate the material mechanical behavior and has been fitted on uniaxial tensile tests realized on virgin samples (Figure III.14). The strain energy density function requires the two mechanical parameters $C10$ and $D1$. The resulting parameter $C10$ is found equal to 0.131 MPa, and $D1$ is taken equal to 10^{-4} MPa^{-1}, corresponding to a Poisson's coefficient of 0.4999, to simulate the silicone quasi-incompressibility.

Those models have been validated by comparing experimental and model results on the sample macroscopic stress σ^G_{yy} (Eq. III.9) versus strain ϵ^G_y (Eq. III.14) (Figure III.22). The macroscopic stress deduced experimentally from grips force σ^G_{yy} is properly simulated with a difference lower than 8.5%. Even if the Neo-Hookean non-linearity observed on the fitted curve diverges from experimental results, the model is considered validated in regard to the macroscopic behavior of the sample.

Normal forces $\vec{N}_i^{Ej}$ distributions have then been compared between FE analysis and experimental results (Figure III.23). For concision sake, only experimental and numerical results on edges E1 and E4 have been compared. The normal forces $\vec{N}_i^{Ej}$ distributions with experimental placement of hooks (solid lines) are well predicted by the model compared to experimental distributions, with a maximum deviation of 11% on edge E1 at step B, and 8.5% on edge E4 at step D.

The normal forces $\vec{N}_i^{Ej}$ distributions of the model using ideal placement of attachment points (dash lines in Figure III.23) highlights that errors in springs attachment points placement are responsible for small variations in the normal forces values. These variations are of an order of 4% at maximum value. The increase seen on normal forces distributions borders are observed independently of springs placement errors. These gradients were caused by the peripheral material situated behind hooks (between attachment points and sample outer edges). Numerical tests (not presented in this paper) highlight that the thinner this part is, the lower the increases at the sample corners are.

Finite elements models also provide analysis on the differences observed experimentally on the three sample strains formulations ϵ^{DIC} versus ϵ^G and ϵ^E (Eq III.12, III.13, and III.14) (Figure III.24). The same relative difference is found on the mean strain in the sample working area ϵ^{DIC} as opposed to the value measured via grips ϵ^G and targets ϵ^E, confirming that holes defor-

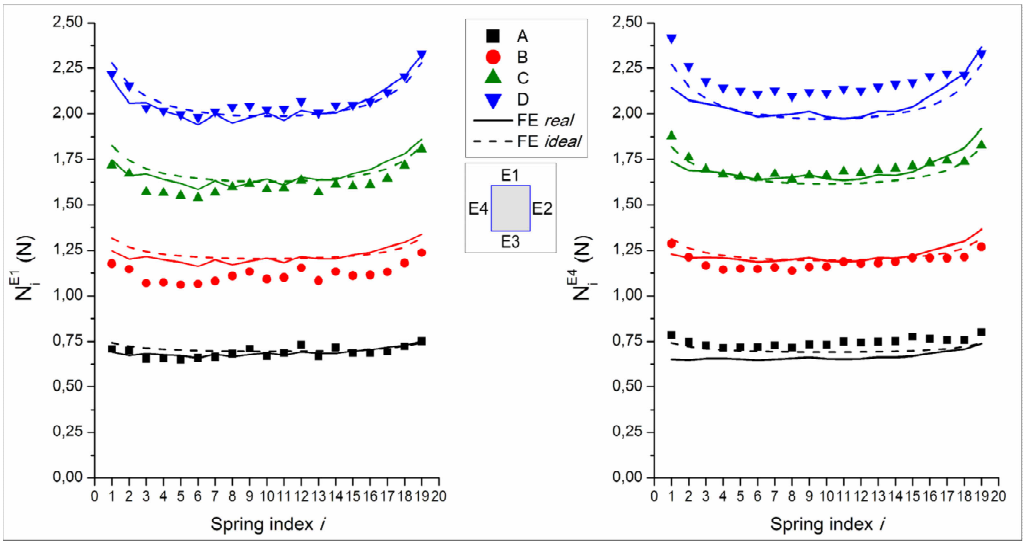

Figure III.23. Comparison of spring normal forces between experiment (symbols), FE model with experimental hooks disposition (solid lines), and FE model with ideal hooks disposition (dash lines). A: $\epsilon^E_{max} = 9\%$, B: $\epsilon^E_{max} = 17.5\%$, C: $\epsilon^E_{max} = 26\%$, D: $\epsilon^E_{max} = 35\%$.

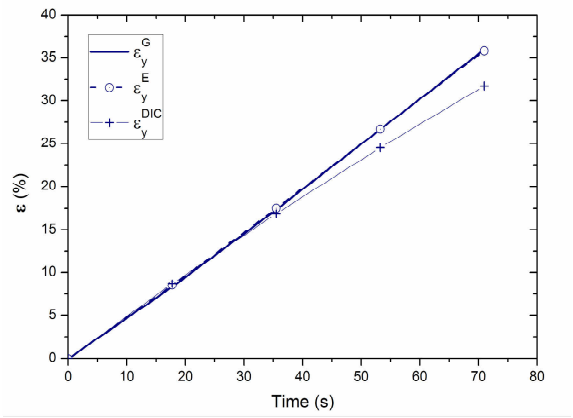

Figure III.24. Comparison of macroscopic strains calculations using the FE model with ideal hooks placement.

mation causes such sample strains deviation.

Finite elements strain field components ϵ_{xx}, ϵ_{yy}, and ϵ_{xy} maps have also been plotted to observe strain non-uniformities when experimental attachment points placement is simulated (Figure III.25). Strain field components maps highlight strain concentrations around attachment points as could be expected for such a setup. These heterogeneities at the sample edges were not symmetrical as experimental attachment positions have been implemented in the model. Strain heterogeneities were not directly related to normal forces distributions as higher forces value does not implies higher strain value in the attachment point neighborhood.

Unfortunately, strains concentrations are over-estimated by the model. The shear strain is specifically over-estimated by a factor 2 as opposed to experimental data (Figure III.25 iii).

A model ignoring every incertitude related to springs characteristics, placement, sample homogeneity, symmetry defects, and calculation approximation has been created. As expected, this

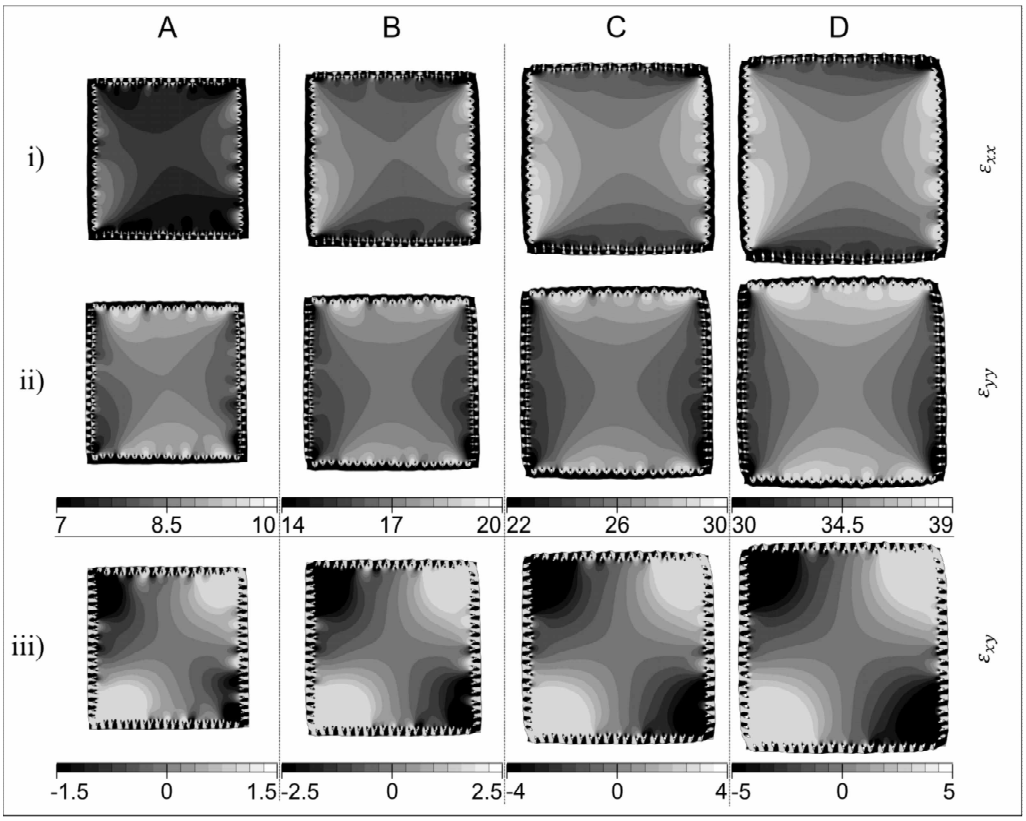

Figure III.25. Strain field components (%) for the finite element model with experimental hooks disposition. A: $\epsilon^E_{max} = 9\%$, B: $\epsilon^E_{max} = 17.5\%$, C: $\epsilon^E_{max} = 26\%$, D: $\epsilon^E_{max} = 35\%$.

model presents non-uniform yet symmetrical strain field components (Figure III.26). As opposed to the real implantation scheme, for time A, B, and C, strain concentrations area around attachment points were smaller. Uniformity criterion h (Eq. III.16) maps obtained with such model are symmetrical and uniform through time. The size of the uniform area $h \leq 0.05$ decreases slightly from 54% to 51% of the sample loaded area. The last results is similar to results obtained experimentally (Figure III.20)

The placement of spring attachment points thus possesses a limited impact on strain field uniformity inside the sample working area, considering the standard deviation of hooks placement around the ideal position is as small as $\pm 0.3mm$ (equal to the hooks radius). Optimizing such placement yields very small strain field uniformity improvement in return.

4.5.4 Improvement perspectives

It has been shown that small deviations in the placement of springs attachment points were responsible for small deviation of approximately 4% of normal forces distributions along the sample edges, and partially responsible for strain non-uniformities. A special care may yet be taken to place hooks precisely to reduce such deviations.

Springs initial and final length (L_i and $L_i + \Delta L$ respectively) impact the value of the ratio R (Eq. III.15); R criterion and tangential forces are needed to be as small as possible. Springs parameters such as initial length L_i and stiffness k have to be adjusted to comply with machine constraints and to have the greatest final length available so as to reduce the tangential spring

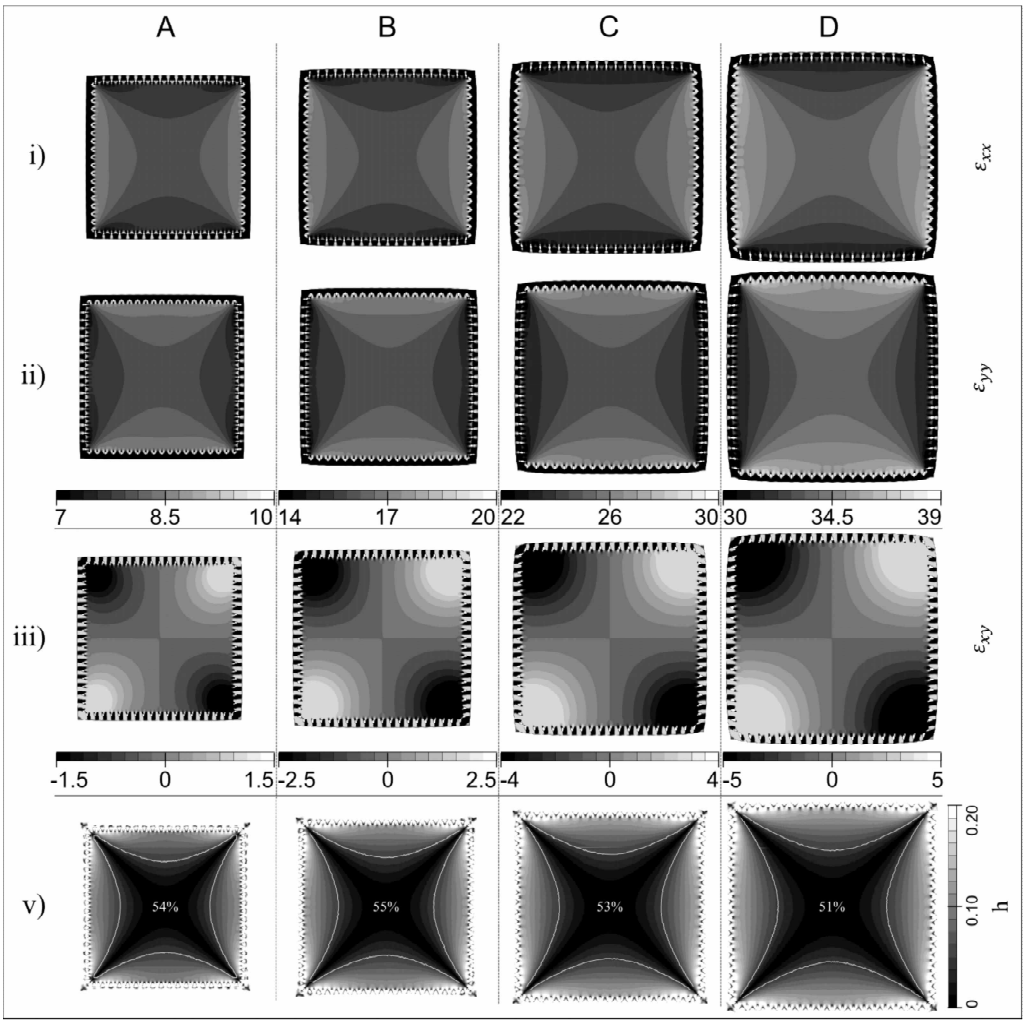

Figure III.26. Strain field components (%) and normalized absolute difference of the strain field components for the finite element model with ideal hooks disposition. A: $\epsilon^E_{max} = 9\%$, B: $\epsilon^E_{max} = 17.5\%$, C: $\epsilon^E_{max} = 26\%$, D: $\epsilon^E_{max} = 35\%$.

forces intensity, and therefore to diminish the ratio R.

Finite elements models can be used to optimize such an experiment and to study the influence of the sample geometry on the strain fields uniformity. The distance between external springs of each edge may be responsible for high stress concentration and the influence of such parameter have to be studied. Furthermore, the size of the excess of material behind the springs attachment points may induce force distributions gradients and should be analyzed.

4.6 Conclusion

The setup presented in this paper has been used to perform equibiaxial tensile tests on a silicone membrane. Using an uniformity criterion $h \leq 5\%$, a uniform strain field is obtained over 50% of the sample zone of interest.

The developed method also provides boundary conditions measurement such as displacements and forces distributions. The resulting boundary forces measured using springs have been shown to match forces measured using grips load-cell. Boundary forces distributions have been shown

to be partially dependent on the precision with which hooks have been placed. Errors of ± 3 mm resulted in a maximum deviation of 4% of normal forces distributions.

In theory, planar biaxial tests only result in normal forces applied on the sample boundary. A ratio of tangential over normal forces R lower than 5% has been obtained experimentally, which has been considered satisfactory.

DIC strain fields have been computed on images, and provide a measurement of the sample macroscopic strains. Two alternative definitions of such macroscopic strains have been proposed and provide a moderate error of less than 7.7%. Such definitions yet allows driving the test with ease and requires less complex real-time measurements.

Finally, a finite element model has been proposed and validated in regard to the sample macroscopic behavior and normal forces distributions along the sample edges. Such model provides satisfactory results to predict the impact and to optimize values of various parameters such as springs attachment point placement errors, springs number, springs characteristics, *etc*.

5 General conclusion

To experimentally study knitted textiles, a testing setup providing direct boundary load distributions measurement has been developed and validated using soft silicone membranes. An in-house developed software has been proposed alongside to analyze the textile structure evolution on experiment pictures. These data grant access to several key parameters of the textile deformation, gliding, local curvature, *etc*, that are not obtainable by common DIC methods. This program has been developed specifically for knitted textiles and uses their particular inner structure to perform tracking of stitches. An illustration example presented similar displacement fields between the two image analysis method obtain on experimental pictures. It has been shown that the average error in displacement measurement is lower than 4%. Only few critical points show higher errors which is induced by DIC method errors on the area of interest edges. This error is considered acceptable has standard DIC can not precisely detect the difference between two consecutive knit loops. Yet few drawbacks are to be noted, such as the time-efficiency of the method and the restrictive application that requires only weft knitted textile.

Those experimental tools can also be used to validate analytical and/or numerical tools.

CHAPTER

IV Numerical analysis tool

1 Introduction

In this chapter is presented the finite elements model used to study knitted NiTi textiles. It aims at studying stresses and strains distribution and evolution, material parameters and geometry dimensions influence, *etc*. Analytical models are limited (loading case, loop geometry, *etc*.) and numerical models are either highly simplified (no bending, no friction, *etc*. [88]) or computation heavy (3D elements [79], no periodicity, *etc*.). This model is inspired by models presented in Chapter II [18, 88, 89], and tends to combine advantages of each model.

The used geometry is based on a single loop which represents the textile Representative Element Volume (RVE). A set of parametric equations has been written to describe the knit loop geometry (Vokoun & Heller). Considering the wire curvilinear length over diameter ratio, beam elements have been used to reduce the model size.

The knit loop deformation is constrained by periodic boundary conditions (homogenization method). Continuity boundary conditions have also introduced to constrain the deformed geometry periodicity due to the presence of rotational degrees of freedom. The contact management is performed via general contact definition.

2 Stitch finite elements model

The finite elements model aims at providing with information on the local wire stress-strain state, which can not be obtained experimentally. Furthermore, the finite element model allows performing simulation on various knit loop size and geometry, various material quantities, *etc*., to study the impact of such parameters on the textile behavior.

In Section 2.2, the knitted NiTi textile studied has been briefly introduced. It can be seen on pictures (Figure III.2) that the wire diameter is small compared to the loop curvilinear length. Therefore, to simplify the finite element model and reduce calculation time, beam finite elements are used to mesh the loop.

The material model used to model the wire superelastic behavior is first presented in Section 2.1. The knit loop and the finite element model geometries are then introduced in Section 2.2. To verify the beam finite elements ability to reproduce a superelastic wire in simple bending, a

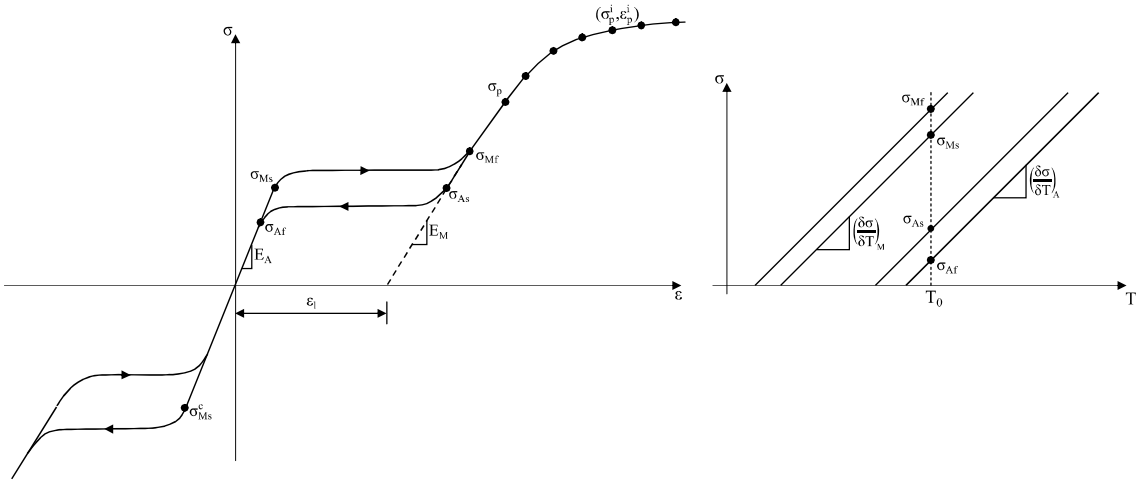

Figure IV.1. Aurrichio behavior model used to model the NiTi superelastic-plastic mechanical behavior.

benchmark is performed and presented in Section 2.3. Periodic boundary conditions are then formulated for beam elements in Section 2.4. Contact management methods between beam elements are then described depending on the resolution method used in Section 2.5.

2.1 Material Model

To model the NiTi wire superelastic mechanical behavior presented in Chapter II (Section 2.3), the Aurrichio behavior model has been used (Figure IV.1). This behavior model requires parameters listed below. In the stress/strain plane (σ, ϵ), the required parameters are:

- σ_{Ms}, σ_{Mf}: martensitic transformation start and end tensile stresses
- σ_{As}, σ_{Af}: austenitic transformation start and end tensile stresses
- σ_P, $(\sigma_P^i, \epsilon_P^i)$: martensite yield stress and yield curve points coordinates
- σ_{Ms}^c: martensitic transformation start stress in compression
- E_A, E_M: austenite and martensite Young's moduli
- ϵ_l: transformation strain
- ν_A, ν_M: austenite and martensite Poisson's coefficients

In the stress/temperature plane (Clausius-Clapeyron law), the additional required parameters are:

- $(\frac{\delta\sigma}{\delta T})_A$: austenitic transformation start stress variation versus temperature
- $(\frac{\delta\sigma}{\delta T})_M$: martensitic transformation start stress variation versus temperature
- T_0: temperature at which above parameters have been measured

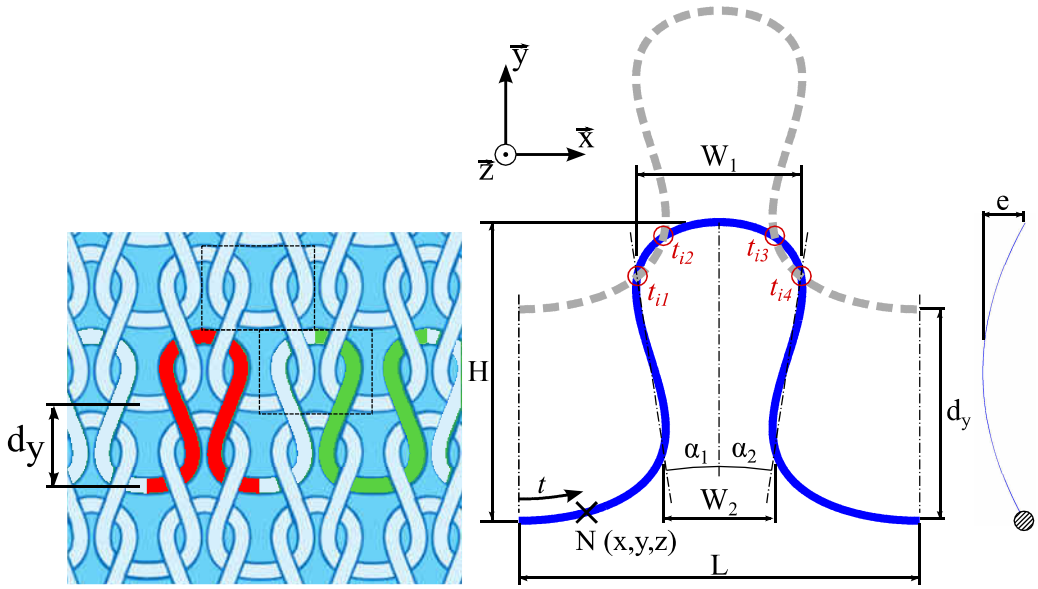

Figure IV.2. Left: Multiple repeating unit cell of a knit loop (red & green) or cut unit cell (dash squares); Right: Knit loop geometry and shape parameters

2.2 Loop geometry and shape parameters

2.2.1 Geometry equations

The knitted structure of a sample is a repetition of a unit cell, which can be defined in different ways (Figure IV.2, left). The knit loop geometry has been modeled using parametric equations and dimensional parameters along the course direction. The equations describe the undulating shape of the wire over a single knit loop.

A set of dimensional parameters has been used to describe the knit loop morphology (Figure IV.2), namely:

- L: the knit loop length,
- H: the knit loop height,
- W_1 & W_2: the knit loop large and small width of inner curvature,
- e: the knit loop thickness,
- d_y: the distance between two courses in the wale direction.

Additionally, to describe the loop shape and symmetry, three angles have been defined, namely α_1, α_2, and $\theta = \alpha_1 + \alpha_2$. For idealized textiles, α_1 and α_2 are equal. In the case of a physical textile, the manufacturing process induces defects in the loop symmetries. These defects can be partly quantified by the difference between those two angles. θ represents the knit loop opening.

These parameters allow the knit loop geometry to be defined with less loop shape restrictions as proposed in earlier models (Chapter II, Section 4.2.1). The spatial coordinates (x, y, z) of a

point N along the loop neutral axis can be determined from a parameter $t \in [0, 2\pi]$ referring to the normalized curvilinear abscissa of the point N (Eq. IV.1) and the equation defines below:

$$\begin{aligned} x &= L\,\frac{t}{2\pi} + k\sin(2t) + asm\sin(t) \\ y &= H\,\frac{cos(t)}{2} \\ z &= e\,\frac{St}{2\times|St|} \end{aligned} \tag{IV.1}$$

with

$$\begin{aligned} St &= \sin(\frac{\pi}{2} + 2(t - t_{i1})) + \sin(\frac{\pi}{2} + 2(t - t_{i4})) \\ &\quad - \sin(\frac{\pi}{2} + 2(t - t_{i2})) - \sin(\frac{\pi}{2} + 2(t - t_{i3})) \end{aligned} \tag{IV.2}$$

where k and asm are curvature parameters around dimensions W_1 and W_2 respectively. t_{i1}, t_{i2}, t_{i3}, and t_{i4} correspond to the intersection points between two course rows normalized curvilinear abscissa t.

2.2.2 Finite elements stitch geometry

The knit stitch geometry consists here only in the wire medium fiber. Such geometry is described using the parametric model presented in Section 2.2.1 and with experimental geometrical parameters obtained using the image correlation software presented in Section 2.2.

A quasi-infinite number of repeating patterns composes the knit structure. The finite element model geometry is chosen to represent a full knitted periodical structure as depicted in Figure IV.3 (green rectangle). The geometry is extracted using a box measuring L wide and d_y high, arbitrarily placed.

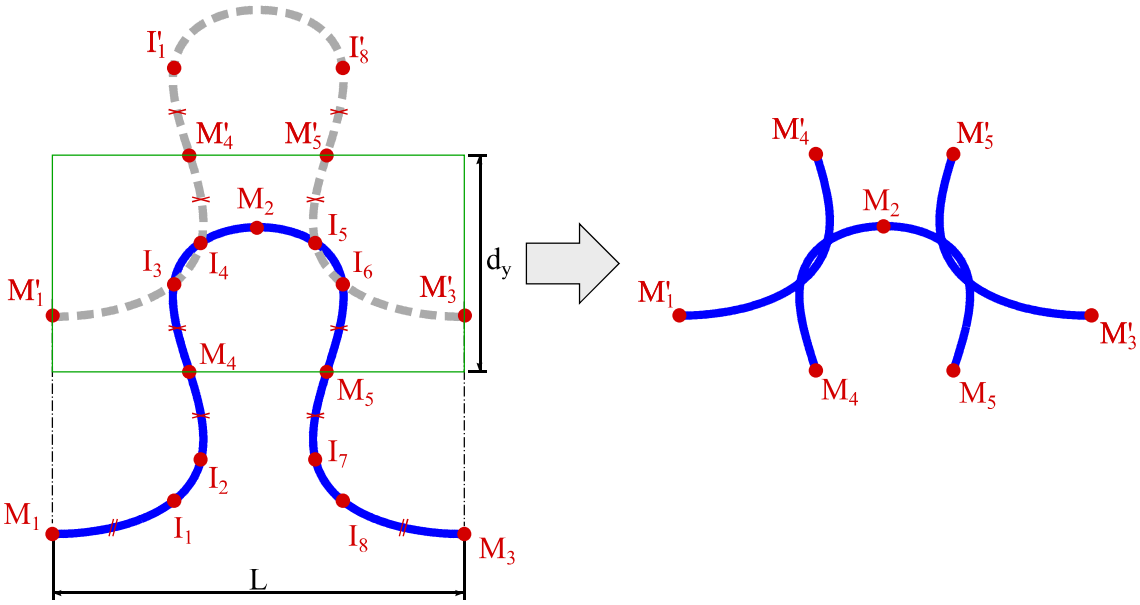

Figure IV.3. Creation of the finite elements model knit loop geometry and reference points for periodic boundary conditions.

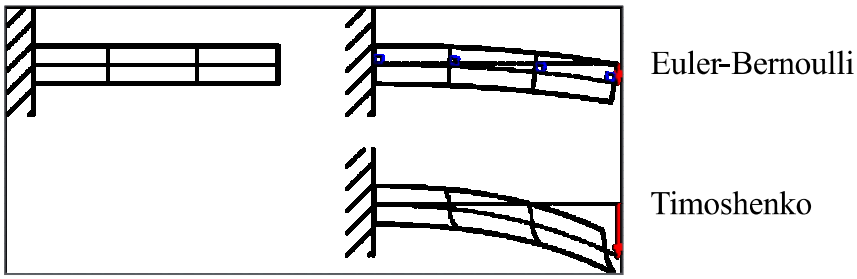

Figure IV.4. Schematization of initial (left) and deformed (right) beam according to Euler-Bernoulli (top) and Timoshenko (bottom)

2.3 Beam finite elements

2.3.1 Beam theory

Two main kinematic hypotheses sets exist to model beams: i) Euler-Bernoulli theory, and ii) Timoshenko theory (Figure IV.4).

Euler-Bernoulli formulation is the simplest formulation: the beam cross-section initially planar and perpendicular to the beam axis is supposed to remain planar and perpendicular to the beam axis when deformation occurs. This theory is valid for slender beams.

Timoshenko theory takes into account for cross-section deformation and is suitable for thicker beams. Using such formulation, the initially right and planar cross-section may deform under the effect of shear strains.

In this work, the wire superelastic behavior is expected to induce large bending with shear stress. The contact pressure is also expected to induce shear stress in the wire section. The Timoshenko formulation is therefore used in the model.

2.3.2 Beam finite elements

In beams, nodal displacements allow to compute the deformed shape of the structure and the nodal section strains ϵ and stresses σ. The section stresses are then used to compute the nodal bending moment M_b. Considering a 2D planar problem, the bending moment around z-axis M_{bz} can be computed as:

$$M_{bz} = \iint_S y\sigma_{xx} dS \tag{IV.3}$$

In order to numerically solve such integral, the trapezoidal rule is used with a certain number of integration points in the section. The default number is 3 points radially and 8 circumferentially, allowing for accurate material plasticity reproduction. The number of integration points can be user-defined in order to simulate more precisely more specific material behavior.

The NiTi wire superelastic behavior is non-linear and presents non-symmetric tension-compression. A benchmark in simple bending has thus been realized to determine the optimal number of integration points in the beam section to balance between precision and computation time. The benchmark geometry is presented in Figure IV.5. The model consists in a beam of length L, with a circular section of diameter d. The loading case consists in simple bending applied by a displacement U_y at the beam free extremity. Quadratic beam elements B32 have been used, of length 0.5 mm. Three number of integration points have been tested, namely 3x8, 9x8, and 15x8 (Figure IV.6, 15x8 is not represented for clarity reasons).

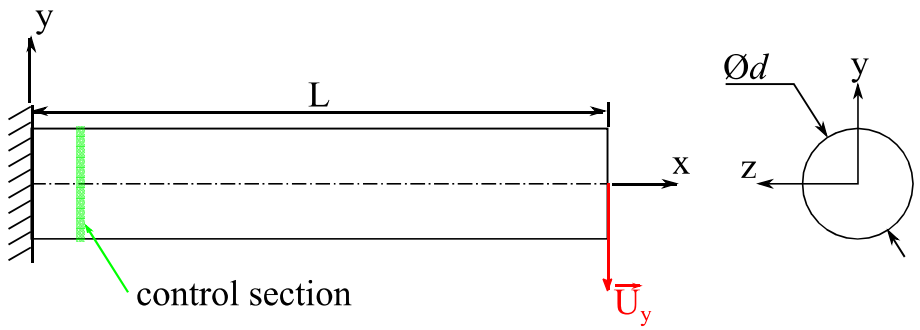

Figure IV.5. Beam bending benchmark performed to compare beam finite elements and standard 3D brick elements.

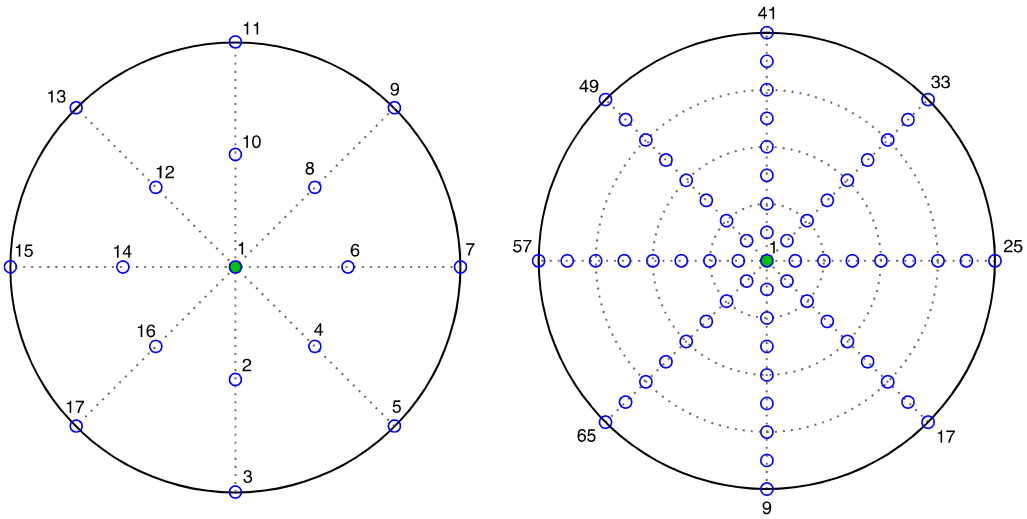

Figure IV.6. Illustration of the integration points organization and numbering in the section using default 3x8 integration (left) and user-defined 9x8 integration points (e_r x e_θ) (right)

Table IV.1. Geometrical and material parameters of the benchmark performed to compare 1D beam elements and 3D brick elements.

L	d	U_y	E_A	ν_A	E_M	ν_M	ϵ^{tr}	σ_{Ms}	σ_{Mf}	σ_{cs}
5 mm	0.4 mm	-5 mm	60 GPa	0.45	40 GPa	0.45	5 %	550 MPa	610 MPa	770 MPa

The benchmark geometrical and material parameters are summarized in Table IV.1.

The bending moment M_{bz} has been studied against the element curvature ρ for the three integration points number at the control section (Figure IV.7, green line), during a single loading cycle. It appears that the default integration diverge from the user-defined integrations by 16% at the martensitic transformation end, yet recovers identical bending moment for larger curvatures ($\rho \geq 0.9mm^{-1}$). Small difference can also be seen at the martensitic transformation start. However, both non-default integrations yield the same bending moment versus curvature relation, with a maximum difference equal to 5% at $\rho = 0.7mm{-}1$. The calculation times are summarized in Table IV.2. Increasing the number of integration points increases computation times, as expected. Therefore, to balance precision with computation times, it has been decided to use 9x8 user-defined integration points in the beam section, to represent the wire bending accurately while reasonably increasing calculation times.

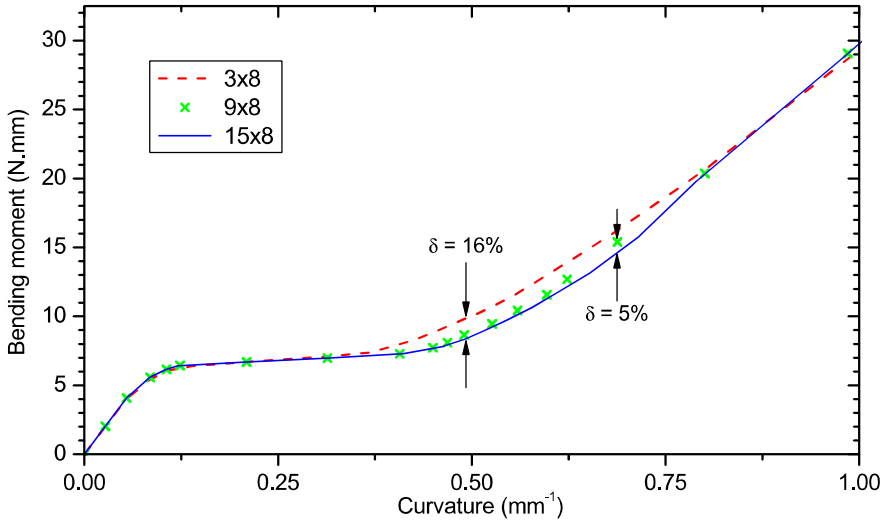

Figure IV.7. Bending moment versus curvature using 3x8 (red dash), 9x8 (green crosses), and 15x8 (blue line) integration points along $\vec{e_r}$ and $\vec{e_\theta}$ respectively.

Table IV.2. Computation (CPU) times of the benchmark depending on the number of integration points used.

Integration	3x8 (17)	9x8 (65)	15x8 (113)
CPU Time (s)	27.3	63.5	101

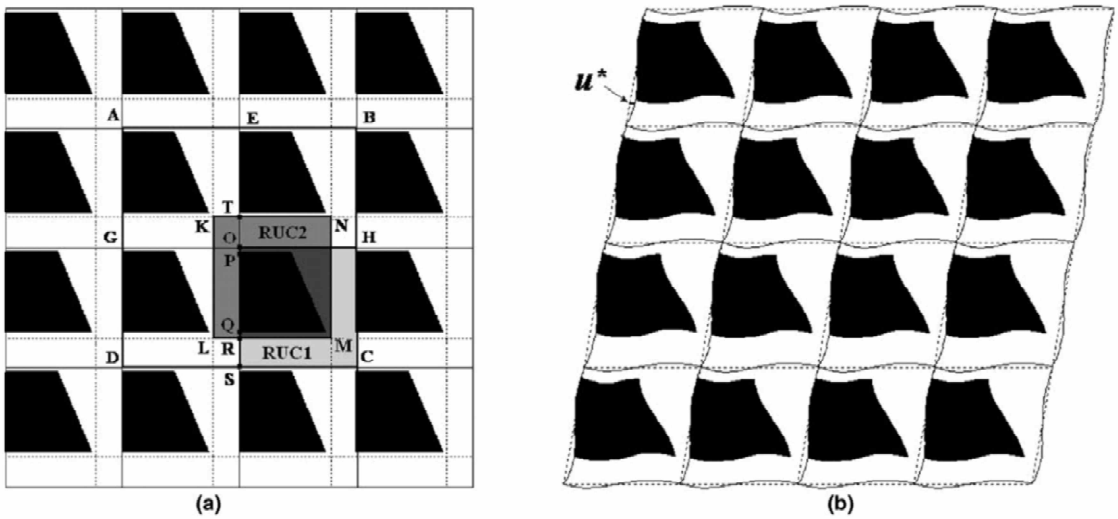

Figure IV.8. Repetition of a 2D periodic pattern in initial state (a), and in any deformed state (b) [9]

2.4 Periodic boundary conditions

2.4.1 3D continuum

For 3D continuum, the kinematic unknowns are the displacements noted, noted u, v, and w along $\vec{x}$, $\vec{y}$, and $\vec{z}$ axis respectively. In this case, the homogenization method consists in constraining displacements between point pairs on opposite faces. With this expression, surface may deform under the effect of loads; the adjacent patterns concordance is kept (Figure IV.8).

Let a cube ABCDEFGH be defined with its edges aligned with $\vec{x}$, $\vec{y}$, and $\vec{z}$ space axis re-

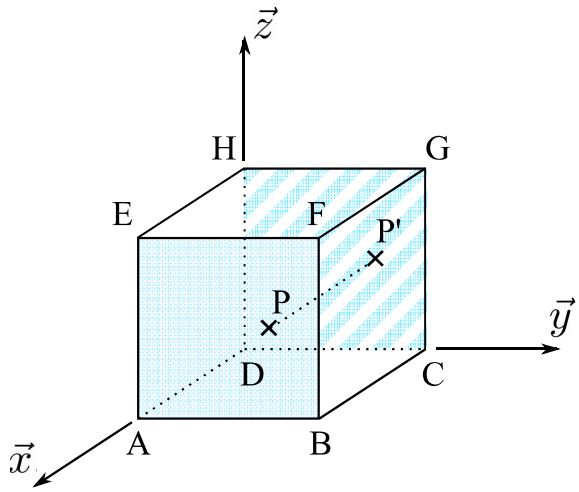

Figure IV.9. Representation of a cubic volume and corresponding points pair for periodic boundary conditions

spectively (Figure IV.9). *P* is a point belonging to the face ABFE (plain color), and its pair *P'* belonging to the surface CDHG (hatching colored), so that $\vec{PP'} = \left\|\vec{PP'}\right\| \vec{x}$. The displacement vectors of *P* and *P'* are written as $< u_P; v_P; w_P >$ and $< u_{P'}; v_{P'}; w_{P'} >$ respectively. The periodic boundary condition between *P* and *P'* is written:

$$\begin{aligned} C_{ux}(t) &= \frac{u_P(t) - u_{P'}(t)}{\left\|\vec{PP'}(t)\right\|} \\ C_{vx}(t) &= \frac{v_P(t) - v_{P'}(t)}{\left\|\vec{PP'}(t)\right\|} \\ C_{wx}(t) &= \frac{w_P(t) - w_{P'}(t)}{\left\|\vec{PP'}(t)\right\|} \end{aligned} \tag{IV.4}$$

$C_{ux}(t)$, $C_{vx}(t)$, and $C_{wx}(t)$ are constant over pairs (PP') at each deformed state. The same equation array is written for point pairs of faces BCGF and ADHE, and point pairs of faces ABCD and EFGH, with new sets of constants $C_{uy}(t)$, $C_{vy}(t)$, $C_{wy}(t)$ and $C_{uz}(t)$, $C_{vz}(t)$, $C_{wz}(t)$ respectively. Those quantities describe strain gradients along the *RVE* principal directions and ensure the deformed pattern periodicity.

2.4.2 Application to knit loop model

For beam elements, nodal kinematic unknowns are displacements ($\vec{u}$, $\vec{v}$, $\vec{w}$) and rotations (R_x, R_y, R_z). Periodic boundary conditions can be formulated using the general definition introduced in Section 2.4.1 for the knit loop model and beam elements.

With such geometry, 3 pairs of periodic boundary nodes are present (Figure IV.10):

- Pair $(M'_1 - M'_3)$ for vertical edges;
- Pairs $(M_4 - M'_4)$ and $(M_5 - M'_5)$ for horizontal edges;

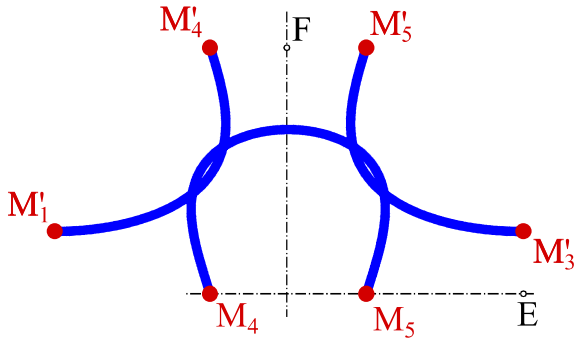

Figure IV.10. Knit loop model presenting boundary points and master nodes E and F.

A set of 15 periodic boundary conditions equations are thus obtained to constrain nodal displacements and rotations for each pair as: Nodal displacements:

$$\begin{aligned} C_{ux}(t) &= \frac{u(M_3')(t) - u(M_1')(t)}{\left\| \vec{M_3'M_1'}(t) \right\|} \\ C_{vx}(t) &= \frac{v(M_3')(t) - v(M_1')(t)}{\left\| \vec{M_3'M_1'}(t) \right\|} \\ C_{wx}(t) &= \frac{w(M_3')(t) - w(M_1')(t)}{\left\| \vec{M_3'M_1'}(t) \right\|} \end{aligned} \tag{IV.5}$$

$$\begin{aligned} C_{uy}(t) &= \frac{u(M_4')(t) - u(M_4)(t)}{\left\| \vec{M_4'M_4}(t) \right\|} = \frac{u(M_5')(t) - u(M_5)(t)}{\left\| \vec{M_5'M_5}(t) \right\|} \\ C_{vy}(t) &= \frac{v(M_4')(t) - v(M_4)(t)}{\left\| \vec{M_4'M_4}(t) \right\|} = \frac{v(M_5')(t) - v(M_5)(t)}{\left\| \vec{M_5'M_5}(t) \right\|} \\ C_{wy}(t) &= \frac{w(M_4')(t) - w(M_4)(t)}{\left\| \vec{M_4'M_4}(t) \right\|} = \frac{w(M_5')(t) - w(M_5)(t)}{\left\| \vec{M_5'M_5}(t) \right\|} \end{aligned} \tag{IV.6}$$

Nodal rotations:

$$\begin{aligned} R_x(M_3') - R_x(M_1') &= 0 \\ R_y(M_3') - R_y(M_1') &= 0 \\ R_z(M_3') - R_z(M_1') &= 0 \end{aligned} \tag{IV.7}$$

$$\begin{aligned} R_x(M_4') - R_x(M_4) &= 0 \\ R_y(M_4') - R_y(M_4) &= 0 \\ R_z(M_4') - R_z(M_4) &= 0 \end{aligned} \tag{IV.8}$$

$$\begin{aligned} R_x(M_5') - R_x(M_5) &= 0 \\ R_y(M_5') - R_y(M_5) &= 0 \\ R_z(M_5') - R_z(M_5) &= 0 \end{aligned} \tag{IV.9}$$

The strain field is applied to the knit loop by controlling the periodic gradients constants C_{ux} to C_{wy} (Eqs IV.5 to **??**) ("master nodes" method [95] [1]). The stitch loop kinematic boundary conditions are applied as nodal displacements or forces on the master nodes *E* and *F*. The relation between master nodes displacements and periodic gradients constants are as follows:

$$\begin{aligned} C_{ux} &= \frac{u(E)}{L} \\ C_{vx} &= \frac{v(E)}{L} \\ C_{wx} &= \frac{w(E)}{L} \end{aligned} \tag{IV.10}$$

and

$$\begin{aligned} C_{uy} &= \frac{u(F)}{d_y} \\ C_{vy} &= \frac{v(F)}{d_y} \\ C_{wy} &= \frac{w(F)}{d_y} \end{aligned} \tag{IV.11}$$

Hence, nodal displacements of master nodes *E* and *F* are introduced into Eqs. IV.5 and Eqs. IV.6 and **??** respectively. Eqs. IV.6 and **??** are also combined to obtain periodic boundary conditions equations as:

$$\begin{aligned} u(M_3') - u(M_1') &= u(E) \\ v(M_3') - v(M_1') &= v(E) \\ w(M_3') - w(M_1') &= w(E) \end{aligned} \tag{IV.12}$$

$$\begin{aligned} u(M_4') - u(M_4) = u(M_5') - u(M_5) &= u(F) \\ v(M_4') - v(M_4) = v(M_5') - v(M_5) &= v(F) \\ w(M_4') - w(M_4) = w(M_5') - w(M_5) &= w(F) \end{aligned} \tag{IV.13}$$

2.5 Contact management and resolution method

The contact are modeled with a "distant contact" condition between slave nodes and master geometry [2]. Such "distant contact" condition may become difficult to implement when the section of both slave and master geometries are not circular as this requires to know the current configuration of the section and its orientation in the global coordinates system for each slave and master geometry. Hence, several simplifications have been introduced in the finite elements code to compute such "distant contact" condition between beam elements. These hypotheses depend on the chosen resolution method: i) implicit or ii) explicit.

[1] Two master nodes, namely E and F, are used to constrain constants C_{ux}, C_{vx} and C_{wx}, and C_{uy}, C_{vy} and C_{wy}, respectively.

[2] As opposed to 3-dimensional case where the contact occurs when the distance between slave nodes and master geometry is zero

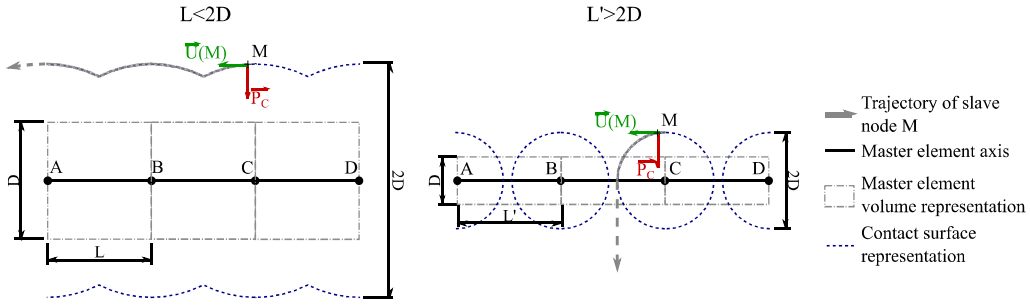

Figure IV.11. Illustration of the contact management between a node and a beam element in Abaqus using implicit resolution method.

2.5.1 Implicit resolution method

The contact between a node and a beam finite element is represented in figure IV.11. The master surface is defined by beam finite elements of length L between nodes A, B, C and D. Those elements possess a circular section of diameter D. Let consider a node M, moving along the master surface in direction of the element AB axis with a direction vector noted $\vec{U}(M)$. A contact pressure noted $\vec{P_C}$ is applied on the element at point M. Using the implicit resolution method in Abaqus, the contact is performed by creating "contact spheres" of diameter equal to $2 \times D$ around the master surface nodes. The contact condition is defined by restraining slave nodes from moving inside such spheres. Two cases are depicted in figure IV.11. The first case represents a master surface where elements length L is less than elements diameter $2 \times D$. The second case represents a master surface where elements length L is greater than $2 \times D$.

In the first case, contact spheres around nodes A and B intersect and form a continued contact surface. Slave node M may therefore slide along this surface, describing a set of arcs with rough points at each intersection of spheres outer surface.

In the second case, however, contact spheres around nodes A and B do not intersect, and the obtained contact surface is discontinued. Hence, the node M may slide on the spherical surface around node B, in this case, and then move through the entire element AB due to the vertical force P_C.

This method may be therefore used in very specific cases, where elements used in the model are thick beams with $2D > L$, or when no movement is intended between master elements and slave nodes. A special care should be taken to align both master and slave nodes in the initial configuration to ensure a correct contact distance.

2.5.2 Explicit resolution method

When using an explicit resolution formulation, the contact between beam elements is constrained similarly to contact between solid elements. The distance a between the slave node M and each master surface elements is computed at every increment start. This distance is compared to the sum of both master and slave surfaces section radii. A common contact penalty method is then used to solve contact restrictions. Therefore, the contact surface obtained along the beam element axis is continued and represents the actual element volume.

Yet few restrictions are present, such as the circular shape of the contact surface, equal to the smallest outbound circle around the section in the case of non-circular sections. The contact sur-

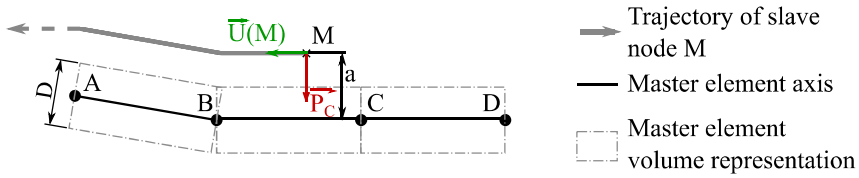

Figure IV.12. Illustration of contact management between beam finite elements using explicit resolution method.

face is also computed in straight line between master nodes, reducing the effective representation of the element volume in the case of highly deformed quadratic beam elements for example.

In knitted textiles, high slip distances are traveled during tensile tests. Hence, due to the implicit resolution contact management restrictions, explicit resolution method is used.

2.5.3 Mass scaling and kinetic energy

The contact between beam elements requires the use of explicit resolution method for the knit loop model. Such resolution method is conditionally stable, and the stability is dependent to time increment. The critical time increment is generally small, and computational times may increase drastically. Furthermore, the explicit resolution method takes into account dynamic effects in the form of kinetic energy, while experiments are conducted at low strain rates for quasi-static deformations.

As the stable time increment depends on the mesh size and material density, to increase the stable time increment artificially, the “mass-scaling” process is used. This process increases the material density by a specific factor, or to reach a certain time increment, both user-defined, if density is not a relevant parameter in the analysis.

However, as mass-scaling increases material density, kinetic energy is increased as well. High kinetic energy induces oscillations in nodal displacements, and may distort the analysis results. Therefore, mass-scaling factor or target time increment have to be chosen carefully to not induce a large amount of kinetic energy in the model.

To help reduce the amount of kinetic energy stored in the model during loading, material damping has been introduced, and the influence of its intensity studied in simple bending with beam elements. A simple model has been created in order to define the optimal damping coefficient. The geometry used is the same model as presented in Section 2.3.2. The beam free end is constrained in displacement, with a maximum displacement $u_y = -14mm$. This value has been chosen to induce large nodal displacement and strain energy to increase the damping coefficient impact visibility. The material used is linear elastic material to keep a conservative model, apart from the material damping studied. A Rayleyh type material damping has been chosen for simplicity reasons. Five damping coefficient values have been tested. The impact of the coefficient α on the model kinetic energy and reaction force during bending is shown in Figure IV.13. The reference analysis is calculated with the implicit method (dots), while the study of damping influence is performed in explicit resolution (lines).

When no material damping is introduced, kinetic energy shows the oscillations mentioned previously, leading to similar oscillations in the reaction force at the beam free end. With the increase of damping coefficient α, kinetic energy decreases earlier during loading. Peak values also decreases, resulting in lower to negligible oscillations on the reaction force for $\alpha \geq 50$. However,

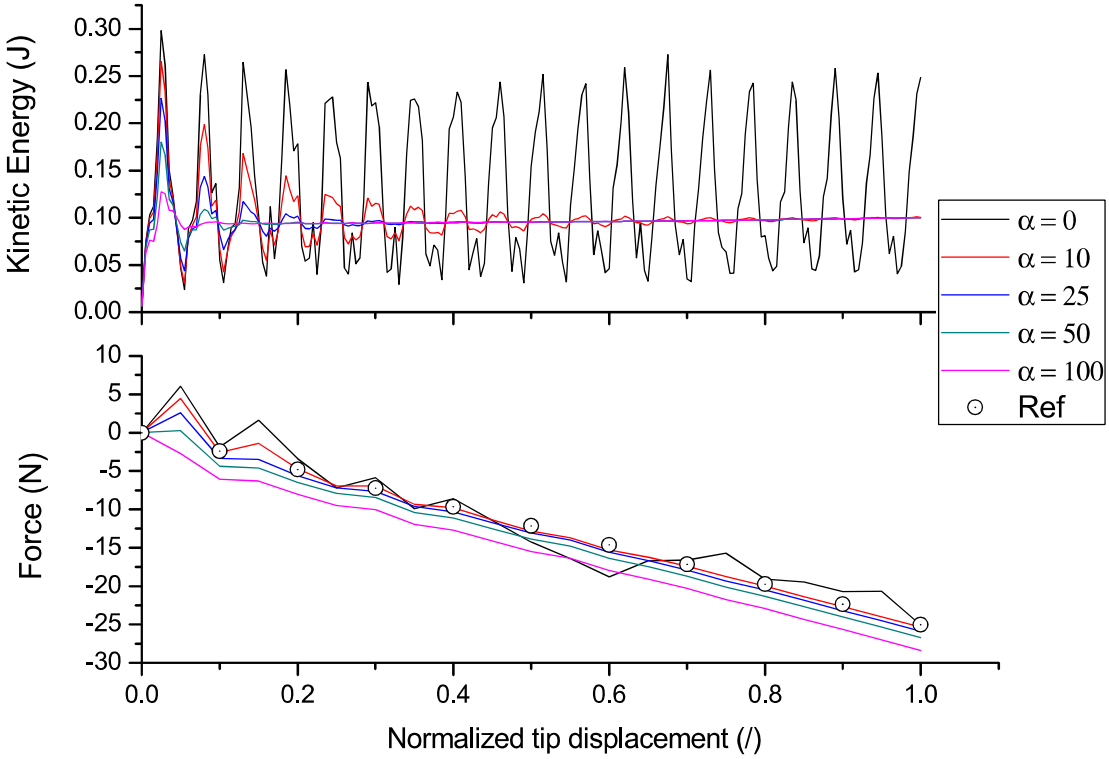

Figure IV.13. Kinetic energy (top) and reaction force at the beam free end (bottom) for different values of material damping.

the increase in damping coefficient causes an increase in reaction force due to the absorption of internal strain energy. For a parameter $\alpha = 100$, the estimated reaction force is 10% higher than the reference value. A value of $\alpha = 50$ returns an error in the reaction force estimation of 6.7%, which is considered satisfactory. Such value has been used for the numerical analysis of the knit loop.

2.6 Conclusion

In this chapter, the periodic boundary conditions and beam elements have been presented and applied to create the knit loop unit cell model. The geometrical model has been derived from the knit loop dimensions and models the contact between two knit rows. The general equations defined for periodic boundary conditions on a cube have been translated to the stitch model and allow simplified boundary conditions with only few constraints. A set of 9 equations has been introduced in addition to the general equations to ensure the beam mean fiber tangent continuity between consecutive patterns in the deformed state. The method led to a total of 18 equations to fully constrain the stitch periodicity and continuity. The master nodes technique has been used with those equations to enforce the knit loop strains in the $(\vec{x}, \vec{y})$ plane.

The explicit resolution method is used to allow beam contact and sliding management. Because of the explicit resolution, kinetic effects and long computational times are yet involved. The mass scaling technique is therefore used to increase the stable time increment to a target time increment giving reasonable calculation times while minimizing dynamic effects. Furthermore, to reduce undesired dynamic effects, Rayleigh material damping has been introduced and vali-

dated in simple bending on beam elements. A typical value of 50 for the damping coefficient has been found to lead to low to negligible dynamic effects while limiting the bending reaction force overestimation.

Lastly, the influence of the number of integration points on the beam section has been studied in terms of bending moment to curvature relation in simple bending for a superelastic material behavior. It has been shown that default integration (3x8 points) lead to an overestimation of the bending moment up to 16%. The number of integration points has hence been increased, and the increase in precision over computation time balanced. The final number has been chosen equal to 9 points radially and 8 circumferentially.

The model will then be validated in regards to experimental results in the following chapter on knitted NiTi textiles.

CHAPTER

V Knitted NiTi textile characterization

1 Introduction

The goal of this chapter is to apply the methodology developed in this work to characterize the various deformation mechanisms taking place in the knitted NiTi textile and their influence on the textile mechanical behavior during tensile loading. The experimental analysis and numerical tools (Chapters III and IV) are applied to the knitted NiTi textile sample in uniaxial and biaxial tension.

The textile mechanical behavior depends on several parameters, such as knit loop geometry, wire characteristics, friction coefficient, *etc*. To analyze those parameters, the knit loops dimensions distributions and populations are first studied in order to characterize the textile geometrical uniformity. The wire material parameters are computed from a simple tensile test and the friction coefficient between NiTi wires is estimated. These parameters are introduced in the numerical model in order to study the influence of material constants and friction coefficient on the knit loop mechanical behavior.

In a first time, studied samples are presented (Section 2). Experimental results obtained on such samples are then presented (Section 3). The corresponding finite element model results are introduced and validated in regard to the experimental results (Section 4). A conclusion is finally made on the knitted NiTi textiles mechanical behavior (Section 5).

2 Samples

Knitted textiles used to run experiments are presented here. The wire properties, the heat treatment performed to shape-set the textile, and the wire tensile behavior are first introduced. It has been tested with the experimental setup (Chapter III, Section 4) adapted to knitted textiles. Then, the knit loop pattern at the initial state is studied in terms of value, population, and spatial repartition, with the in-house software (Chapter III, Section 2.2). The knit loop mean representative geometry is computed from those measurements.

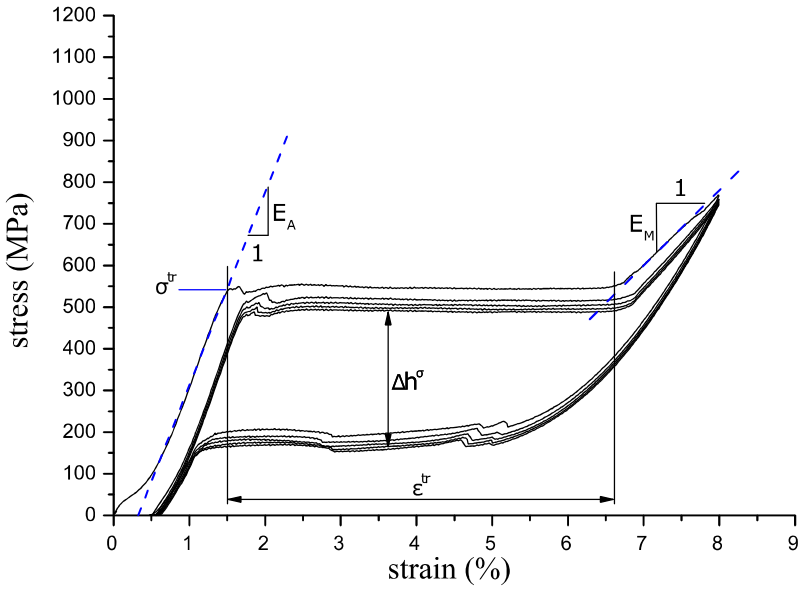

Figure V.1. Simple tensile test of a NiTi wire, composition of 50.8 at% Ni and ∅0.1 mm diameter (Fort Wayne Metals, NiTi#1)

2.1 Wire composition and behavior

The wire used for the knitting process is composed of 50.8 at% Ni (Fort Wayne Metals, NiTi#1), possesses a diameter of ∅0.1 mm, and is provided in the "cold-work" state. In such state, the wire has a common elasto-plastic behavior with a high yield stress, of the order of 1.5 GPa.

A flat bed bench knitting machine is used to manufacture the fabric. After the knitting process, the wire does not possess the superelastic behavior and residual stresses remain within the wire due to the knitting. The shape-setting stage is performed using a simple setup to hold the textile and to obtain more even loop shape. The system is then put in a furnace at 450^{o}C for 30 minutes to reduce internal stresses and to heat-treat the wire to the superelastic behavior. The wire is tested in simple tension after treatment, and the resulting mechanical behavior is presented in Figure V.1.

The experimental biaxial testing setup presented in Chapter III (Section4) and tested on soft silicone membranes has then been adapted to fit knitted textiles. Springs hook-like extremities are used to grab the textile directly within each loop, taking advantage of the fabric porosity (Figure V.2, zoomed insets). However, because of the knit loop geometry and the convexity of segments S1 and S3 (cf Chapter III , Section 2.2.2), springs aligned with the wale direction (y in this case) are not placed symmetrically side to side (Figure V.3). The hooking point stability is not insured if a symmetrical spring disposition was to be chosen. A similar problem occurs with springs aligned along the x-axis as the sinusoidal shape of segments S2 and S4 does not offer a stable hooking point.

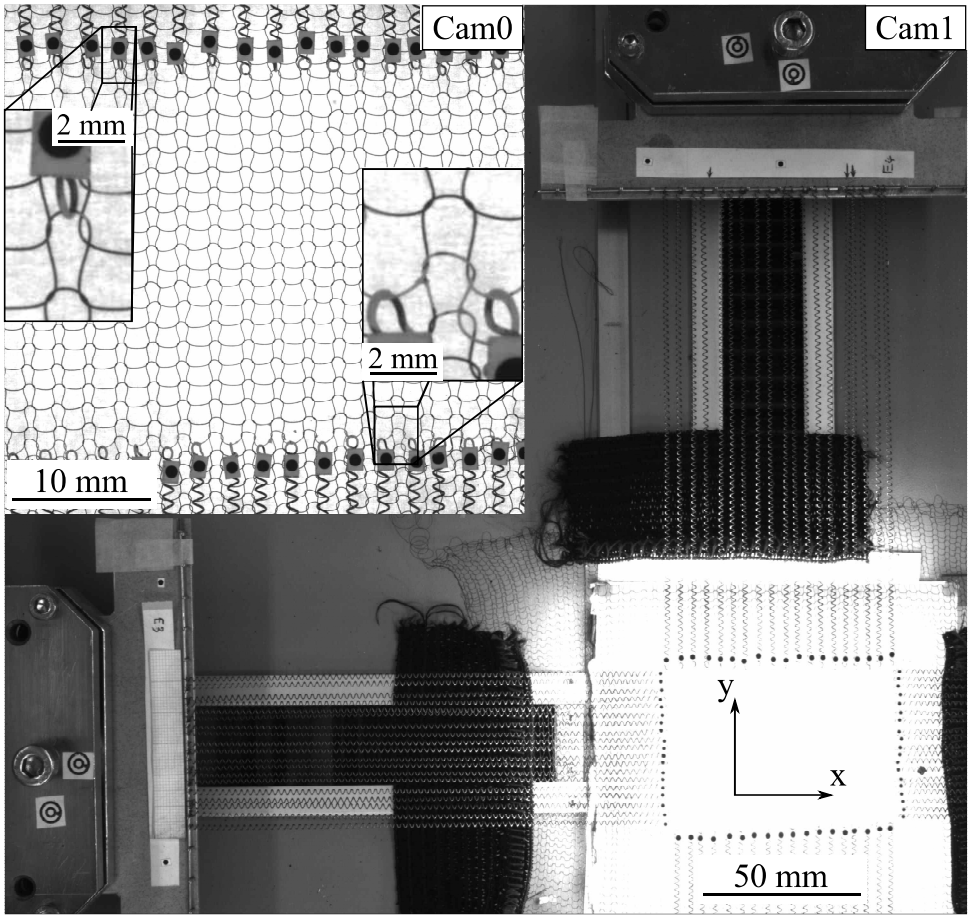

Figure V.2. Knitted NiTi textile set-up in the biaxial tensile test experimental apparatus

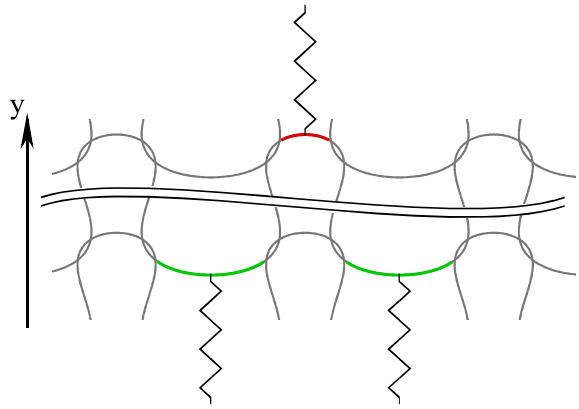

Figure V.3. Springs placement in the wale direction and symmetry defect due to the knit loop wire curvature.

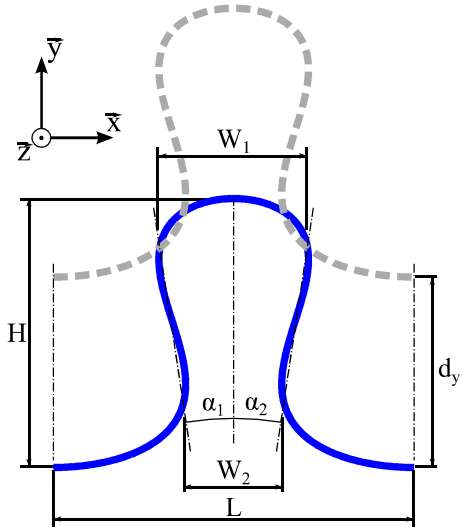

Figure V.4. Knit loop dimensional parameters.

2.2 Knit pattern and representative geometry

The numerical model developed in this work uses a single knit loop chosen to be representative of the textile sample tested. The knit loop geometry obtained after the sample shape-setting (Figure V.4) is studied thanks to the in-house software presented in Chapter III (Section 2.2). Each knit loops dimension spatial distribution is analyzed within the sample zone of interest. This distribution is studied to verify the random characteristic, or to highlight particularity resulting from manufacturing or shape-setting process instabilities. Assuming a Gauss repartition the mean value and standard deviation in absolute value and in percent of the mean value are computed and presented in text box within the histogram plots with letters μ, σ, and $\sigma_{\%}$ respectively.

The knit loop dimensional parameters L, H, and d_y are randomly spread across the sample zone of interest (Figure V.5), indicating no particular defect in the knitting and shape-setting process. The standard deviation for each dimension is equal to 3.4%, 5.4%, and 8.1% respectively. These low values indicate that the representation of the global textile morphology using the mean dimensions values is representative.

The knit loop widths are also randomly distributed in the textile zone of interest, and no direct link can be made between the spatial repartition of both dimensions. These distributions indicate that the knitting process and shape-setting process did not induce particular defects in the loop geometry. The standard deviation obtained for these dimensions are equal to 6.5% and 13.3% respectively. The W_1 standard deviation is satisfactory, while W_2 standard deviation is superior to the maximum deviation considered satisfactory (10%). Hence, the use of the mean value may induce errors in the simulated mechanical behavior, and the influence of such deviation on the textile mechanical behavior should be studied.

The knit loop angular opening $\alpha_1 + \alpha_2$ spatial distribution appears here also randomly distributed across the sample zone of interest (Figure V.7). However, the loop warping angle $\alpha_1 - \alpha_2$ spatial distribution shows a distinctive alternated pattern between positive and negative values in the wale direction (y).The mean value is close to zero (0.89^o) which corresponds to an almost right angle between course and wale direction (89.11^o). Two main populations can be distinguished: a population centered around -2^o and a second around +3^o, equivalent to the mean value

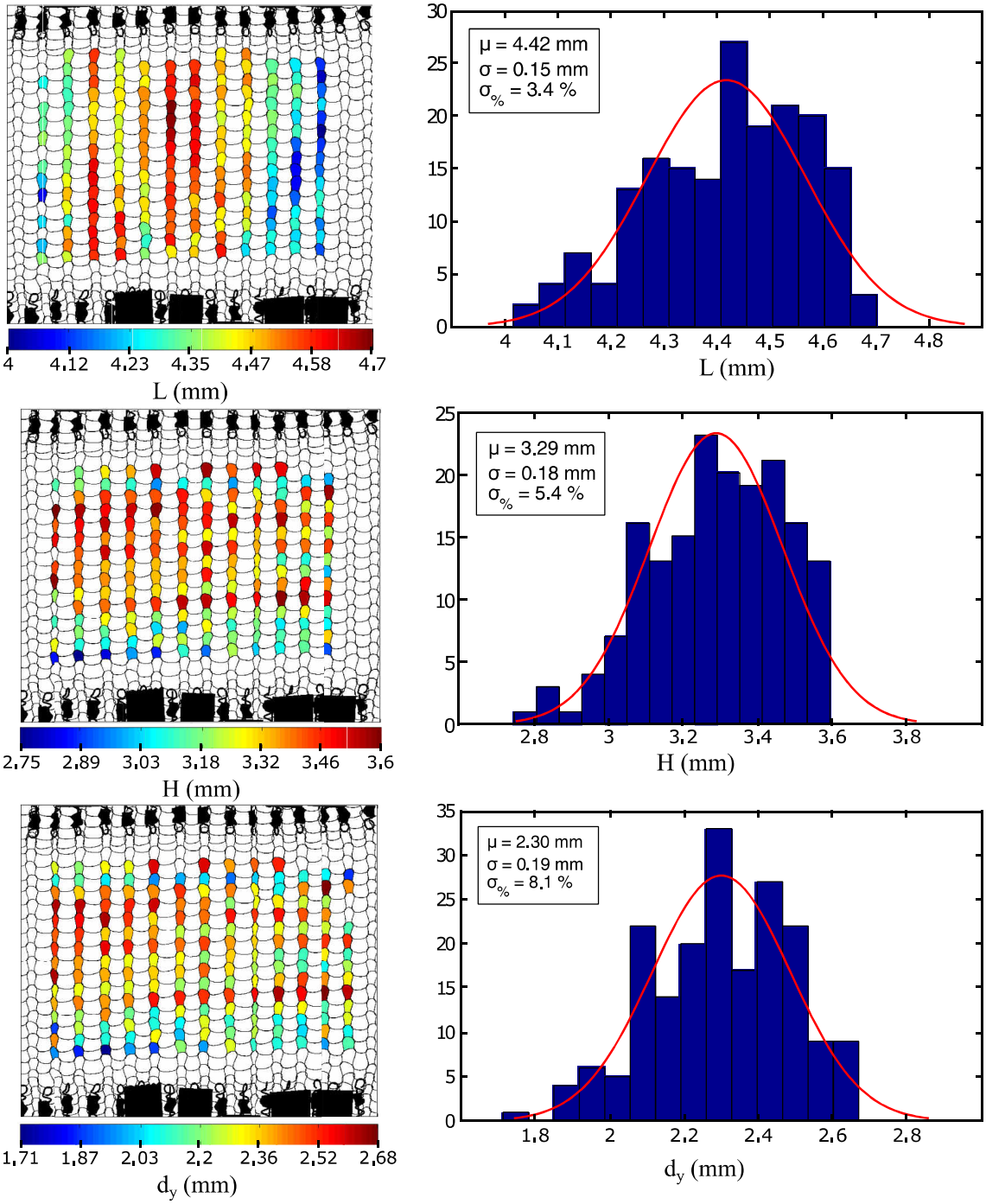

Figure V.5. Distribution maps of knit loop dimensions L, H, and d_y in the initial state (left) and population distributions and gaussian fit with mean value and standard deviation (right)

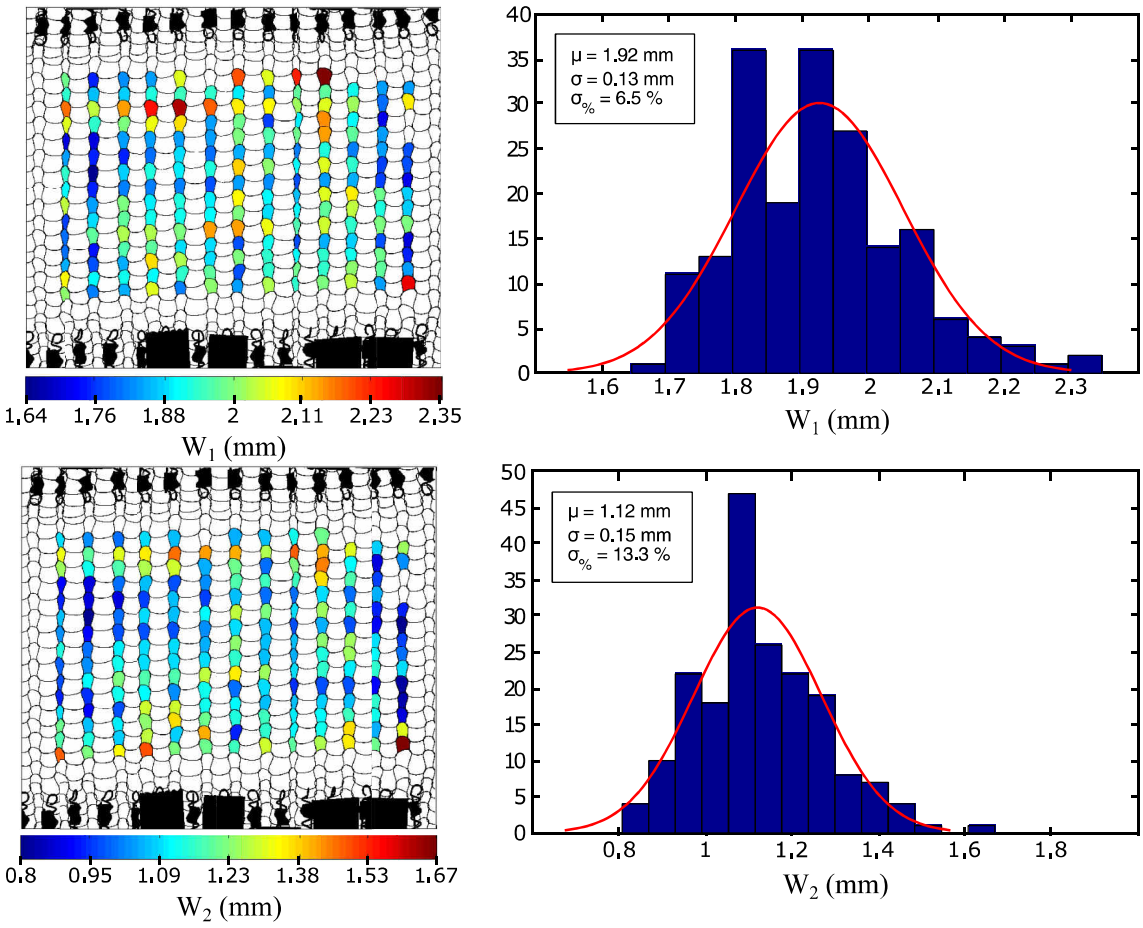

Figure V.6. Distribution maps of knit loop widths W_1 and W_2 in the initial state (left) and population distribution and gaussian fit with mean value and standard deviation (right)

$\pm\sigma$ ($\pm 2.78^o$). The high standard deviations for both angles highlight the difficulty of shaping a wire with a considerable elastic modulus. During knitting process, the local curvatures are very small and induces large axial strains in the wire. The sample being knitted with a cold-work wire ($E_A \approx 60GPa$ and $\sigma_e \approx 1.5GPa$), large residual stresses are present after knitting is complete, and create shape defects. These shape defects are kept after shape-setting, even if residual stresses are removed from the wire. However, the effect of alternating warping is expected to be negligible as it compensates itself to provide a mean value close to zero.

The mean values and standard deviations are recapitulated in table V.1, and the mean representative geometry has been identified with such dimensions and the parametric equations presented in Chapter III, Section 2.2. The resulting knit loop is presented in Figure V.8 (green line) alongside with 8 copies (blue lines) and superimposed over the textile picture in its initial state. This superposition over a zone larger than a single knit loop shows the approximation of a mean representative geometry over the real varying geometry, yet depicts that idealizing the textile as a repetition of perfect loops fits a larger sample area. This figure also highlights that alternating warping does not induce noticeable deviation of the mean representative geometry over 3 knit rows.

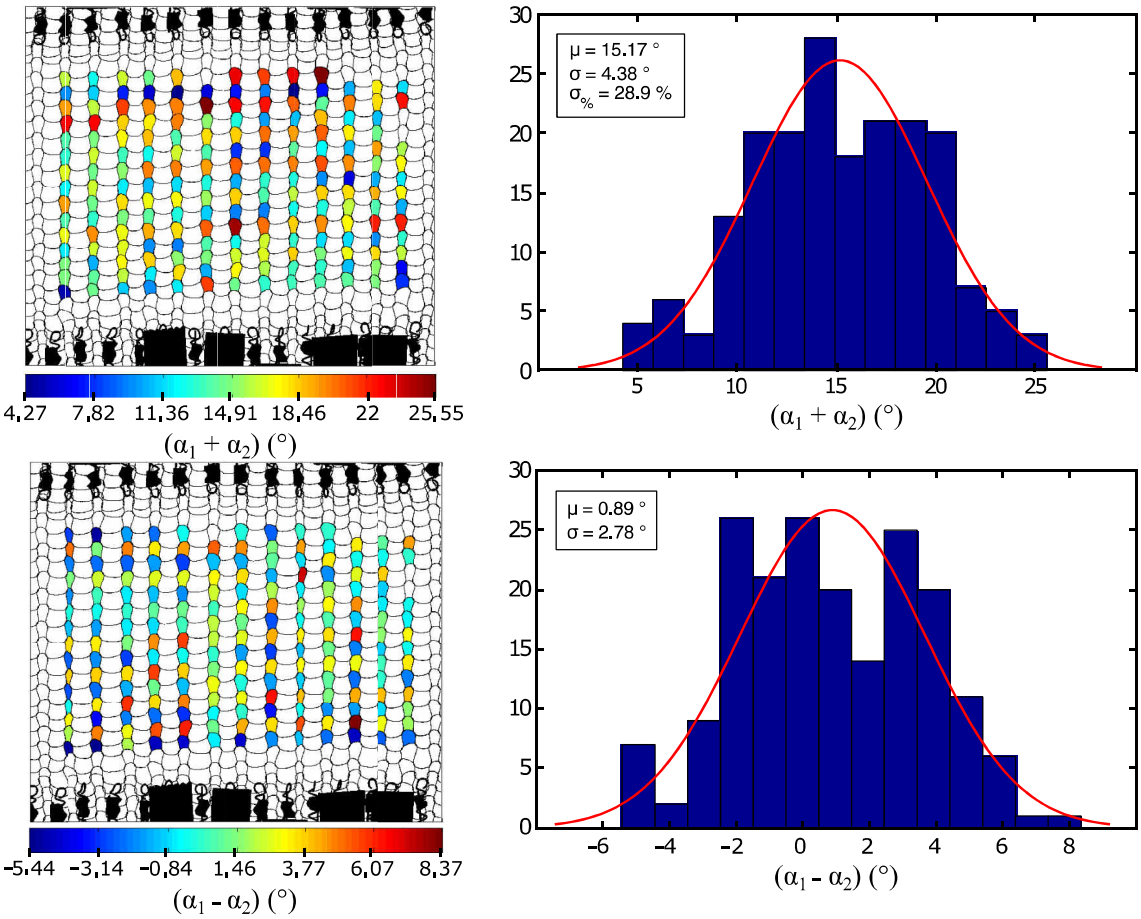

Figure V.7. Distribution maps of knit loop opening $\alpha_1 + \alpha_2$ and warping $\alpha_1 - \alpha_2$ in the initial state (left) and population distribution and gaussian fit with mean value and standard deviation (right)

Table V.1. Experimental initial mean loop dimensions

	$L(mm)$	$H(mm)$	$d_y(mm)$	$W_1(mm)$	$W_2(mm)$
Mean	4.42	3.29	2.30	1.92	1.12
Std dev	0.15	0.18	0.13	0.15	0.19

3 Experimental results

In this section, experimental results obtained on knitted NiTi textile are presented. Firstly, the wire friction coefficient between NiTi #1 wires heat treated at 450^{o}C for 30 minutes is presented and briefly opposed to values found in literature. Then, uniaxial tensile tests on knitted NiTi textiles are presented, starting with the sample macroscopic behavior, followed by knit loop geometry changes during loading, and finally boundary forces distribution measured via the spring system presented in Chapter III. On the same plan are then presented results obtained for the same textile in biaxial tension.

3.1 NiTi wires friction coefficient

Using the principle presented in Chapter III, Section 3, the friction coefficient between NiTi#1 (FWM) wires heat-treated at 450^{o}C during 30 minutes has been experimentally determined.

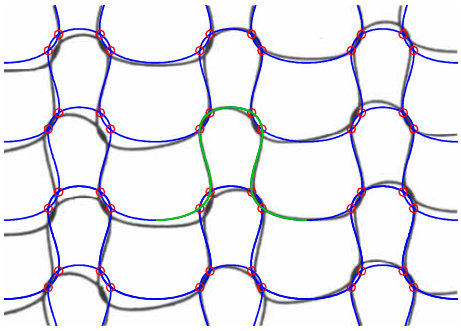

Figure V.8. Initial geometry identified on experimental picture created using parametric equations presented in Chapter 2.2

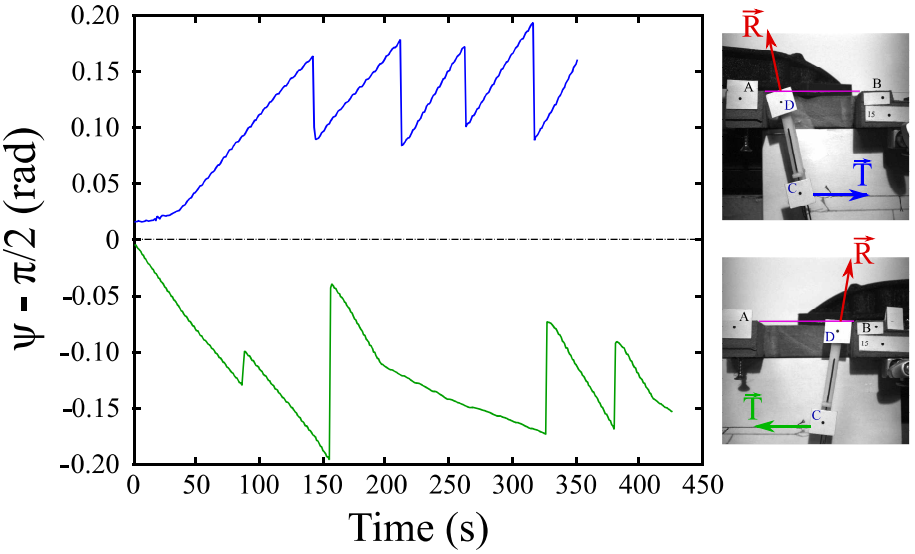

Figure V.9. Total friction cone angle measurement between two nitinol wires plotted versus time

Values obtained during time of the angle $\psi - \frac{\pi}{2}$ are plotted in the two configurations, namely $\vec{T} > \vec{0}$ (blue line) and $\vec{T} < \vec{0}$ (green line) (Figure V.9). A single measurement set is presented over the three performed for clarity purposes. Peak values correspond to instants when the mobile begins sliding along the reference wire, *i.e.* instants when $\vec{R}$ relies on the friction cone edge.

The friction cone half summit angle φ is defined by the peak-to-peak values of curves $\psi - \frac{\pi}{2}$ divided by 2, repeated over the three measurements sets. In this case, a total number of 121 values have been obtained for φ and the corresponding histogram distribution plot is presented Figure V.10. Assuming a Gaussian distribution, a mean value $\varphi_{moy} = 0.186$ rad and a standard deviation $\sigma = 0.016$ rad have been obtained. The friction coefficient is therefore found equal to $f = 0.185 \pm 0.02$. In literature, few values are found, and range from 0.13 to 0.51. The coefficient measured with this method is relatively close to the coefficient 0.13 obtained by Abel *et al.* [50], identified using a reverse analysis method, taking an analytical model and experimental results in uniaxial tension on knitted NiTi textiles made of ∅ 0.2 mm wire.

3.2 Uniaxial tension

This section regroups experimental results obtained for the knitted NiTi textile in uniaxial tension.

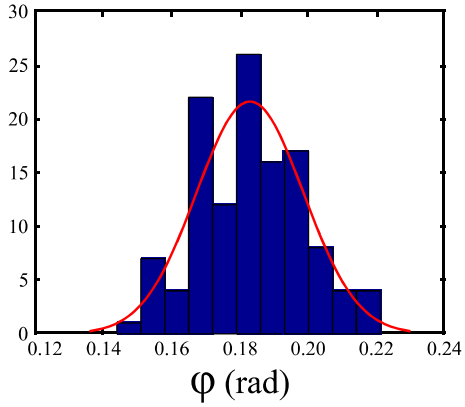

Figure V.10. Demi-friction cone angle obtained with a set of three measurements, mean value $\phi_m = 0.186\ rad$ and a standard deviation $\sigma = 0.016\ rad$

An initial pretension $F_0 = 0.02\ N.mm^{-1}$ is applied in both course and wale directions before conducting tests in order to remove the textile looseness. This force is maintained constant during uniaxial tension in the transverse direction. The working area targeted strains are measured via camera extensometers placed on springs target, one extensometer in each direction. The maximum strain is equal to 30%, and the strain rate equal to 0.0025 s^{-1}.

3.2.1 Stress-strain relations

The sample macroscopic behavior measured with the spring system (F^E_{lin} and ϵ^W, Chapter III, Section 4) is presented Figure V.11. The upper part presents the mechanical response in lineic force versus axial strain for course (blue line) and wale (red dash) directions. The bottom part presents the transverse strain versus axial strain. Four specific step times A, B, C, and D, have been included and are referenced in further figures as specific strain states.

The experimental results highlight the mechanical properties and particularities of the knitted textile tested. The textile anisotropy appears clearly in this figure, depicting the course direction (blue line) stiffer than wale direction (red curve). At 24% strain, the lineic force in the wale direction is 30% lower than in the course direction.

At strain state A, in the course direction, the strain is equal to 6%, and the hysteresis in lineic force is equal to $H_C(A) = 3.5\ 10^{-2}\ N.mm^{-1}$, and at strain state C (sample strain equal to 18%), the lineic force hysteresis is equal to $H_C(C) = 4.6\ 10^{-2} N.mm^{-1}$. The increase ratio between this minimum and maximum values is equal to 1.316. In another hand, in the wale direction, at 6% sample strain, the lineic force hysteresis $H_W(A) = 2\ 10^{-2}\ N.mm^{-1}$, almost two times lower than its course-wise counterpart. However, at 18% sample strain, the hysteresis is equal to $H_W(C) = 3.9\ 10^{-2}\ N.mm^{-1}$, hence an increase ratio of 1.9. Finally, at final stage of loading (30% strain), the maximum hysteresis value is reached and is equal to $H_W(D) = 4.9\ 10^{-2}\ N.mm^{-1}$, being 2.5 times greater than $H_W(A)$. The course direction also shows a greater "stiffening" of its force response. Finally, no residual strain appears in each direction after charges are released.

The curves presenting the transverse strain versus axial strain also highlight the textile anisotropy in an opposite way, in the sense that, in the course direction, the textile is more compliant inducing an higher transverse strain. The Poisson's coefficient in the course direction is

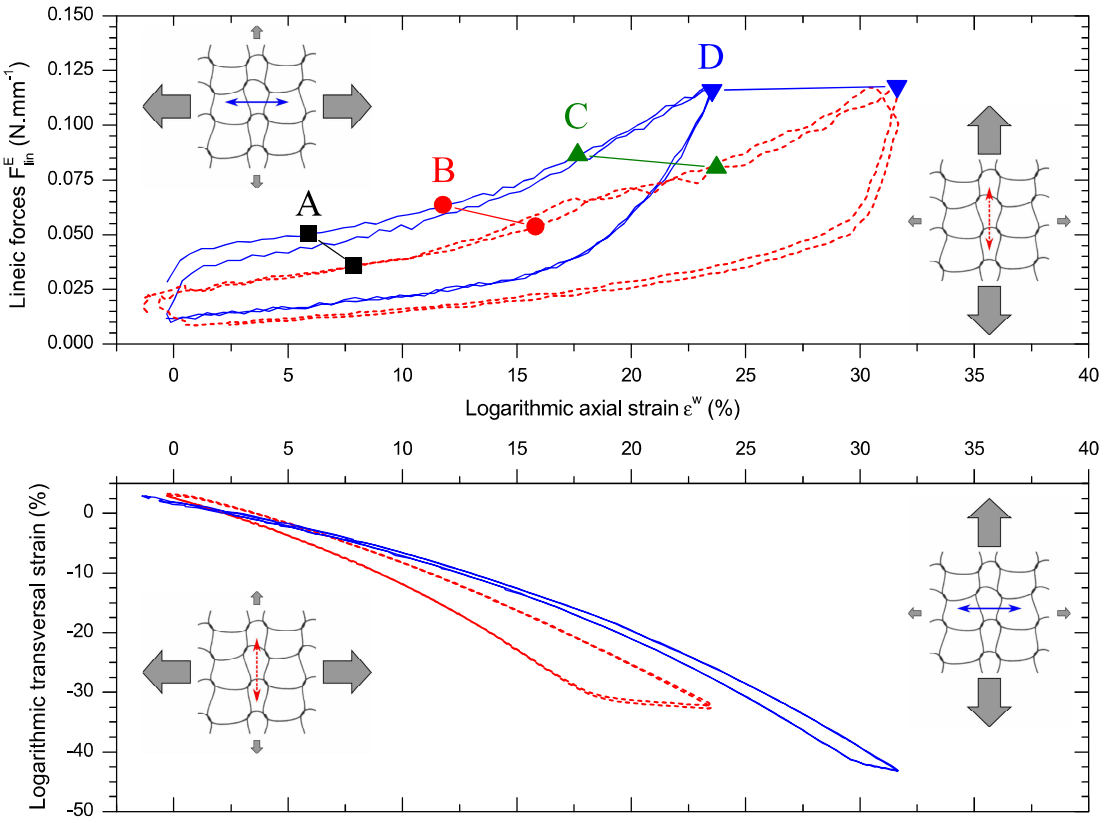

Figure V.11. Mechanical behavior of knitted NiTi textile in uniaxial tension; lineic force - axial strain relations (top), and transversal strain - axial strain (bottom)

thus higher than in the wale direction, and estimated at $\nu_{xy} = 1.05$ while in the wale direction, the Poisson's coefficient is estimated at $\nu_{xy} = 0.94$. This strains anisotropy may prove useful in specific applications, such as tubular actuator, for example, with the wale direction parallel to the tube axis and course direction to the circumferential axis. Inflating the tube leads to an axial stroke, and the anisotropy allows higher axial strains for lower tube inflation, reducing volume needed for the actuator to inflate.

3.2.2 Representative loop geometry under loading

The knit loop mean representative geometry has been determined at the textile initial state. This geometry has been shown to represent the global textile morphology with low deviation except for the knit loop width W_2 and opening and warping angles. During loading, initial geometrical uniformity defects and strain field uniformity defects may degrade this mean geometry representative capacity. These defects may therefore reduce the precision of the numerical model. The evolution of the mean representative loop dimensions is therefore studied during loading, as well as the standard deviation associated, in order to assess for loop geometry uniformity variations. In the following figures, the mean value is represented in thick lines, and standard deviation by the colored area centered around the mean value, plotted at $\pm\sigma$.

The wale-wise tensile test is first studied (Figure V.12). The knit loop length L presents an opposite variation compared to the vertical distance between rows d_y. These variations correspond

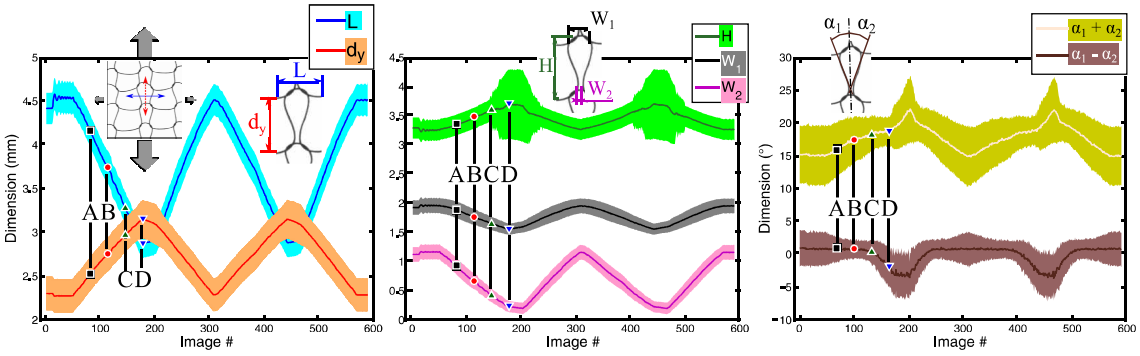

Figure V.12. Loop dimensions variations during loading cycles in wale-wise tension

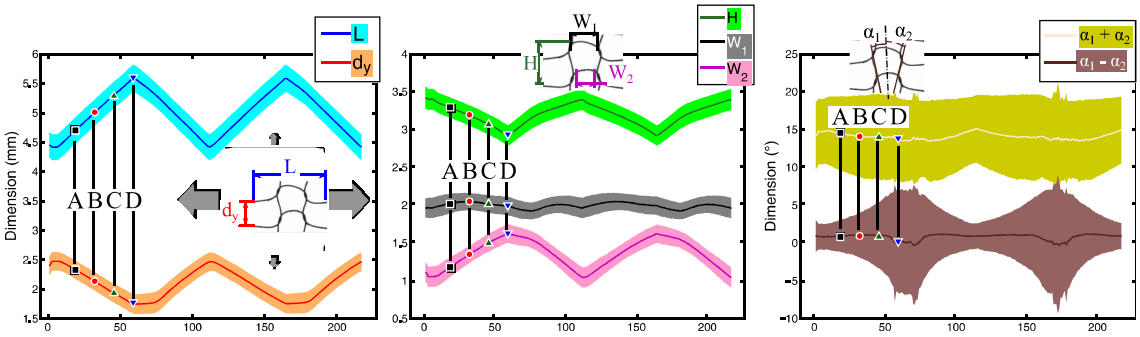

Figure V.13. Loop dimensions variations during loading cycles in course-wise tension

to the sample global strains. The standard deviation of each dimension retains its initial absolute value, implying that no uniformization of loop dimensions occurs with the increasing loading.

The knit loop height H also increases yet of a smaller quantity than d_y. The standard deviation retains its initial value until step C, where the transverse contraction of the textile implies contact between segments S2 and S4, preventing the detection of segment S1 and intersection points correctly (Figure V.14). This error is also reproduced during the second loading, in same intensity and time span, inducing that the error is phenomenological and not consequent to the method. Mean values and standard deviations of the loop widths W_1 and W_2 decrease with loading. The almost zero value of W_2 indicates the contact between segments S2 and S4, and such measure may be taken with caution as well because of errors in intersection points placement described.

Finally, the mean warping value $\alpha_1 - \alpha_2$ shifts from zero value, while the standard deviation decreases. The springs symmetry defects on each side on the wale direction and hooking points instability in both wale and course direction may induce small shear strains in the sample working area and modify the warping mean value. The loop angular opening $\alpha_1 + \alpha_2$ follow a stable increase while the standard deviation decreases. Loading in wale direction tends to standardize the angular opening.

The tensile test in course direction is then studied (Figure V.13). The knit loop length L and the knit rows distance d_y vary in an opposite way, corresponding to the sample strains, similarly to the tensile test in wale direction. The standard deviation of both dimension remains constant throughout loading cycles.

As previously, the knit loop height H decreases alike knit rows distance d_y with a lower intensity, and the standard deviation remains constant. For this loading case, knit loop remains well defined, and the in-house software is able to detect correctly intersection points and loop

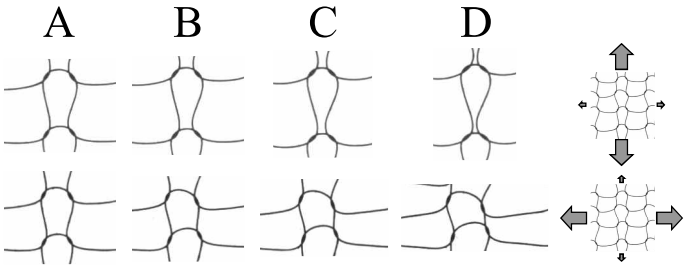

Figure V.14. Deformation of a random knit loop during wale-wise tensile loading (top) and course-wise tensile loading (bottom)

segments, removing the increase in the standard deviation seen in the previous test. The knit loop smaller width W_2 increases largely as compared to the larger width W_1, up to close values. Knit loops tend to change to a rectangular shape, without change in standard deviations of both dimensions. There is no standardization of knit loop dimensions with this type of loading.

Finally, shape parameters are analyzed. The angular opening $\alpha_1+\alpha_2$ decreases slightly despite the rectangular shape depicted previously. The standard deviation increases by 40% (from $\pm 5^o$ to $\pm 7^o$) implying that the deformed knit loops initial defects are amplified by the loading case. Such deduction can be performed on the loop warping $\alpha_1 - \alpha_2$ which mean value remains close or equal to zero, yet the standard deviation greatly increases from $\pm 2.5^o$ to $\pm 7.5^o$.

The deformed shape of a loop chosen randomly in the sample central area is presented in Figure V.14 for both wale-wise and course-wise uniaxial tension. In the former load case, the knit loop horizontal symmetry is preserved as the loading is also of the same symmetry and therefore, initial defects in the loop warping and opening are preserved. Horizontal segments $[M_1, I_1]$ and $[I_8, M_3]$ remain horizontal, and initial warping does not interfere and the deformation mechanism is thus stable. On the contrary, for the second load case, initial warping defects, which can be linked to alignment defects of segments $[M_1, I_1]$ and $[I_8, M_3]$, tend to destabilize deformation mechanisms, and such defects are amplified with the increased loading, as seen previously. The initial knit loops dimensions uniformity is thus key to stable deformation mechanisms.

Knit loops length L and knit rows spacing d_y illustrate the knit loop encompassing box strains. Logarithmic strains of each loop are thus computed using such dimensions as:

$$\begin{aligned} \epsilon_{xx} &= ln(\frac{L}{L^0}) \\ \epsilon_{yy} &= ln(\frac{d_y}{d_y^0}) \end{aligned} \tag{V.1}$$

The evolution of the loops strains mean value (thick lines) and standard deviation (colored surface) are plotted versus time and compared to the sample strains in the same direction (symbols) (Figure V.15). The stitch strains mean value correspond to the global sample strains, in both course-wise and wale-wise uniaxial tension, allow correlation between the mean representative knit loop strains and the sample strains, thus allowing the study of such loop numerically. Furthermore, stitch strains spread in the course direction (blue lines/surfaces) is narrow ($\pm 2\%$ to $\pm 4\%$ at maximum sample strains), indicating more uniform strains in that particular direction and better approximation of the sample strain with the homogenization method. In the wale direction, the standard deviation in strains ranges from $\pm 5\%$ to $\pm 7\%$ at maximum sample strains. The homog-

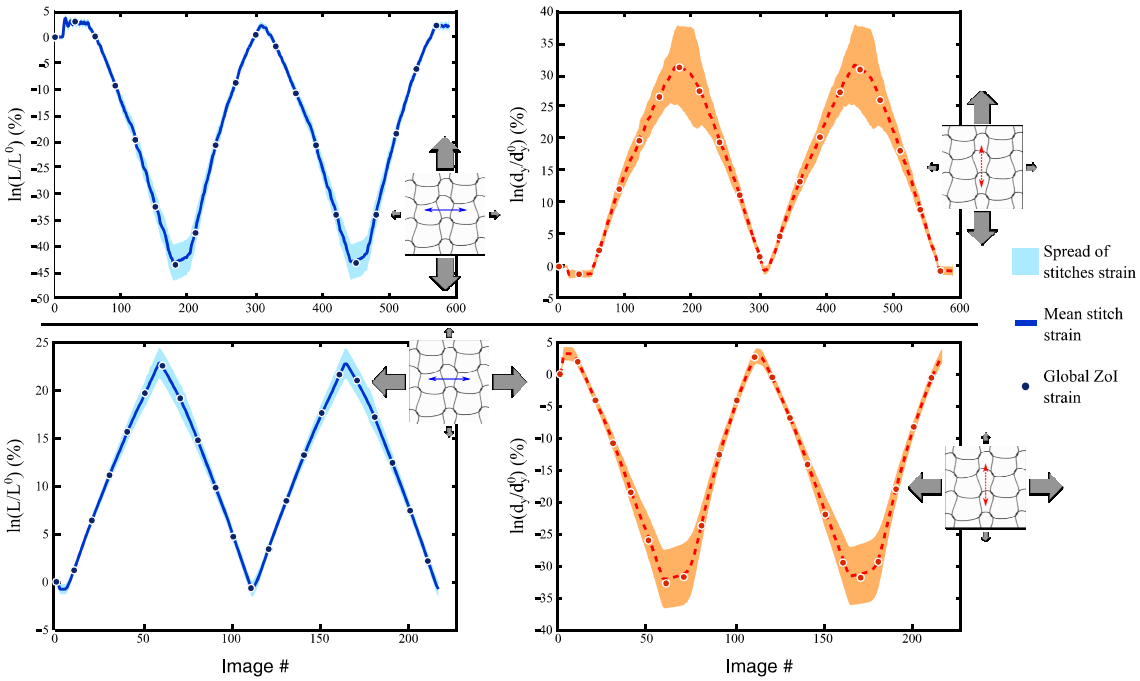

Figure V.15. Correspondence between global area of interest strains and local loops dimensions variations in wale-wise tension (top) and course-wise tension (bottom)

enization method in that direction may lead to slightly larger errors but remains in the confidence interval.

3.2.3 Boundary force distributions

Boundary forces distributions are then analyzed at strain increments A, B, C, and D, for each load case in uniaxial tension to verify the quasi-unixial loading hypotheses. Those distributions are presented along edges E1 and E4 for reasons presented in Chapter III.

In a first time, forces distributions are presented for the wale-wise uniaxial tension test. In chapter III, silicone membranes in their deformed shape presented a concave edge shape, resulting in a distribution showing an increasing force close to corners (springs 1 & 2 and 18 & 19) and a uniform distribution in springs in between. In the case of uniaxial tension on knitted textiles, the sample deformed shape shows edges concave in the tensile direction and convex in the transverse direction (Figure V.16). A similar distribution as obtained with silicone membranes is attained on edge E4, while an opposite distribution is present on edge E1 because of the edge convexity (Figure V.17). In the tensile direction, normal force is considered uniform between springs 4 and 13 included, with a deviation of $\pm 8\%$ for step B, C, and D. At step A, only spring 1 is off the uniformity criterion with a deviation of 20%. Along edge E1, normal force distribution is highly heterogeneous, with a variation of approximately $\pm 27\%$ in the central area between springs 3 to 17 at steps B, C, and D, and $\pm 33\%$ for all springs at step A. This non-uniformity is mainly caused by the low forces measured during loading, inducing a strong influence of measurement errors and springs defects (initial length, placement, knit loop geometry, *etc.*).

Along edge E1, tangential forces are almost non-existent, either because of the low normal forces than because of the low angle formed by springs compared to their initial normal position. Along edge E4, in another hand, normal forces induce stronger tangential forces, with a distri-

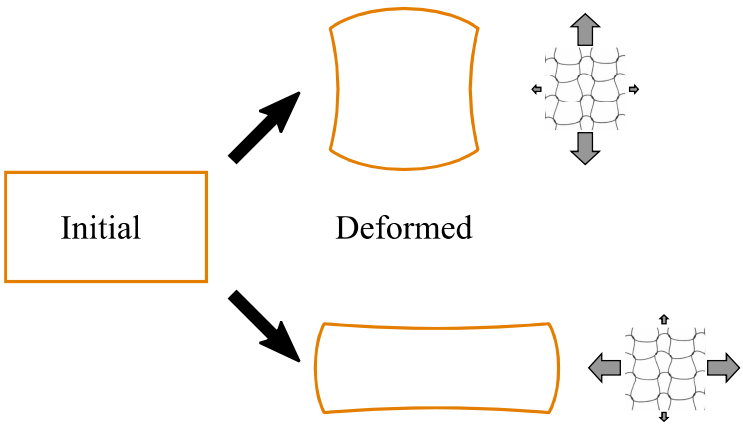

Figure V.16. Schematic representation of the ZoI deformed shape in uniaxial tension.

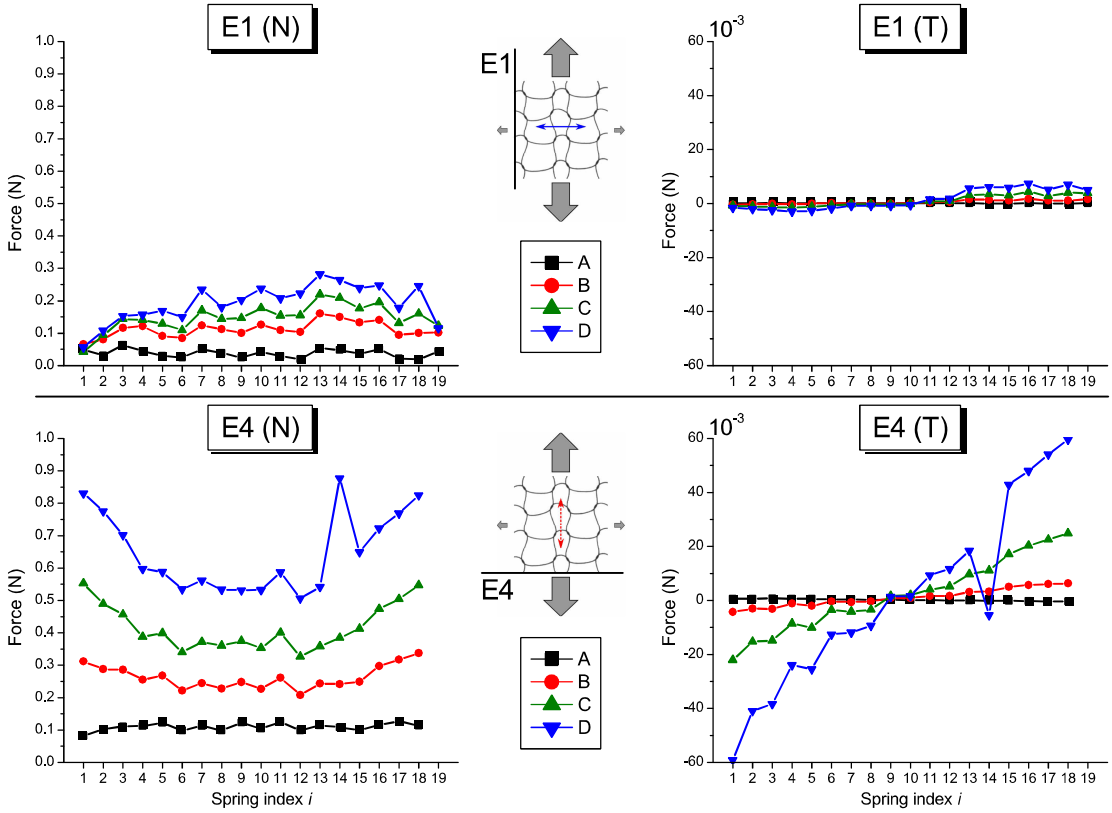

Figure V.17. Boundary forces measurement along edges E1 (top) and E4 (bottom) during wale-wise tension, normal component N is on the left side, and tangent component T on the right side; Values are given at strain increments A, B, C, and D

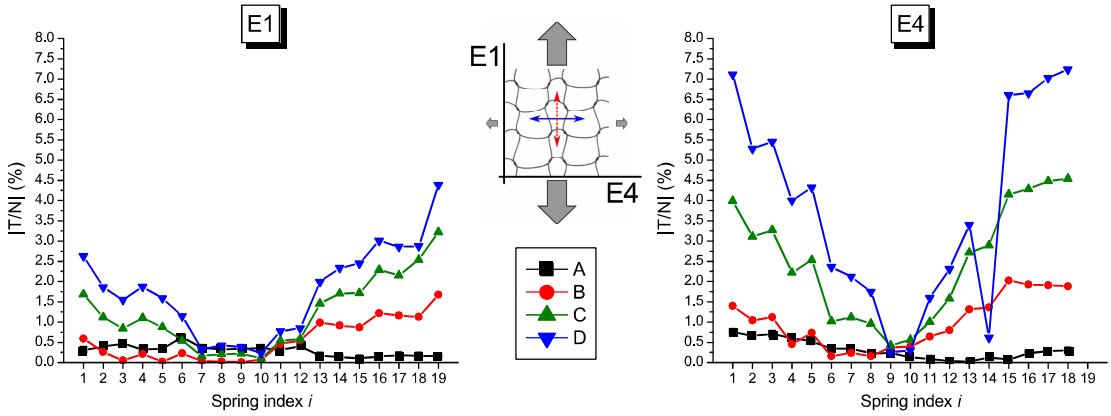

Figure V.18. Tangent component T over normal component N ratio (in %) along edges E1 (left) and E4 (right) during wale-wise tension; Values are given at strain increments A, B, C, and D

bution consistent with observations realized on silicone membranes. The criterion for negligible tangential forces has been introduced in Chapter III, equal to $R \leq 5\%$, is controlled in the case of uniaxial tension. Along edge E1, the ratio $\left|\frac{T}{N}\right|$ is always inferior to 5% (Figure V.18). The boundary conditions applied are thus considered equivalent to simple tension. Along edge E4, in the zone defined previously as uniform in regard to normal forces, the ratio obtained verifies the criterion introduced, validating the absence of shear forces in the sample. However, on external springs, this ratio overcomes the maximum value of 5%, unlike tests performed on silicone membranes on which the ratio remained under 4%.

As for the tensile test in the wale direction, in course-wise tension edge E1 possesses the "U-shape" distribution on normal forces and the opposite distribution on edge E4 (Figure V.19). On edge E1, the center zone between springs 3 and 18 included is poorly uniform, with a variation of $\pm 46\%$ around the mean value. The same observation is performed on edge E4 where the normal force variation between springs 3 and 17 included represents 57% of the mean value. Stitch warping defects, amplified by the sample strains as well as attachment points instabilities for springs aligned with the tensile direction on segments S2 and S4, are the cause of this distribution non-uniformity.

Tangential forces distributions are of the same configuration as for tests carried out on silicone membranes, with however an off-center zero value on edge E1, obtained on spring 12 instead of spring 10, which correspond to a vertical translation of 5 mm, i.e. 12% of edge E1 length. Despite the normal forces lack of uniformity during such test, the 5% criterion on ratio $\left|\frac{T}{N}\right|$ is verified all along edge E1, and on 18 over 19 springs on edge E4, with the dismissed value equal to 6%. This criterion allows to neglect shear effects in course-wise uniaxial tension as well.

These uniaxial tensile tests present satisfactory tangential over normal forces ratio ($\leq 8\%$), even with large displacements of springs attachment points. However, in course-wise uniaxial tension, the transverse normal force (along edge E4) is relatively close or equal to the normal forces in the tensile direction (edge E1). This implies that this loading case can not be considered as a uniaxial loading case. In addition, a "buffer-zone" can be drawn between the sample working area outer edges and uniform zone of width equal to 3 springs.

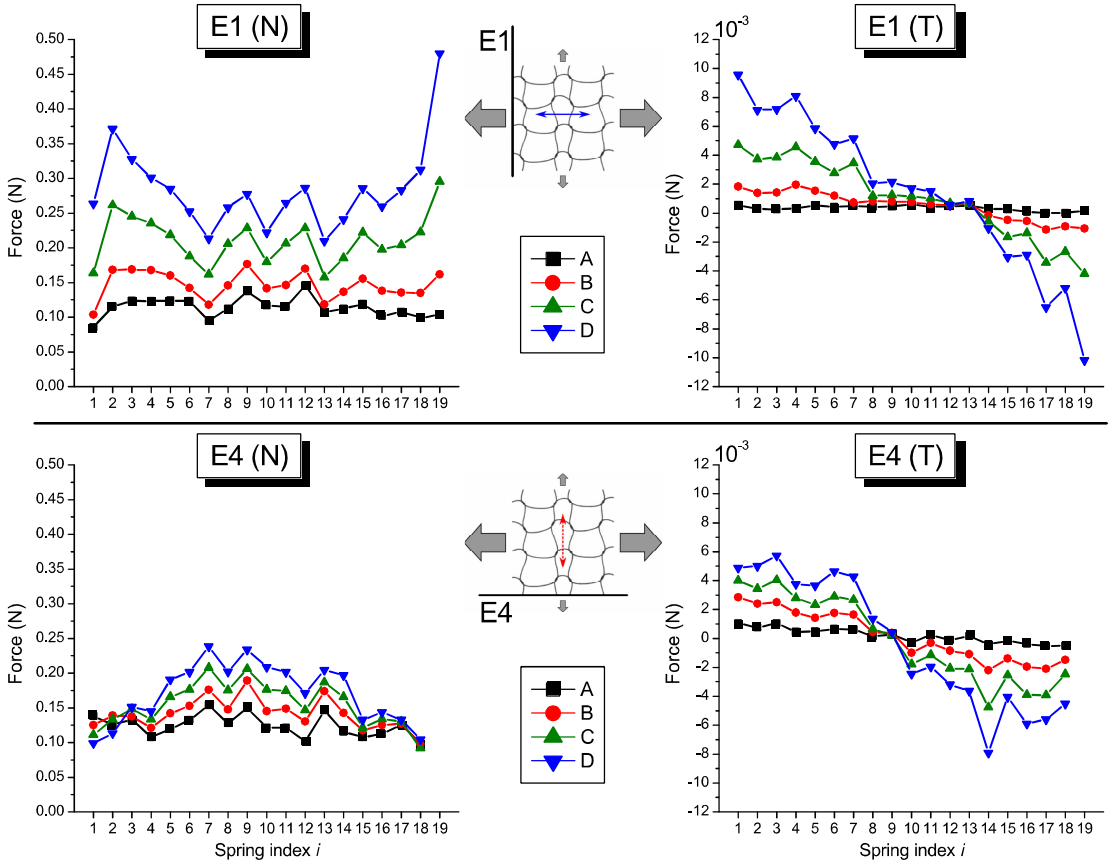

Figure V.19. Boundary forces measurement along edges E1 (top) and E4 (bottom) during course-wise tension, normal component N is on the left side, and tangent component T on the right side; Values are given at strain increments A, B, C, and D

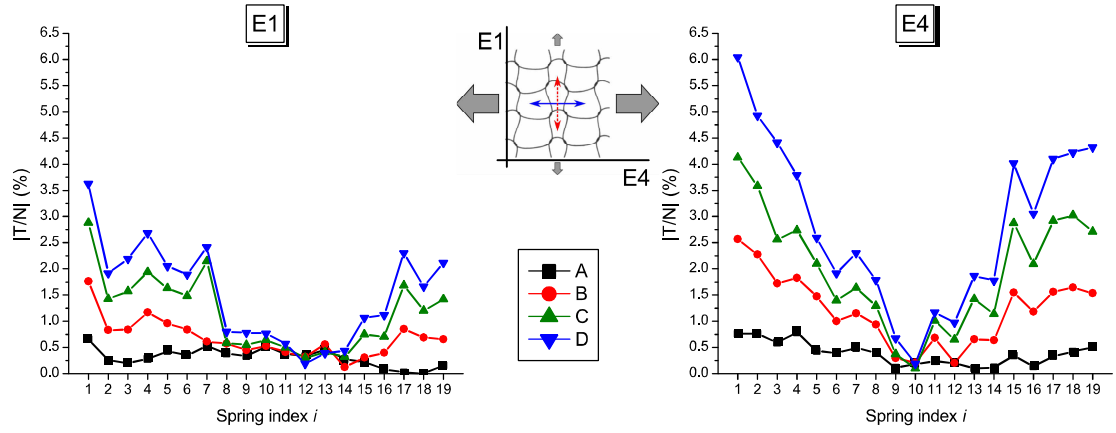

Figure V.20. Tangent component T over normal component N ratio (in %) along edges E1 (left) and E4 (right) during course-wise tension; Values are given at strain increments A, B, C, and D

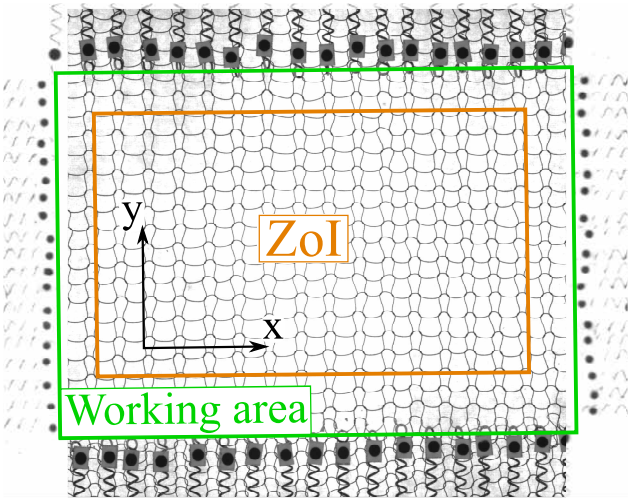

Figure V.21. Representation of the textile working area (green outline) and Zone of Interest (ZoI - orange outline)

3.3 Biaxial tension

In this section are presented experimental results obtained in biaxial tension for the knitted NiTi textile tested in uniaxial tension in previous section (Section 3.2). The macroscopic behavior is first presented, followed by the evolution of stitch dimensions and mean representative geometry during loading. Finally, boundary forces distributions are analyzed for this loading case.

3.3.1 Stress-strain relations

For this test, Figure V.21 depicts the sample zone of interest (orange) and the working area (green). The maximum strain used to carry out the loading case is measured with visual extensometers (camera 1), one for each direction, following the movement of one spring target on each working area edge. The maximum strain defined for this test is equal to 10%, and the strain rate to 0.02 $s^{-}1$. Two cycles of loading/unloading are performed.

Principal strains of the working area $\epsilon^{Workingarea}$ (lines) and the zone of interest ϵ^{ZoI} (symbols) are presented during the two loading cycles (Figure V.22). The control strain $\epsilon^{Workingarea}$ follows the desired equi-biaxiality condition during the first loading. This strain differs after the first loading and for the next cycle because of the constant grip speed, the sample anisotropy, and the friction causing residual strains after unloading. Principal strains of the zone of interest ϵ^{ZoI} (symbols) resulting from such test, however, dramatically differ from the working area strains. There are two main causes for this difference. The first cause rises from the spring attachment method. In the wale direction, springs are attached on long segments which may bend excessively under the effect of spring forces. This bending induces large springs target displacement but no strain on the corresponding knit loop. The second mechanism comes from the “buffer-zone” strains. This zone is defined as the area comprised between the zone of interest and the working area borders. In the course-wise direction, the segment bending under spring loads is reduced because of the segment shorter length. Therefore, the buffer-zone deformation in the course direction is very large to generate the large difference seen between working area strain $\epsilon_x^{Workingarea}$ and zone of interest strain ϵ_x^{ZoI}. Nevertheless, some stabilization occurs after the first unloading since strains (both working area and ZoI) in the second cycle reproduce strains of the first cycle

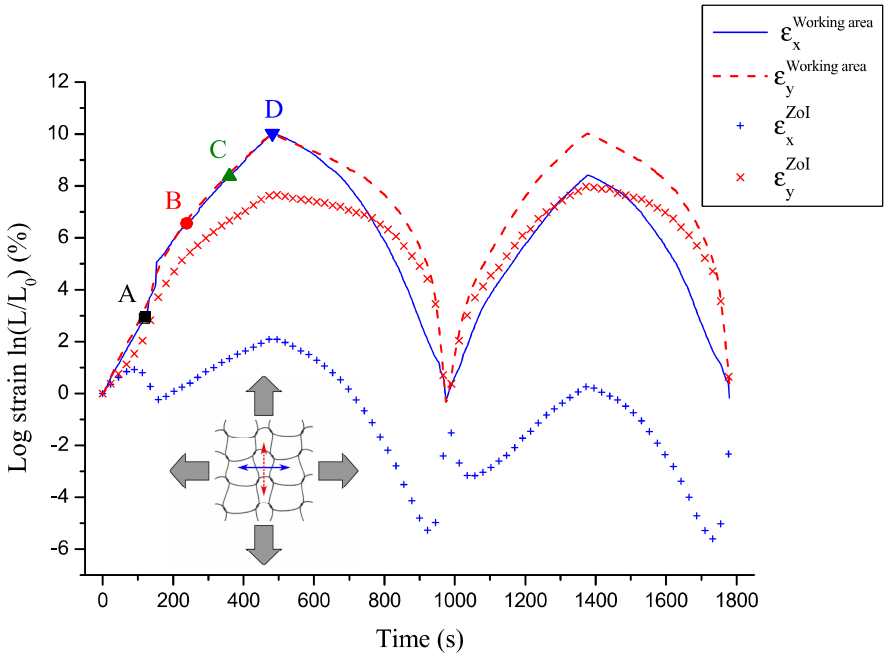

Figure V.22. Strains measurements of the sample working area (lines) and ZoI (symbols) in principal directions.

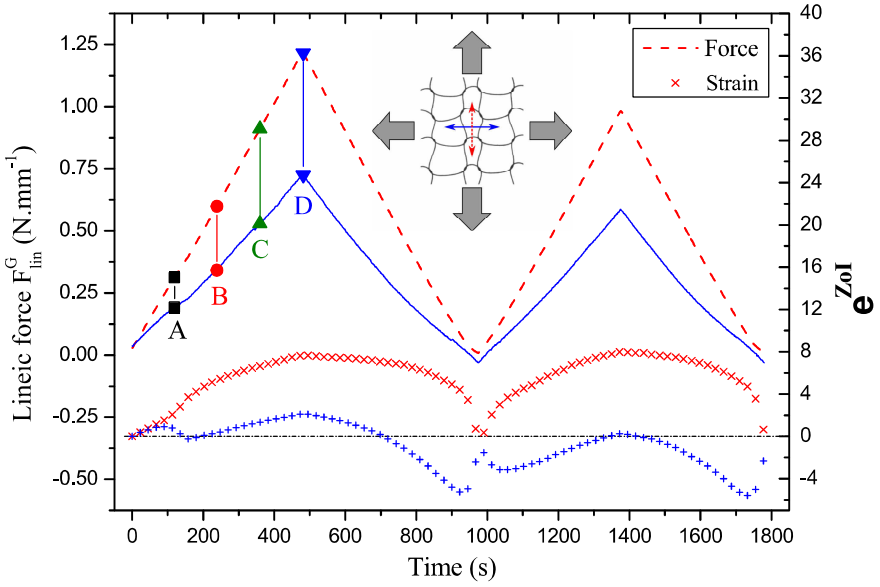

Figure V.23. Macroscopic behavior of the sample ZoI in force (left scale, lines) and strains (right scale, symbols) in time.

minus the loading step between $t = 0$ and $t = 150$ s.

Despite the non-monotonic zone of interest strains during such biaxial test, resulting macroscopic lineic forces evolution is monotonic and linear in time (Figure V.23), which implies that the control sequence is actually performed on macroscopic forces instead of strains.

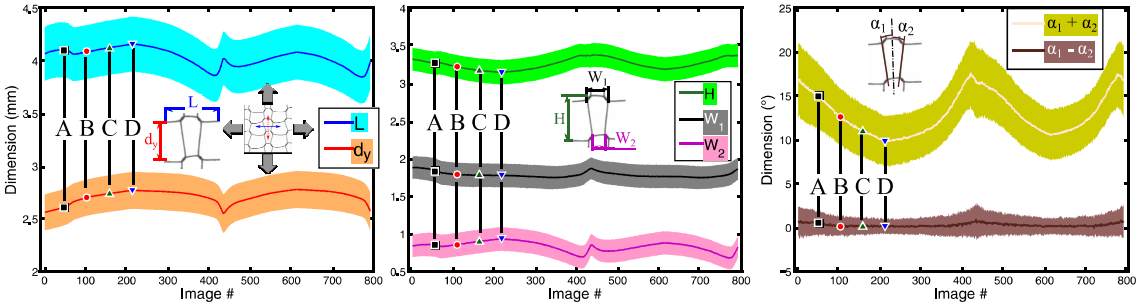

Figure V.24. Loop dimension variations during loading cycles in biaxial tension

3.3.2 Representative loop geometry under loading

Similarly as the presentation scheme used for uniaxial tension test (Section 3.2.2), the knit loop mean representative geometry, as well as the standard deviation associated with each dimension, is studied during loading cycles. The mean values are represented in thick lines while the standard deviations correspond to the colored area around, drawn at $\pm\sigma$ (Figure V.24).

As for the uniaxial tension tests, the knit loop length L and knit rows distance d_y vary correspondingly to the zone of interest strains, with a constant standard deviation. The biaxial loading does not imply dimensions standardization.

In opposition, knit loop height H varies in the opposite way as d_y, decreasing under the effect of loading, while maintaining a constant standard deviation. This is due to two main deformation mechanisms, different or absent in uniaxial tension. The first mechanism is the straightening of segments S1 and S3, implying a lower height H even if a constant spacing d_y is considered, as the middle points of segments S1 and S3, namely M_1 and M_2 used to measure the stitch height move toward each other as the segment straighten. The second part is the decreasing contact distance between C_1 and C_2, allowing for a slightly higher distance d_y, even if a constant height is taken. The loop greater width W_1 mean value and standard deviation remain practically constant, with a decrease of less than 10% of the mean value. The loop smaller width W_2 follows an evolution similar to the loop length L with a constant standard deviation. This is due to locking preventing the wire to slide between two contacting loops, and only the rotation around z-axis of segments S2 and S4 and segments S1 and S3 axial strains allow the textile to deform in the course direction (x-axis).

The stitch mean angular opening $\alpha_1 + \alpha_2$ and its standard deviation absolute value are decreased by 35% at the end of the first loading. This is due to the deformed loop shape, which becomes almost rectangular under biaxial loading. This deformed shape can be observed with the knit loop widths W_1 and W_2 variations. The mean warping value $\alpha_1 - \alpha_2$ remains stable around its initial value, while the standard deviation decreases significantly during loading, to reach a 50% reduction at step D. The locking happening in the case of biaxial loading implies the straightening of the loops segments S1 to S4. The phenomenon removes defects present initially because of the manufacturing and shape-setting processes which was responsible for the warping standard deviation increase in course-wise uniaxial tension (Section 3.2.2).

Therefore, biaxial loading does not allow stitch dimensions uniformization, notably because of the lack of sliding which prevent stitches height and length to balance. Yet, locking allows reducing shape defects (warping and opening) contrarily to course-wise uniaxial tension.

The stitches strains are computed following Eq. V.1 using dimensions L and d_y, and the

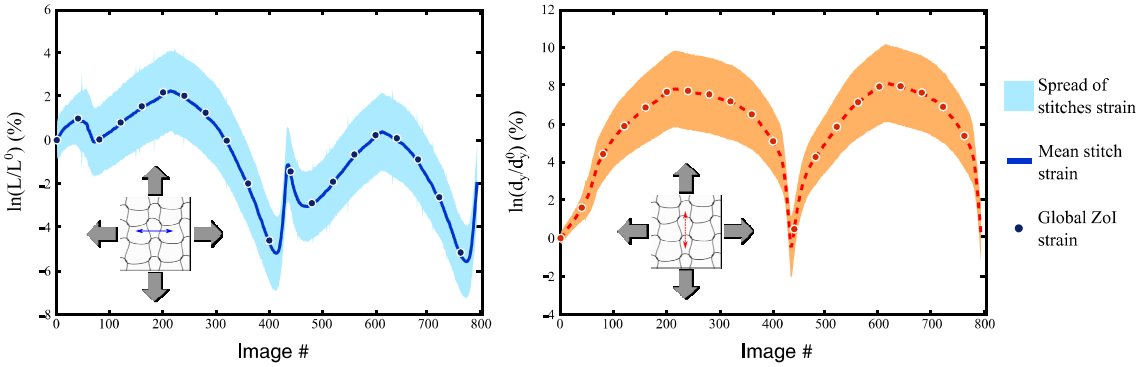

Figure V.25. Correspondence between global area of interest strains and local loops dimensions variations in biaxial tension

mean value (thick line) as well as the corresponding standard deviation (colored area) are presented Figure V.25 and compared to the zone of interest strains. Knit loops strains appear poorly uniform, with a standard deviation increasing with loading up to 100% increase in course direction and 200% increase in wale direction. Yet, the mean stitches strains reproduce the zone of interest strains, allowing to use the homogenization method and study the behavior of the mean representative loop with care.

3.3.3 Boundary force distributions

Normal (N) and tangential (T) boundary forces distributions are plotted for steps A, B, C, and D along edges E1 (top) and E4 (bottom) (Figure V.26).

Along edge E1, no corner effects are present as all springs are comprised around $\pm 15\%$ around the mean normal force, yet this spread is too large to consider this distribution uniform. Springs attachment points instability is the main cause of this non-uniformity. Along edge E4 however, springs hooking points are very stable, and the central zone between springs 2 and 18 included is therefore uniform at $\pm 2\%$ around the mean value, and external springs 1 and 19 differ only from 10% and 15% respectively. This value is of the same order as measured with silicone membranes where external springs where off by 12% to 13%. Yet, in the case of knitted textiles, only one spring at each edge extremity is to be considered non-uniform, as opposed to two for silicone membranes. Normal force distributions on this edge highly uniform.

The tangential forces distribution along edge E4 presents a similar shape as obtained in uniaxial tension and with silicone membranes, yet off-center of 30% of the edge length. The zero position remains stable during loading, indicating potential lack of symmetry in the displacement field along x-axis, inducing a larger angle between current and initial spring axis for springs 11 and above than symmetry would impose. Along edge E1, the distribution appears randomly spread and is consequence of springs hooking points instability coupled with measurement precision, springs initial defects, and knit loops geometry defects. Yet, the ratio $\left|\frac{T}{N}\right|$ obtained on both edges is always less or equal to 3%, verifying the previously defined 5% criterion, and validating the biaxial loading hypothesis (Figure V.27).

The biaxial loading hypotheses are therefore verified in this case. This indicates that the application of boundary conditions is not responsible for the large differences in working area and zone of interest strains.

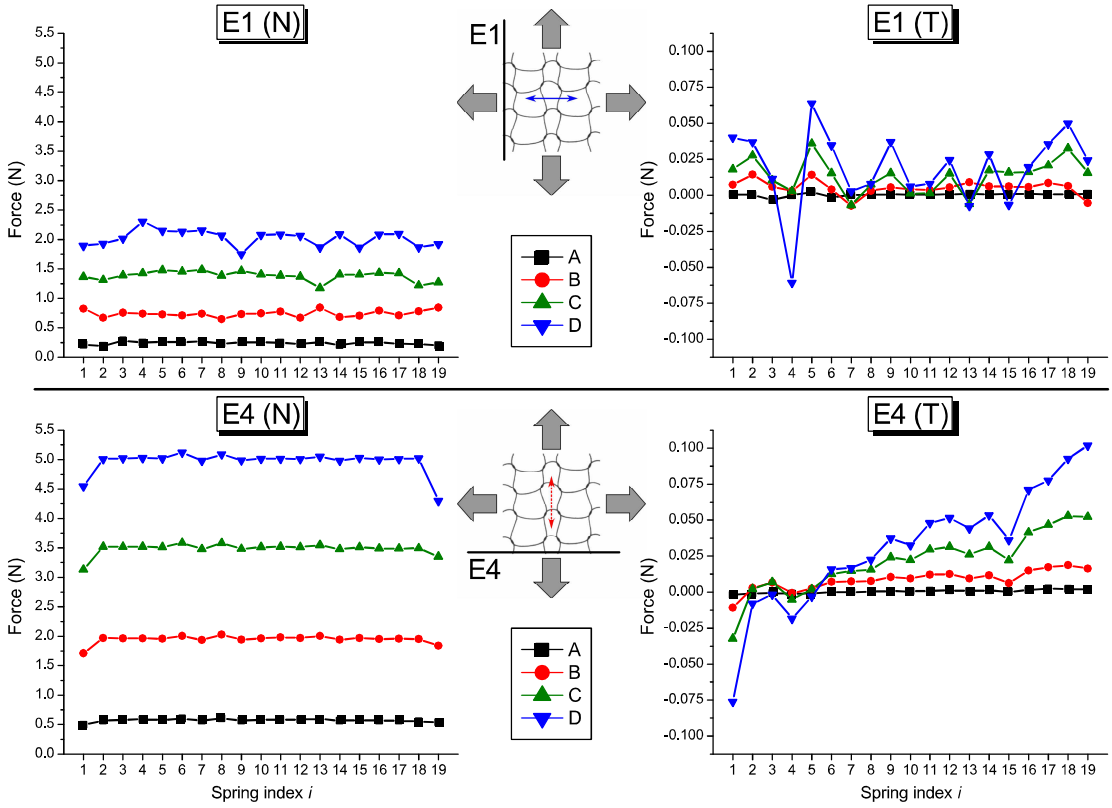

Figure V.26. Boundary forces measurement along edges E1 (top) and E4 (bottom) during biaxial tension, normal component N is on the left side, and tangent component T on the right side; Values are given at strain increments A, B, C, and D

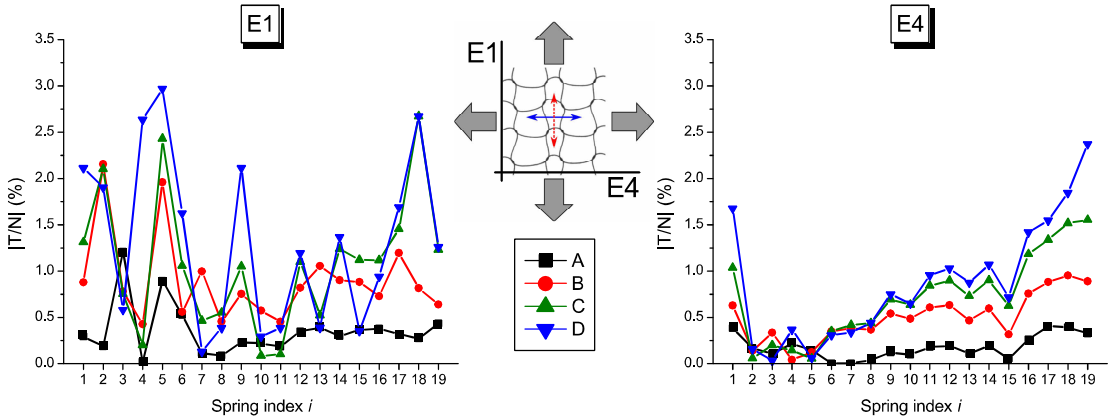

Figure V.27. Ratio of tangent component T over normal component N (in %) along edges E1 (left) and E4 (right) during biaxial tension; Values are given at strain increments A, B, C, and D

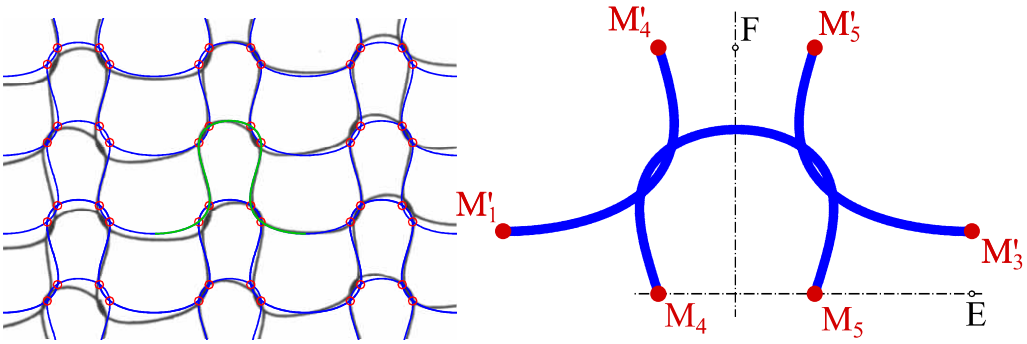

Figure V.28. Initial geometry identified on experimental picture created using parametric equations presented in Chapter 2.2

4 Numerical simulations

In order to evaluate the influence of material parameters on the textile macroscopic behavior, the finite element model presented in Chapter IV is used with the initial geometry defined in Section 2.2. The numerically obtained macroscopic behavior is opposed to experimental results to assess for the model precision, in uniaxial and biaxial tension. Then, after validation, the model is used to analyze the influence of the material austenite Young's modulus and wire-to-wire friction coefficient on the knit loop mechanical behavior.

4.1 Model parameters

4.1.1 Boundary conditions

The finite element geometry is computed using the parametric equations defined in Chapter IV, Section 2.2.1, and the mean representative knit loop dimensions presented in Table V.1 (Figure V.28). This initial geometry yet presents a large penetration of both $[M_4, M_2]$ and $[M'_1, M'_4]$, and identically for segments $[M_2, M_5]$ and $[M'_5, M'_3]$, because of the stitch curvature in the z direction. In order to remove such penetration, the stitch distance d_y is reduced artificially, and a pre-load force F_0^y is applied taking the experimental value (Figure V.29). During this step, horizontal gradients $C_{ux}(t)$, $C_{vx}(t)$, and $C_{wx}(t)$ are maintained equal to zero. Therefore, the vertical symmetry and knit length L are preserved during this step, but vertical translation is allowed. This pre-loading step is common for all three loading cases.

The next step depends on the loading case chosen. In the case of uniaxial tension, the stitch kinematic is constrained in the axial direction and determined with the experimental zone of interest axial strain. In the transverse direction, a constant force F_0 is imposed taken equal to the experimental value.

In the case of biaxial tension, a second pre-loading step is performed as experimental initial loading is different than uniaxial tension. This step is performed by imposing experimentally measured forces F_{0biax} in both x and y directions. Then, the complete stitch kinematic in x and y directions is imposed to control stitch strains determined with experimental zone of interest strains (Figure V.22).

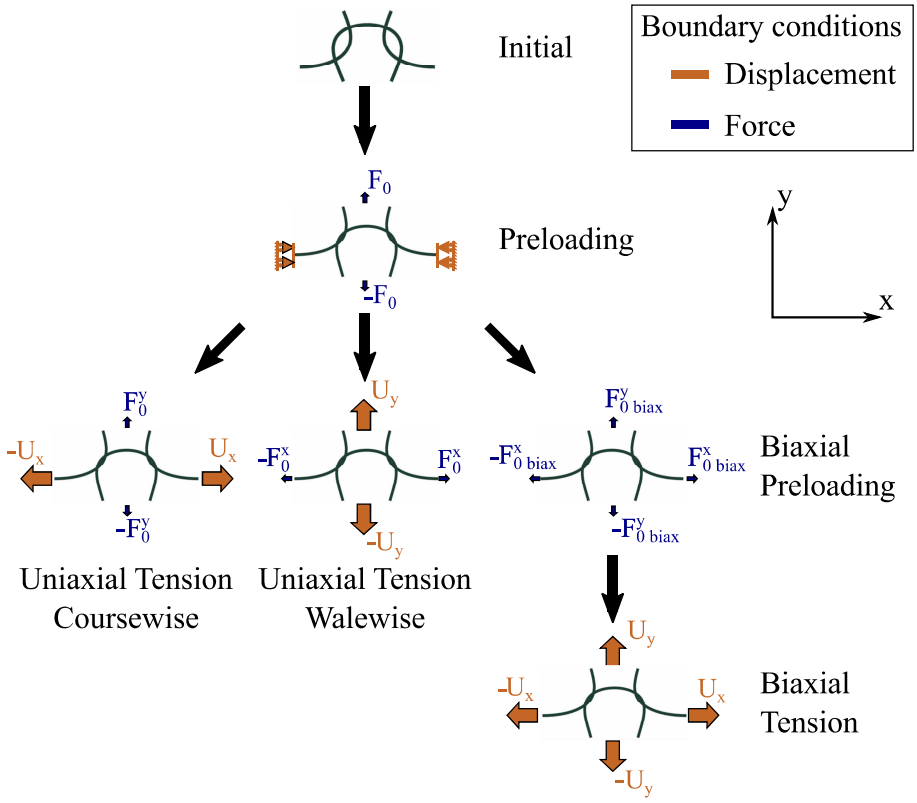

Figure V.29. Loading steps for the finite elements model depending on the tensile direction.

Table V.2. Superelastic material parameters identified on wire uniaxial tension (Figure V.30) for use with the Auricchio superelastic material behavior model.

Austenite	E_A	ν_A	σ_{As}	σ_{Af}		ϵ_l	T_0
	46 GPa	0.45	210 MPa	160 MPa			
Martensite	E_M	ν_M	σ_{Ms}	σ_{Mf}	σ^c_{Mf}	3.33 %	22^o C
	18 GPa	0.45	553 MPa	563 MPa	774 MPa		

4.1.2 Material behavior models

Using the tensile test carried out on an heat treated NiTi wire (Figure V.30), necessary parameters used for Auricchio superelastic material behavior are identified, and presented Table V.2.

A simplifying approximation has also been introduced by using a linear elastic material of Young's modulus E equivalent to austenite modulus E_A (Figure V.30). This approach allow considerable computing time reduction compared to a model using superelastic behavior model. The macroscopic behavior of both methods are compared with experimental results in further sections.

4.2 Uniaxial tension

Firstly, uniaxial tension is studied. The knit loop mechanical behavior obtained numerically is first compared to experimental results, using a linear elastic material model first then the superelastic material behavior. The material is then chosen and the influence of the austenite Young's

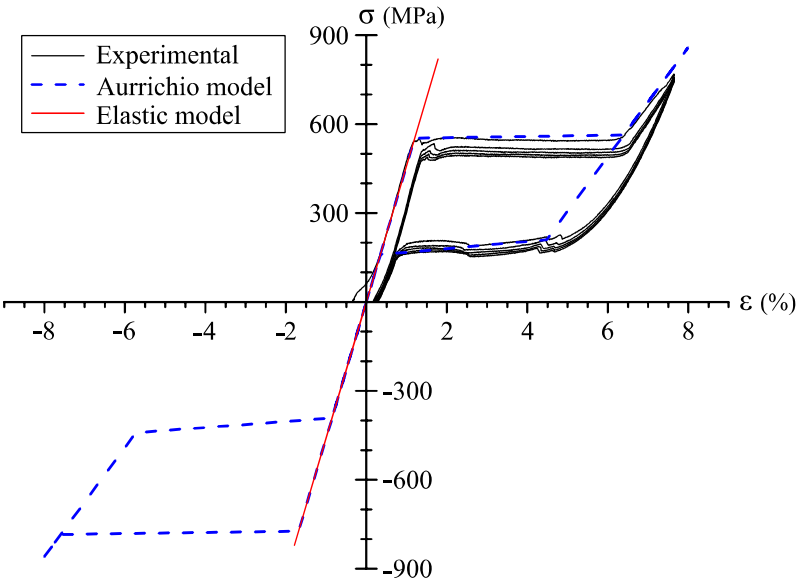

Figure V.30. Material behavior models used in the numerical analysis using a linear elastic material (red) and Aurrichio model (blue dash) fitted on wire tension experimental results (black).

modulus E_A and the friction coefficient on the stitch mechanical behavior is analyzed numerically.

4.2.1 Macroscopic behavior

The stitch macroscopic behavior in wale-wise tension using linear elastic material is presented in Figure V.31. The lineic force versus axial logarithmic strain overestimates by 50% experimental results at the loading start, up to step B where this overestimation decreases to less than 4.5% at step D. The unloading however reproduces precisely experimental unloading, with an overestimation equal to 5%. The transverse logarithmic strain computed numerically overestimate experimental results by 23.5%. The strain hysteresis is also overestimated by 95%.

In order to verify for these errors possible origin, the superelastic material behavior model is then used in the same conditions. The resulting macroscopic behavior is compared to numerical results with linear elastic material and to experimental results (Figure V.32). The overall lineic force response is similar to the elastic material response, excepting with the appearance of oscillations. The almost equivalent hysteresis (2.5% difference) between the two simulations indicates that only geometrically induced hysteresis (friction and structural) is present. The material stress state is expected to remain on the linear part common between the two materials (Figure V.30). The transverse strain versus axial strain relation yields similar observation. It can be determine that the material behavior is not the cause of the model errors. Experimental errors (initial loops uniformity, strain field uniformity, *etc.*) are most likely responsible, for a large amount, of the errors measured with the numerical model.

The stitch macroscopic behavior with linear elastic material in course-wise uniaxial tension is compared to experimental results (Figure V.33). The finite elements model reproduces the experimental response of the textile in lineic force versus logarithmic axial strain with 7% error during loading. The numerical unloading path overestimates experimental results because the finite element model fails to reproduce the textile stabilization happening experimentally, highlighted by the shifting zero position after the first loading and constant after the next loading cycle (Figure

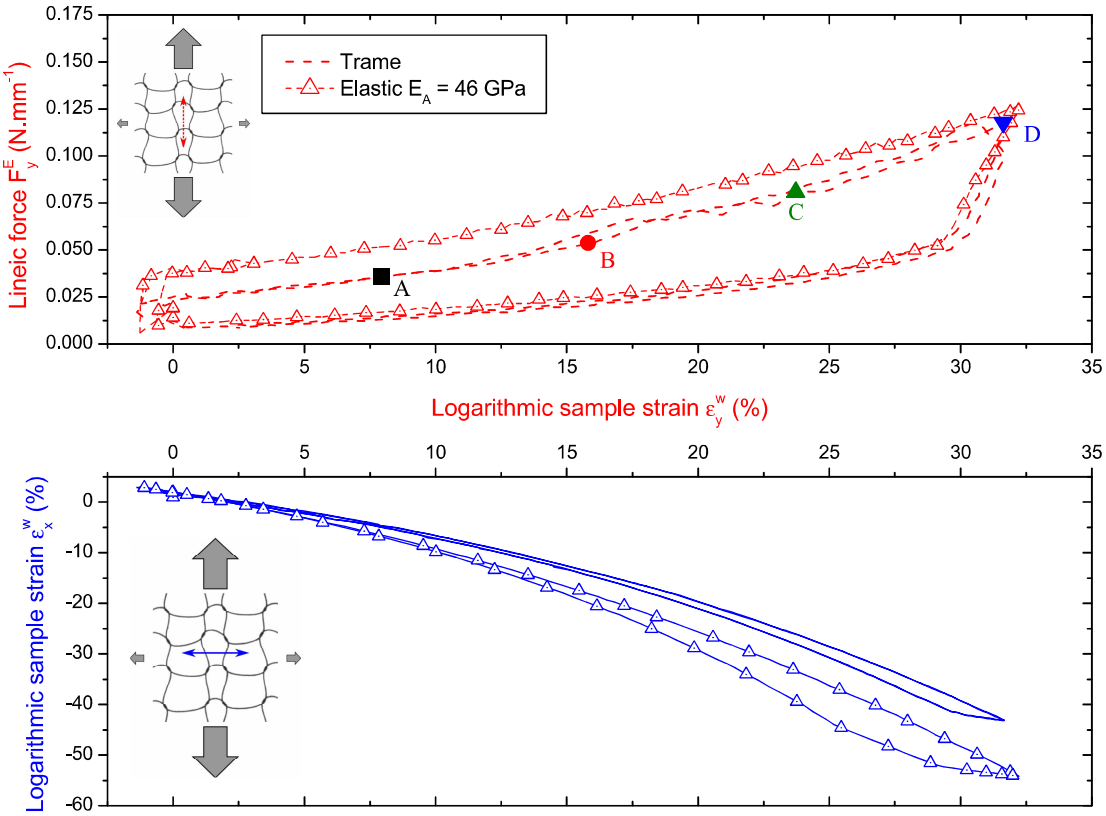

Figure V.31. Comparison between FE model and experimental results in uniaxial wale-wise tension using simple elastic material model.

V.11). The transverse logarithmic strain is underestimated by 14% while the hysteresis is overestimated by 19%.

The stitch macroscopic behavior with the superelastic material is then compared to the linear elastic model and experimental results together (Figure V.34). With such material model, the stitch maximum lineic response is overestimated by 20%, while unloading is correctly reproduced. The transverse maximum logarithmic strain is still underestimated yet by 9% with the superelastic material, while the hysteresis is overestimated by 50%. The higher lineic force hysteresis in the case of the superelastic material indicates that geometrically induced hysteresis is not only responsible for the whole mechanical hysteresis observed. The use of a superelastic material, however, does not increase significantly the model precision, while still increases computation times by a factor 6 approximately.

Despite the presence of martensitic transformation in course-wise tension, the linear elastic model reproduces the stitch experimental mechanical response better in both course-wise and wale-wise tension.

To assess for the presence of martensitic transformation in the wire during loading, the section maximum Von Mises stress σ_{mises}^{max} is plotted along the normalized curvilinear abscissa for strain increments A, B, C, and D. Because of the stitch initial geometry, mesh, and loading and geometrical vertical symmetry, only half of the loop is represented for clarity purposes, *i.e.* segments $[M_4, M_2]$ and $[M_1', M_4']$, each plotted on a separate graph. Contact points are named C_1 and C_2 and C_1' and C_2' for segments $[M_4, M_2]$ and $[M_1', M_4']$ respectively, and contact pressure along the

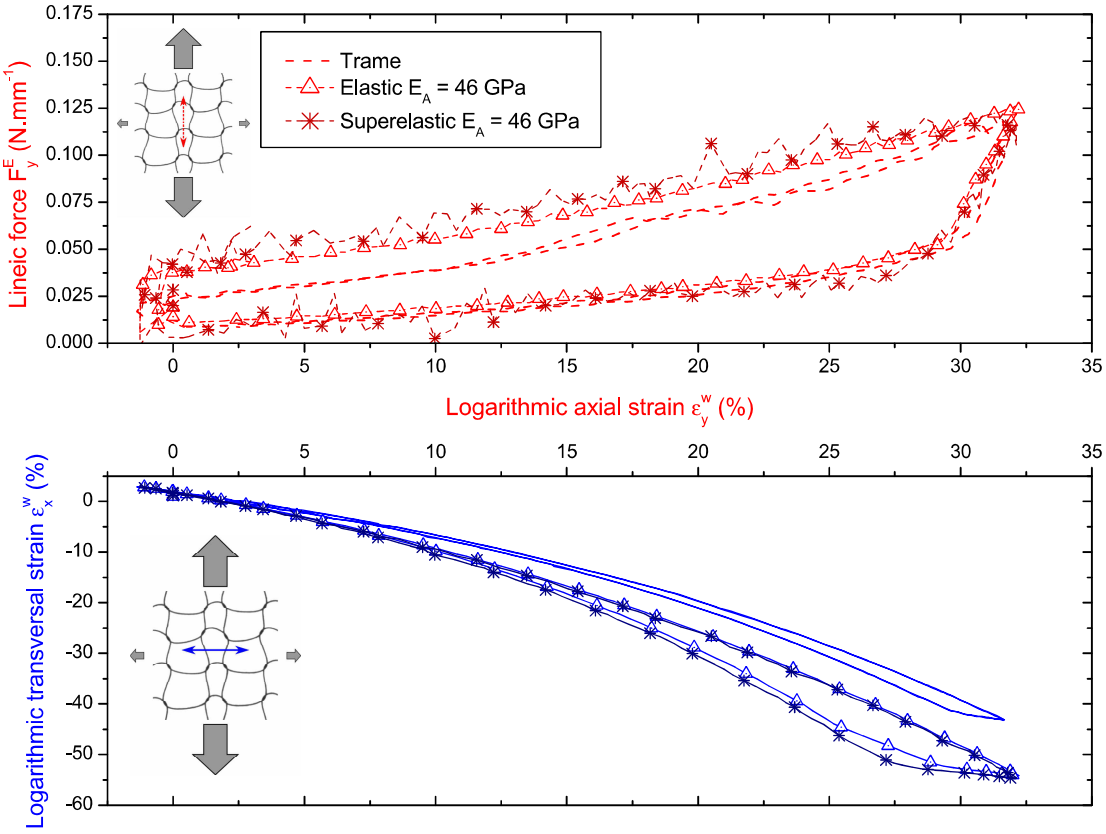

Figure V.32. Comparison between linear elastic (triangles) and superelastic (asterisks) material behavior models with experimental results (lines) in uniaxial wale-wise tension.

normalized curvilinear abscissa is plotted to detect their position.

The wale-wise uniaxial tension is first studied (Figure V.35). Bending occurring between M_4 and C_1 rises a maximum Von Mises stress lower than martensite start stress σ_{ms}. This threshold is only exceeded between contact points C_1 and C_2 until point M_2, after step B. Along segment $[M_1', M_4']$, the transformation stress is surpassed between points M_1' and shortly after C_1', at steps C and D. Martensitic transformation would therefore occur over a long curvilinear length in the wire. However, bending being the most preponderant deformation mechanism, transformed zone is located on the outer layers of the section. Therefore, the transformed asutenite volume represents only a small proportion of the total volume in the stitch. Furthermore, equivalent Von Mises stress does not allow separating tension to compression within the section, and as the compressive martensite start stress is generally 40% higher than its tension counterpart σ_{ms}, the worst case scenario has been used by placing the tension threshold for both tension and compression. Hence, the low martensite volume fraction and worst case scenario for compression explains the limited impact of using a superelastic behavior model.

Then, maximum Von Mises stress within the wire section is studied for the course-wise tension (Figure V.36). Along segment $[M_4, M_2]$, martensitic transformation start stress σ_{ms} is surpassed only at step D, at point M_2 vicinity, under the effect of the wire straightening. During loading, sliding induces a constant distance between contact points C_1 and C_2, while moving both points toward point M_4. The sliding distance traveled corresponds to 10% of the segment $[M_4, M_2]$ curvilinear length. Along segment $[M_1', M_4']$, the section maximum Von Mises stress surpasses

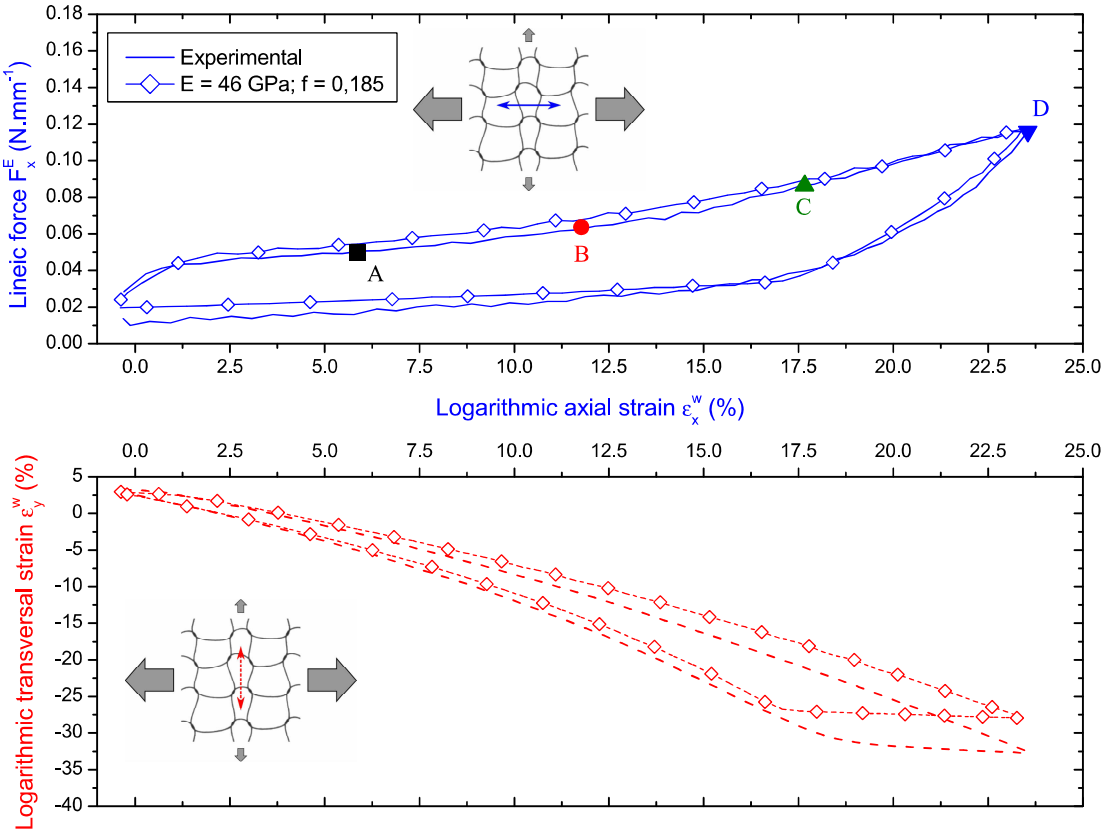

Figure V.33. Comparison between FE model and experimental results in uniaxial course-wise tension using simple elastic material model.

the martensite start stress earlier, from step C, in the vicinity of point M_1'. The maximum Von Mises stress is reached at contact point C_2', acting like the pivot for segment $[M_1', M_4']$ bending. For such loading case, martensitic transformation would still occur in the wire yet with a lower martensitic volume fraction as the threshold stress σ_{ms} is exceeded over a shorter wire length. This observation indicates that location of martensite transformation has a greater impact on the stitch macroscopic behavior than the volume fraction as using a superelastic material to model the course-wise tension lead to larger hysteresis in both lineic force and transverse strain.

Due to the low transformed austenite volumes, the linear elastic material is used for further analysis as it allows for better stitch macroscopic behavior simulation and large computation time reduction, usually by a factor 6.

4.2.2 Influence of Young's modulus

In order to provide with a first mechanical behavior analysis of knitted NiTi textiles and the influence of wire parameters, the austenite Young's modulus E_A impact over the knit loop macroscopic behavior is studied. Two values have been tested, namely 46 GPa and 70 GPa. The first value has been identified on the wire behavior in simple tension and corresponds to the elastic modulus on the first linear part of the load (Figure V.1). However, during this phase, R-phase appears more or less significantly and the austenite modulus computed on the whole charge blends together austenite and R-phase modulus. Usually, initial nickel-titanium austenite Young's modu-

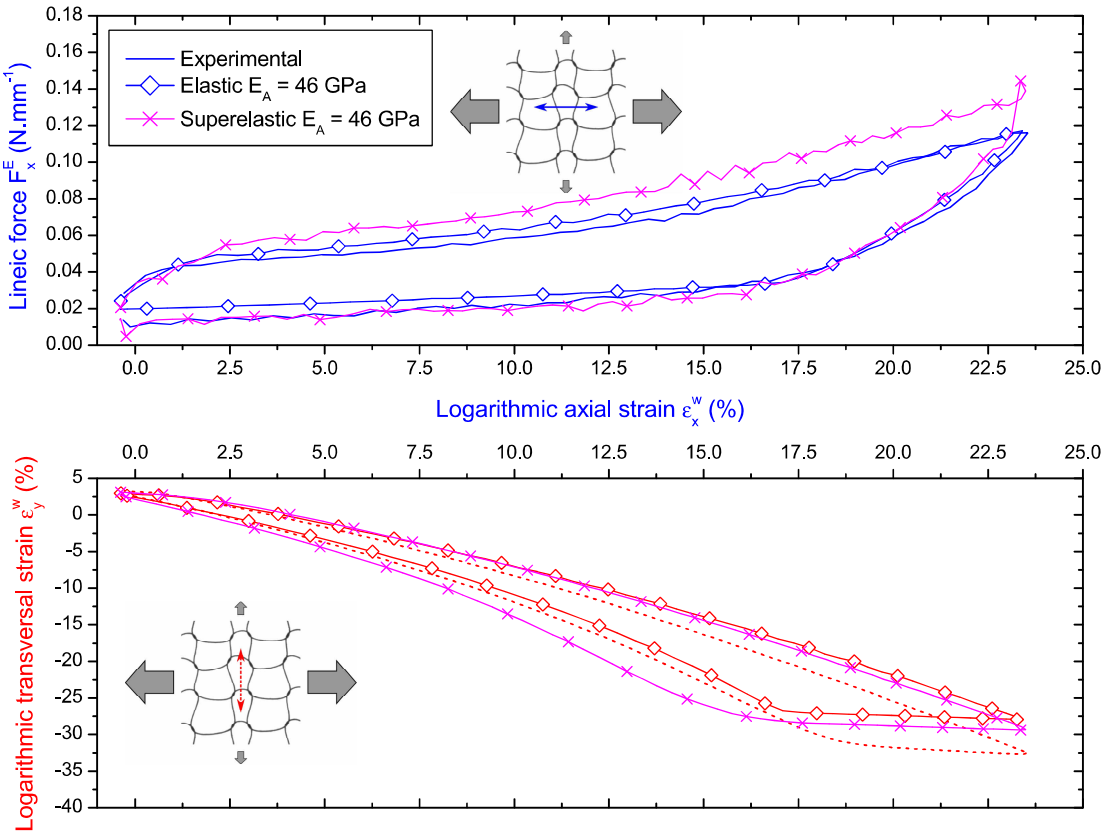

Figure V.34. Comparison between linear elastic (diamonds) and superelastic (crosses) material behavior models with experimental results (lines) in uniaxial course-wise tension.

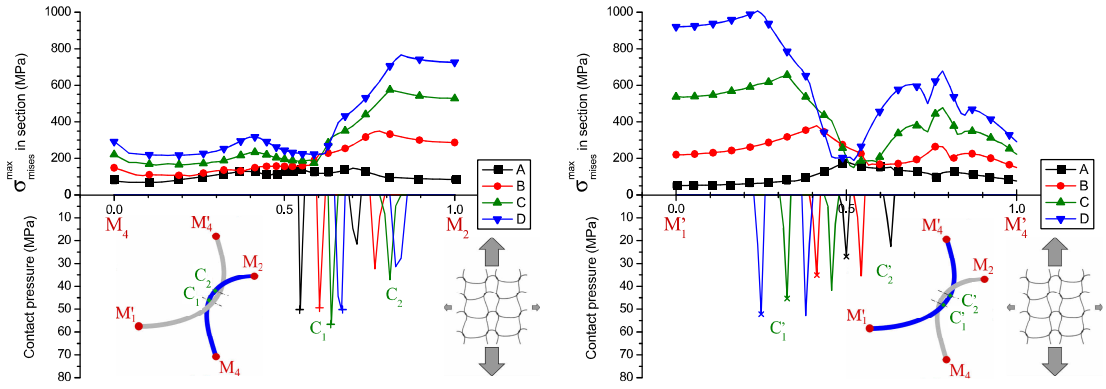

Figure V.35. Maximum mises stress (top) and contact pressure (bottom) in the wire section along normalized curvilinear abscissa between points M_4 and M_2 (left) and points M_1' and M_4' (right) using linear elastic material during uniaxial wale-wise tension at strains increments A, B, C, and D.

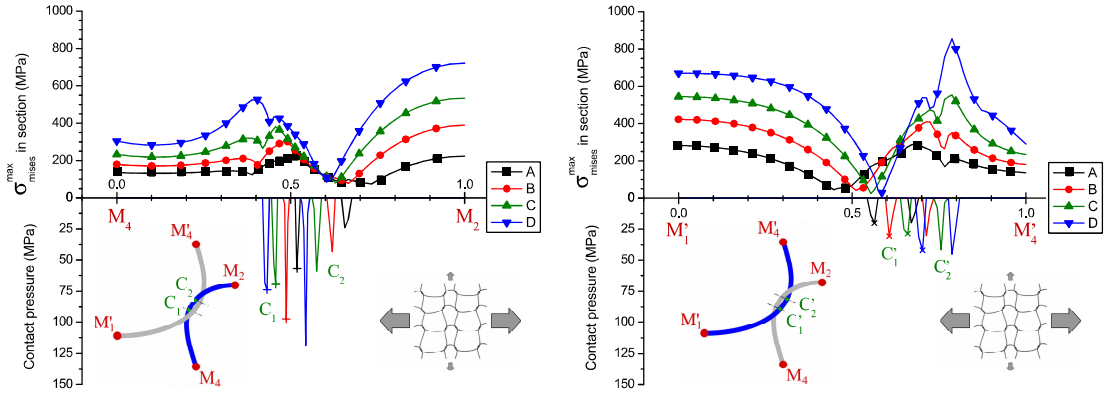

Figure V.36. Maximum mises stress (top) and contact pressure (bottom) in the wire section along normalized curvilinear abscissa between points M_4 and M_2 (left) and points M_1' and M_4' (right) using linear elastic material during uniaxial course-wise tension at strains increments A, B, C, and D.

lus is around 70 GPa.

Young's modulus influence is first analyzed in wale-wise tension (Figure V.37). Increasing Young's modulus induces a strong stiffening because of bending deformation mechanisms and stress levels presented previously (Section 4.2.1). At strain increment D, the lineic force response suffers a 35% increase. However, slopes at the unloading start are identical, and passed 20% strain, both unloading curves are superimposed over experimental results. This observation indicates that sliding only is present at this point. The transverse strain obtained with both moduli is, however, perfectly superimposed, indicating that the stitch Poisson's coefficient ν_{yx} is unresponsive to Young's modulus variation.

Then, the influence of such moduli is studied in course-wise tension (Figure V.38). Similar conclusions as the wale-wise uniaxial tension case are drawn, namely the lineic force stiffening with a maximum force increased by 35% and identical initial unloading slopes. Passed 17% strain, both models fit experimental results. Like previously, only sliding is present from this point. The transverse strain however slightly shifts with the change in Young's modulus, with a 8% increase of transverse strain at strain increment D. Transverse strain hysteresis increases also by 15%, indicating that the stitch Poisson's coefficient is dependent on the material Young's modulus.

4.2.3 Influence of friction coefficient

The stitch deformation mechanism being also highly dependent on wire sliding, friction coefficient is a preponderant parameter in the mechanical response of knitted textiles. The influence of such parameter has been studied by using three distinct values for f, namely $f = 0.185$ found experimentally (Section 3.1), $f = 0.13$ found in literature [50], and $f = 0$ to verify the presence of structural hysteresis (hysteresis not created by friction nor material).

In a first time, the wale-wise tension is studied (Figure V.39). A decreasing friction coefficient f induces better fitting of experimental results at loading start. However, the lineic force response differs from experimental results at 15% and 2.5% strains and the maximum lineic force reached at strain increment D is decreased by 16% and 70% for $f = 0.13$ and $f = 0$, respectively. The absence of friction induces an almost stiffless stitch. Friction is therefore the most important parameter controlling the stitch mechanical response in lineic force in wale-wise tension. The error at the loading starts seen when using $f = 0.185$ is therefore potentially due to the preloading step

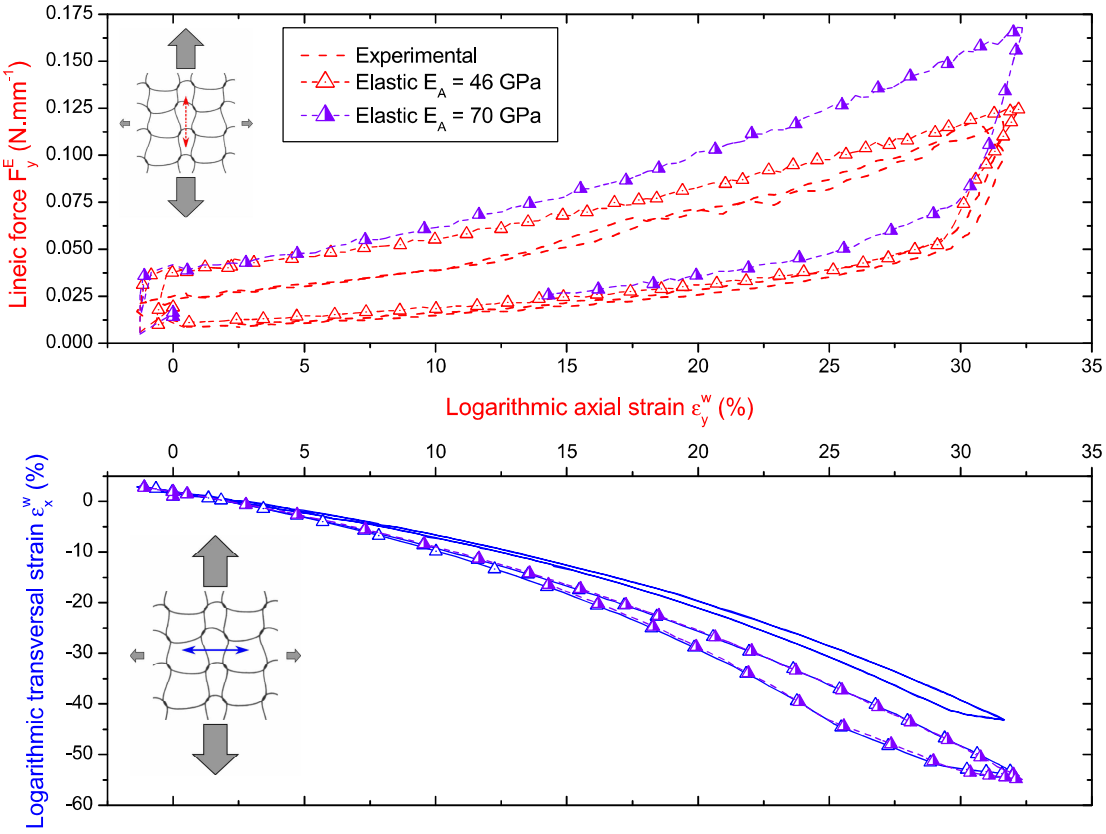

Figure V.37. Influence of Young's modulus on the mechanical behavior of the knit loop in wale-wise tension.

and friction occuring during this step. Maximum transverse strain, however, is barely increased by less than 3% for both $f = 0.13$ and $f = 0$. The strain hysteresis is almost insensitive to small f change but becomes nullified for $f = 0$. Hence, no structural hysteresis is detected in wale-wise tension.

Course-wise tension is then analyzed for its dependence on the friction coefficient (Figure V.40). The friction coefficient decrease induces, similarly to wale-wise tension, a softening of the stitch mechanical response. However, even with no friction the stitch produces a non-constant lineic force response, yet with a maximum value decreased by 40%. With $f = 0.13$, the maximum lineic force is reduced by 13%. The transverse strain increases with the reduction of friction coefficient, with 9% and 40% increase for $f = 0.13$ and $f = 0$, respectively. The strain hysteresis decreases with the friction coefficient, up to a zero value without friction. In this case again, no structural hysteresis is detected, and friction coefficient plays a less important role as in wale-wise tension.

4.3 Biaxial tension

The numerical model is used in this section to compute the knit loop mechanical response in biaxial tension, depending on the material behavior model used, and compared to experimental results. As for the uniaxial tension case, the material model in then chosen in regard to the stitch macroscopic behavior, and the influence of the austenite Young's modulus E_A and friction coeffi-

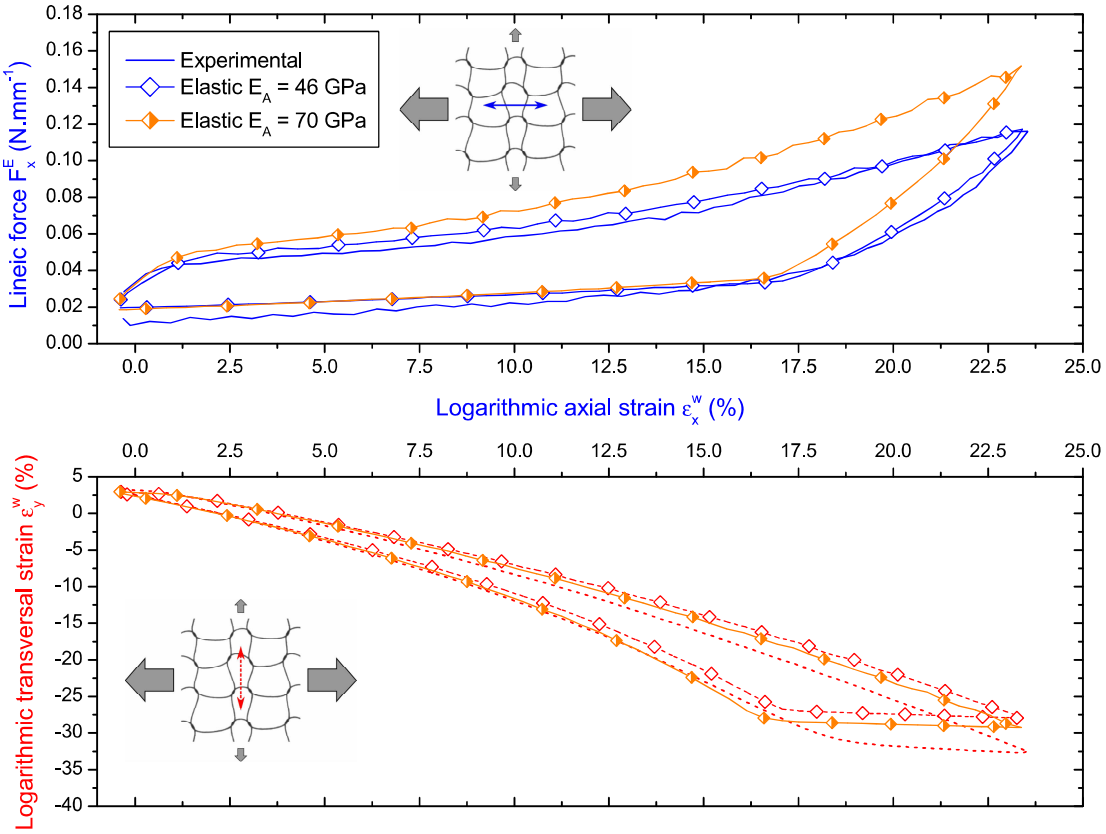

Figure V.38. Influence of Young's modulus on the mechanical behavior of the knit loop in course-wise tension.

cient f on the macroscopic behavior are analyzed. In this analysis, only the first loading cycle is studied.

4.3.1 Macroscopic behavior

The linear elastic material behavior is then used for biaxial tension and resulting stitch lineic forces are compared to experimental results (Figure V.41). Until time increment A, elastic material reproduces exactly experimental results. Then, after this step, elastic material starts to overestimate the experimental stitch response up to a factor 2.3 at step D for both course and wale direction. Therefore, superelastic material is used to model biaxial tension, and reproduces precisely the knit loop experimental mechanical behavior until step time B. From this point, the model underestimates experimental response by 17% in the wale direction and less than 3% in the course direction (Figure V.42). Taking into account hypothesis linked to initial knit loop and strains uniformity, the finite element model using superelastic material is validated in regard to the stitch macroscopic behavior and superelastic material behavior is used for further analysis.

Then, the section maximum Von Mises stress σ_{mises}^{max} along the curvilinear abscissa is studied for this loading case (Figure V.43).

Along segment $[M_4, M_2]$, the Von Mises stress exceeds the martensitic transformation stress σ_{ms} immediately at time A, between contact points C_1 and C_2 (Figure V.43), indicating the presence of martensitic transformation in the wire external layers. Along segment $[M_1', M_4']$, martensite appears at time A at the close vicinity of contact point C_2'. Because of stresses distributions

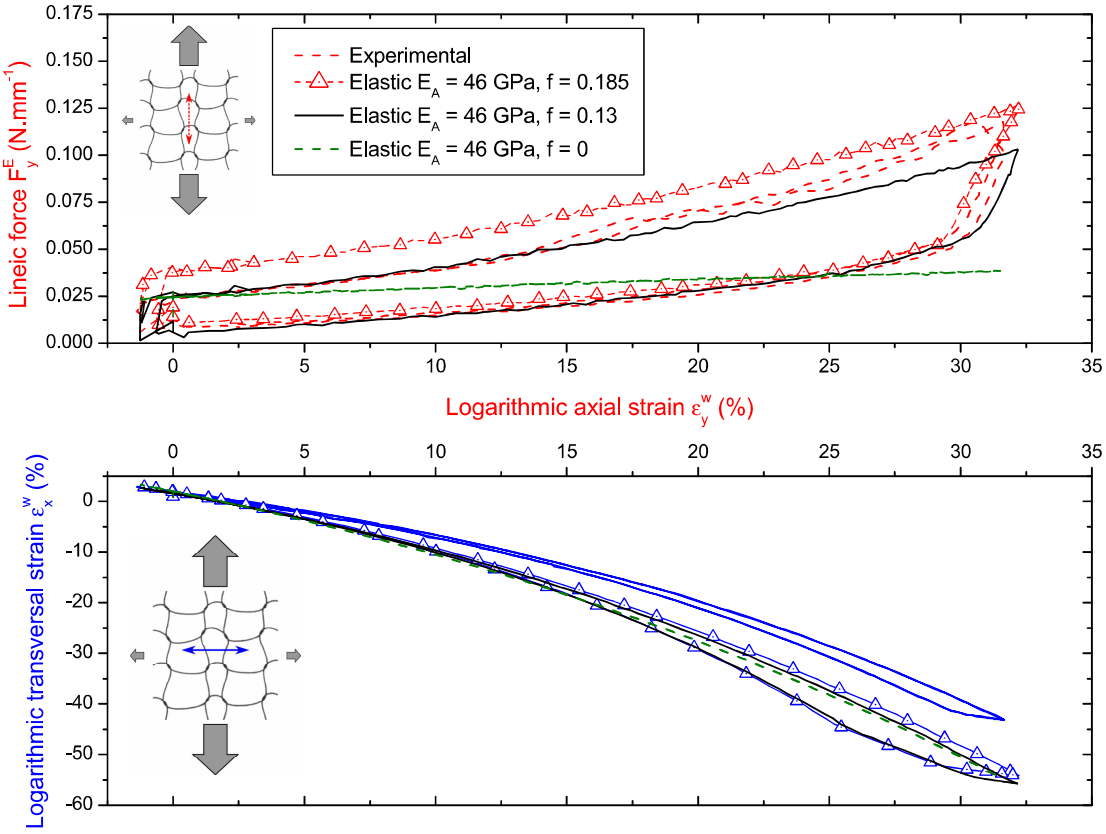

Figure V.39. Influence of the wire friction coefficient on the knit loop mechanical behavior in wale-wise tension.

in bending, martensite is expected to be located only in the external layers of the wire. As the martensite transformation start stress σ_{Ms} is surpassed only in a small length of the wire, a small portion of the wire volume is expected to transform into martensite. This low martensite volume yields similar results between the elastic material model and superelastic material model. Furthermore, stress level analysis in uniaxial tension highlights that surpassing martensitic transformation stress, even with maximum stress 50% higher, still yields correct simulation of the stitch macroscopic behavior with the linear elastic material.

However, since step time B, a large portion of segment $[M_4, M_2]$ curvilinear length possesses a maximum Von Mises stress superior or equal to the martensitic transformation stress, causing the lineic force response overestimation observed with the linear elastic material. Stress levels reached between contact points C_1 and C_2 for step times C and D would theoretically cause martensite plasticity, not taken into account in the model. However, only small shift in strains are present at the end of the first cycle, namely -1.2% and -0.5% for course and wale directions, respectively. The shift strains negative signs indicate that the shift is not plastic permanent strain but knit loops shape balance because of sliding and friction. Therefore, martensite plasticity is negligible.

Along segment $[M_1', M_4']$, stress levels are of similar magnitudes, with however a slower increase in time, as at time C, a longer portion of the segment curvilinear length possesses a maximum equivalent stress lower than the martensitic transformation stress. Contrarily, at time D, a slightly smaller portion of the segment curvilinear length lies below σ_{ms}, namely 6.3% of segment $[M_1', M_4']$ against 15.2% of segment $[M_4, M_2]$, with yet a peak maximum stress value lowered by

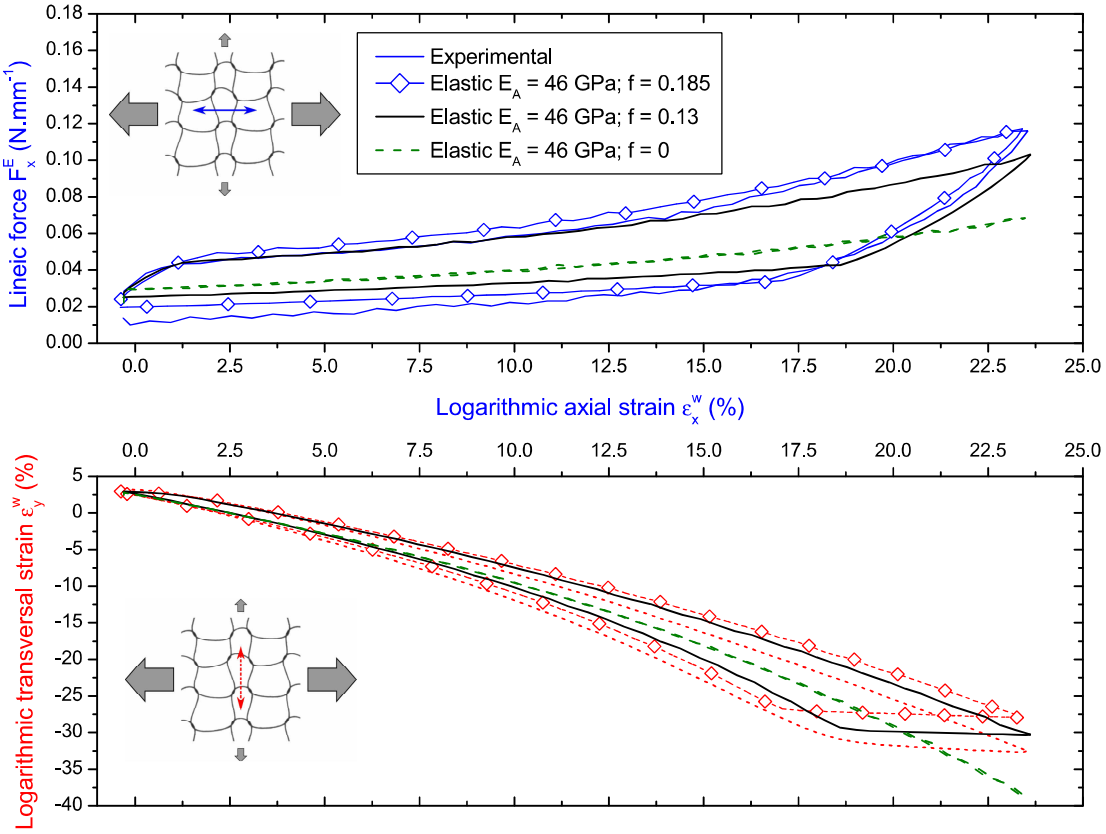

Figure V.40. Influence of the wire friction coefficient on the knit loop mechanical behavior in course-wise tension.

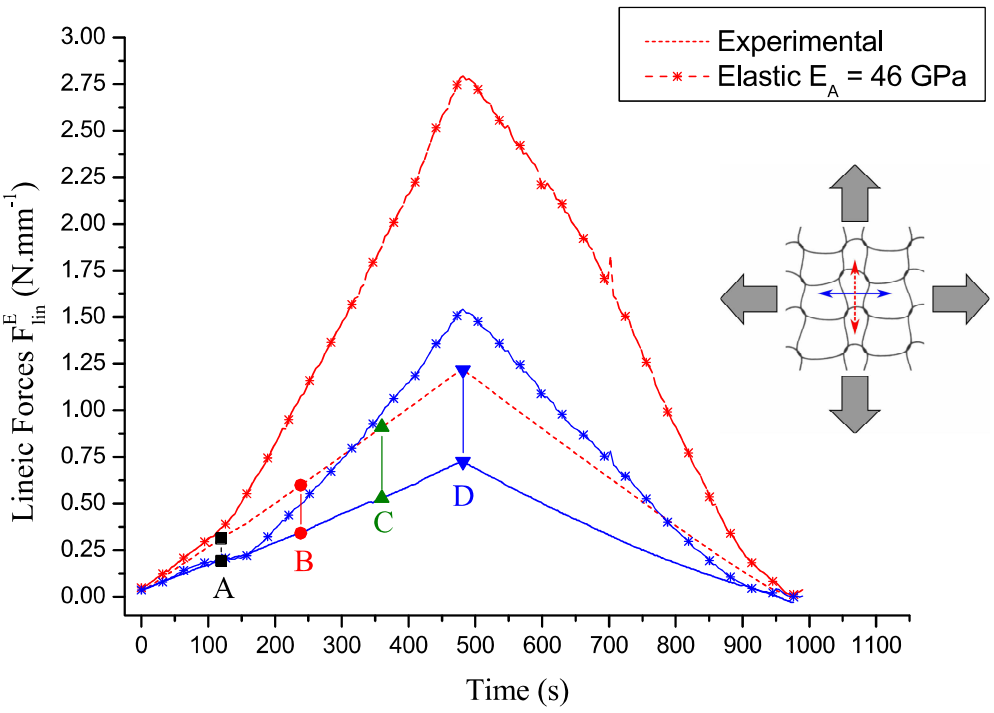

Figure V.41. Comparison between experimental (lines) and numerical lineic forces using linear elastic material (asterisks) during a biaxial loading cycle.

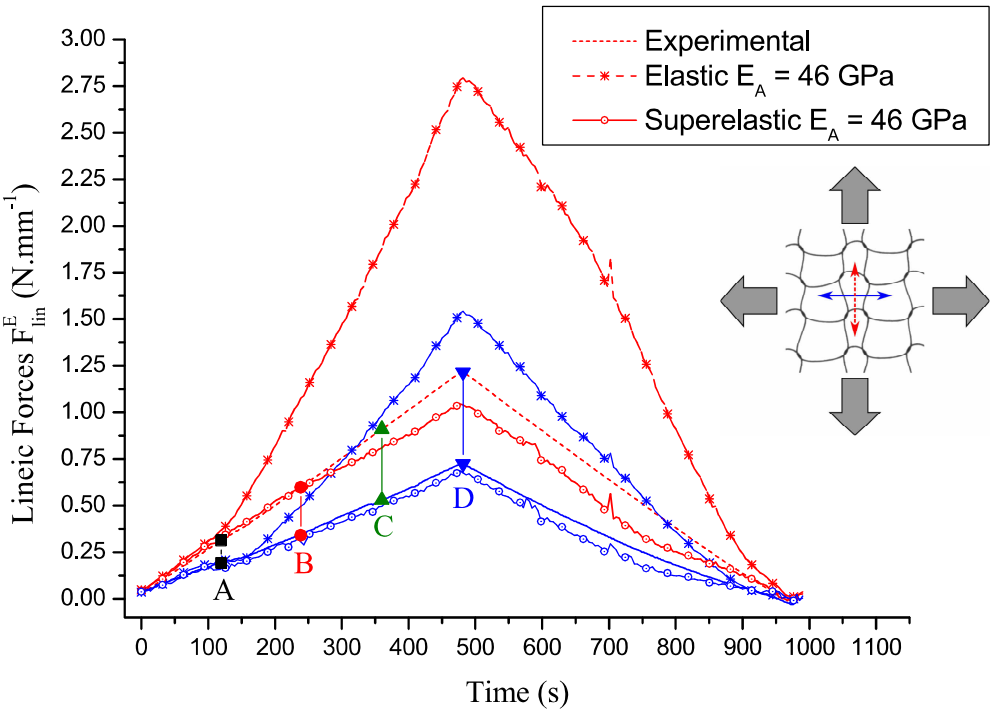

Figure V.42. Comparison between experimental (lines) and numerical lineic forces using linear elastic material (asterisks) and superelastic material (circles) during a biaxial loading cycle.

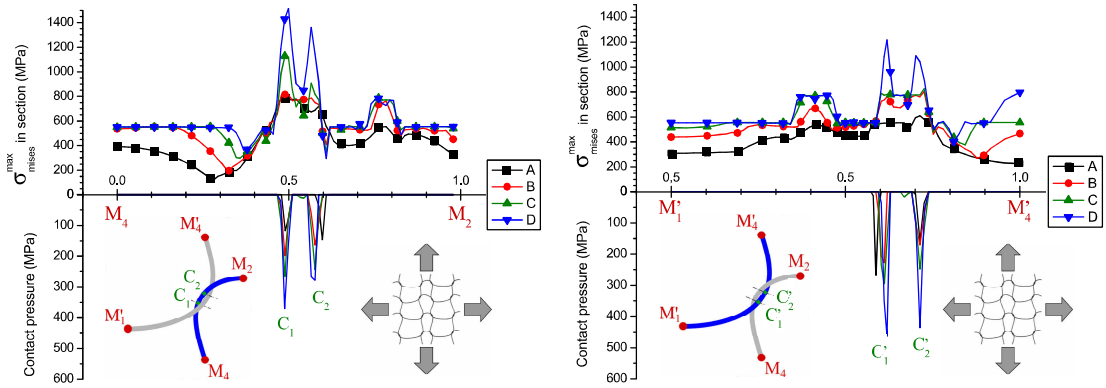

Figure V.43. Maximum mises stress (top) and contact pressure (bottom) in the wire section along normalized curvilinear abscissa between points M_4 and M_2 (left) and points M_1' and M_4' (right) using superelastic material during biaxial tension at strains increments A, B, C, and D.

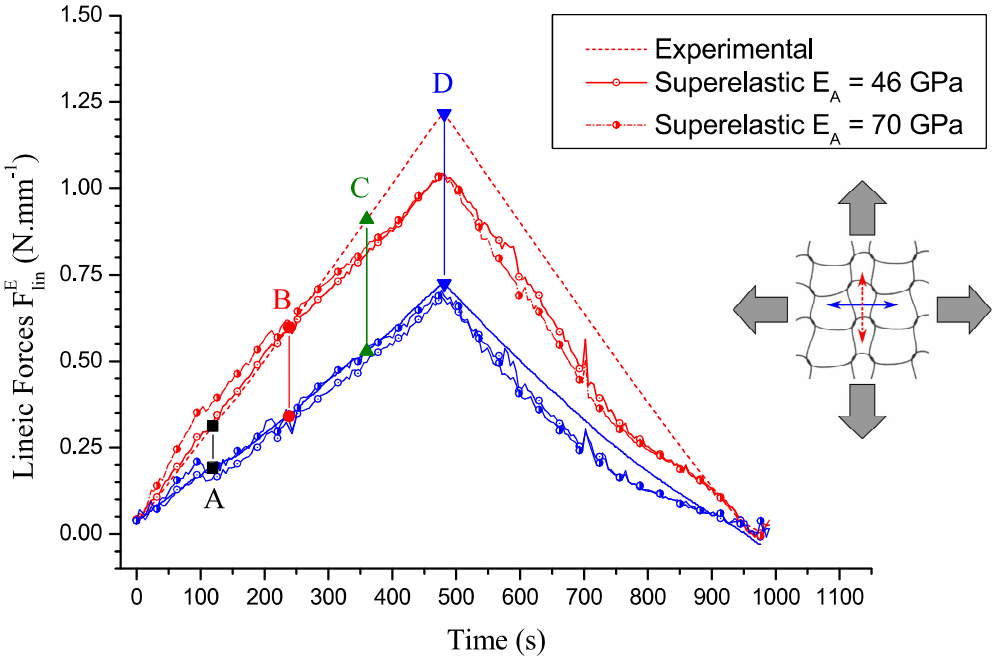

Figure V.44. Influence of Young's modulus on the lineic forces response of the knit loop in biaxial tension.

20%, and also located between contact points. The large martensitic volume fraction on this part of the loop confirms the overestimation induced by the use of the linear elastic material.

Finally, the position of contact points C_1, C_2, C_1', and C_2' varies only until step B. This indicates that sliding occurs only before this time, and friction coefficient is expected to yield an impact only on this part of the force response.

4.3.2 Influence of Young's modulus

As for uniaxial tension loading cases, the austenite Young's modulus influence on the stitch macroscopic behavior is studied in this section. Same modulus values as defined previously are used. The mechanical response is presented in Figure V.44.

The increase in Young's modulus induces an overestimation of lineic forces response yet only before step time B. This is explained by the presence of sliding and important bending before time B, inducing lower stress state in the section, thus a large austenite volume fraction. Hence, the impact of austenite Young's modulus is present only in this period. The maximum lineic forces in both directions are equal for the two moduli.

Another impact of the austenite Young's modulus appears during pre-loading, where the material remains in austenitic phase. The Young's modulus variation induces changes in the knit loop dimensions before the loading step, causing potential deviation at the macroscopic and microscopic scale.

4.3.3 Influence of friction coefficient

Finally, the influence of the friction coefficient on the stitch macroscopic behavior is studied for the biaxial loading case with the superelastic material model, and three values of friction

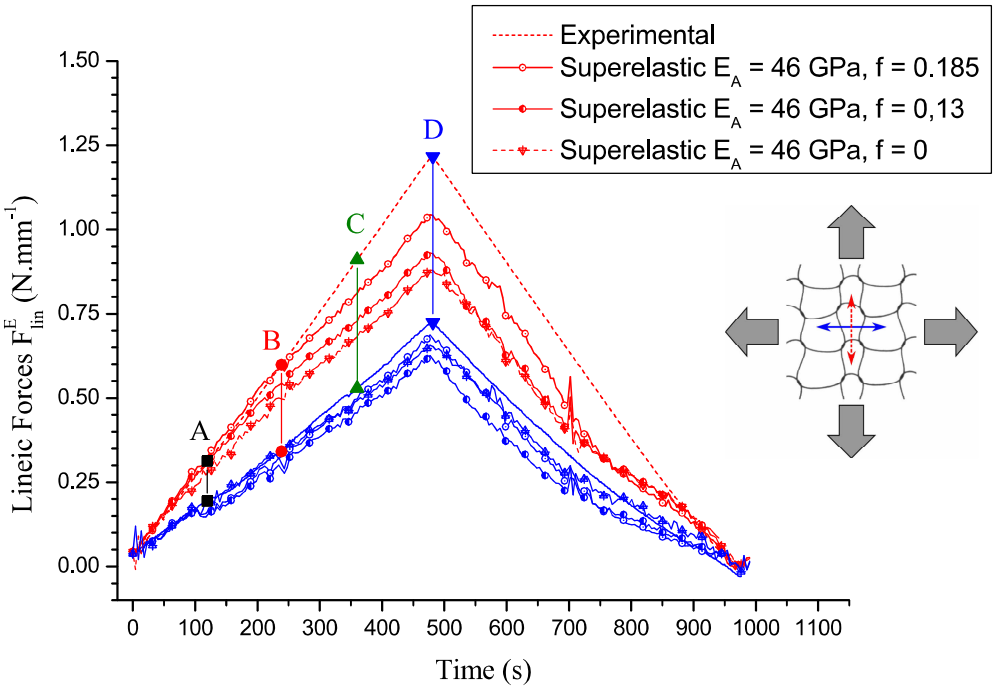

Figure V.45. Influence of the wire friction coefficient on the knit loop lineic forces response in biaxial tension.

coefficient as introduced previously (Section 4.2.3). The knit loop lineic force responses for such models are plotted alongside experimental results in Figure V.45.

The friction coefficient reduction induces the stitch softening, similarly as observed in uniaxial tension, yet with no sliding happening after step B previously identified (Section 4.3.1). No friction induces small oscillations at the loading start because of the lack of energy dissipation by friction and low dissipation due to the material hysteresis because of the low stress level in this time period. The maximum lineic force decreases with the friction coefficient, by 23.5% and 28% in the wale direction, and 14% and 9.5% in course direction, for $f = 0.13$ and $f = 0$ respectively.

As for the austenite Young's modulus, friction coefficient variation induces initial geometry shifts after the second pre-loading step, modifying the lineic force response with the application of the experimental stitch kinetic.

5 General conclusion

In this chapter, direct measurement of heat treated nitinol wire-to-wire friction coefficient has been brought and validated through the numerical analysis of the influence of the coefficient on the stitch macroscopic behavior. The coefficient has been estimated at $f = 0.185$, similar to the coefficient found in literature and identified on knitted NiTi textiles [50].

The knit loops dimensions have been analyzed thanks to the dedicated software developed in-house and a mean representative loop geometry has been determined, with a relatively constant standard deviation in absolute value, equal to $0.15 \pm 4mm$, for all dimensional parameters. This constant standard deviation is yet to be understood, and potentially rises from manufacturing process precision.

Table V.3. Summary of parameters E_A and f influences depending on the loading case

	Uniaxial Wale			Uniaxial Course			Biaxial	
	F^y_{max}	H^y	ν_{yx}	F^x_{max}	H^x	ν_{xy}	F^x_{max}	F^y_{max}
E_A	+	+	- -	+	+	+	- -	- -
f	+++	++	- -	+	++	+++	-	++

The experimental setup, validated on soft silicone membranes in previous chapter, has been adapted to fit knitted textiles and allowed computing stitch geometry changes during loading, to verify concordance between the zone of interest and mean stitch strains, allowing the use of the homogenization method for numerical analysis. Boundary forces distributions have been measured and corner effects characterized. It has been shown that uniaxial tension offers poor boundary forces distribution with high standard deviation in central zone (27% for course-wise tension), and 3 external springs at each edge extremity off the mean value by a larger amount. The ratio $\left|\frac{T}{N}\right|$, however, has validated the hypothesis of negligible shear effects at the sample edges.

In biaxial tension, in another hand, boundary forces have been shown as highly uniform with 10% to 15% deviation on a single spring at each edge end, and less than 3% deviation on the remaining springs. However, biaxial tension tests on the textile shown the experimental setup limits by highlighting the dramatic difference between working area and zone of interest strains, removing the possibility to control the sample strains effectively.

The mean representative geometry has been imported in the finite element model, and the model has then been used to validate the use of a linear elastic material in order to optimize computational times (reduction by a factor 6) in uniaxial tension. This study has shown that such approximation yields confident results in uniaxial tension in the strains range obtained experimentally. The maximum Von Mises stress in the wire section along the curvilinear abscissa revealed the linear elastic material approach is validated even if local stresses highly surpass martensitic transformation stress σ_{ms}. The biaxial numerical results yet has depicted limits of such approximation as the linear elastic material overestimates 2.3 times experimental results at maximum strains. The Auricchio model however has been shown to be fitting experimental forces with a maximum error of 17% in the wale direction, and less than 3% in the course direction. Maximum Von Mises stress in the section has highlighted that a large length of the wire is transformed into martensite during such loading, explaining the important errors obtained with the elastic material. Yet, this finite elements analysis has shown that a very simple model, using beam elements approximation and simple material behavior, can be used to estimate the mechanical behavior of a knitted NiTi textile.

Finally, the finite elements model has been used to compute the influence of two key parameters on the knit loop macroscopic behavior, namely the austenite Young's modulus E_A and friction coefficient f, summed up in Table V.3. This study highlights the importance of friction in uniaxial tension (mainly in wale-wise tension) and the absence of structural hysteresis. This leads to the conclusion that, no matter the loading case, the wire-to-wire friction coefficient is more impacting on the knitted textile mechanical behavior than the austenite Young's modulus.

CHAPTER

VI Conclusion & discussion

1 Conclusion and improvements

1.1 Conclusion

In this work, a complete set of analysis tools has been proposed to provide a methodology to perform architectured material based on knitted NiTi textiles design. For the knitted NiTi textiles experimental characterization, an experimental setup to perform uniaxial and biaxial tests has been proposed, which also provides direct boundary forces distributions measurement. This setup has been inspired by studies performed on textiles as well as on soft polymers and biological membranes, as the textile overall mechanical behavior is similar to such materials. This setup aims at providing the sample with strain fields uniformity within the sample working area. To complement this experimental setup, the image analysis software developed computes the internal morphology of the textile and dimensions changes during loading. Then, based on the assumption of uniform knit loops dimensions and strain fields during tensile loading, a finite element model has been proposed using the homogenization method and a single knit loop geometry to compute the textile mechanical behavior. This model uses beam finite elements in order to reduce computation times as the wire diameter is small compared to its curvilinear length. The model is solve with the explicit method in order to be able to take into account for contact implying sliding between beam elements. Finally, in order to complete the model configuration, an experimental setup to compute the wire-to-wire friction coefficient has been developed. The value obtained after several measurements is averaged and implemented in the model. The mechanical behavior analysis of a knitted NiTi textile has then been performed with the methodology developed specifically in this work.

The macroscopic behavior obtained in uniaxial tension presents the characteristic anisotropy and large recoverable strains. The anisotropy is characterized by a lineic reaction force lower in the wale direction than in course direction. Recoverable strains of up to 32% have been achieved in uniaxial tension. The experimental analysis setup proposed allowed to perform boundary forces distributions direct measurement and orientation (normal and tangential) in order to verify uniaxial and biaxial tension hypotheses. This measurement also allows to quantify boundary effects and forces concentrations on the sample edges.

The image processing software developed for knitted textiles allowed to measure several knit loop parameters (dimensions and shape) and provided the knit loop mean representative geometry and standard deviation. The standard deviation associated with the mean value appeared of the same order of magnitude for every of the loop dimensions, requiring further study to analyze the origin of such value. The mean dimensions values and standard deviations have been studied throughout loading and revealed that no uniformization occurs during uniaxial and biaxial loading. It has been shown that, in course-wise tension, small shape and symmetry defects are the main reasons for knit loop deformed shape instability. Lastly, the knit loops dimensions allowed computing each loop strains along the x and y-axis, using the loop length and row spacing respectively. During loading, the knit loops strains uniformity has been evaluated with the corresponding standard deviation value and evolution. Uniaxial tensile tests present highly uniform knit loops strains, and such strains correspond to the global sample strains. These two observations imply that the homogenization method can be used numerically to model the sample mechanical behavior and extrapolate its behavior from a single knit loop.

The numerical analysis has then been performed on the knit loop representative geometry, using periodic boundary conditions in order to reproduce the behavior of a virtually infinite textile, and beam elements in order to reduce computational times and periodic boundary conditions enforcement complexity. The model has also been further simplified by using a simple linear elastic material behavior instead of a superelastic behavior model, in order to verify the possibility of further reducing calculation times. The kinematic boundary conditions have been implemented in the model to constrain the stitch strains, and the resulting mechanical behavior has been compared to experimental measurements. The model using linear elastic material behavior presents good agreement with experimental measurements in uniaxial tension. The analysis of the section maximum Von Mises stress along the wire curvilinear abscissa revealed that stress levels within the section are relatively low, and only locally exceeds the superelastic martensitic transformation stress σ_{Ms}. These low stresses levels explains the similar knit loop mechanical behavior when computed using linear elastic material or superelastic material. This simple finite element model thus provides precise evaluation of the knitted NiTi textile mechanical behavior, and can be used for early studies as a time saving method to refine the research domain, prior to use more complex yet more precise models.

Two preliminary studies have been presented to estimate the influence of two key parameters for knitted NiTi textiles, namely the austenite Young's modulus E_A and the heat-treated NiTi wires friction coefficient f. It has been shown that the austenite Young's modulus has a limited impact on the mechanical behavior of the textile, specially in biaxial tension. The friction coefficient f, however, plays an important role on the mechanical behavior of the knitted textile, even in biaxial tension where locking occurs directly at the beginning of the loading step. Hence, studies on the NiTi wires friction coefficient could valuable for knitted NiTi textiles studies.

1.2 Improvement perspectives

Biaxial tests on knitted textiles appear difficult to really control due to stitch deformations with the proposed hooking system. The local forces on the loop segments induced large concentrated bending on loop and thus large deviation of the global strain versus the mean loops strain. However, such defects may also be observed with other setups which use very local attachment technique. This study has thus brought to light such defects induced by the griping method and

particular precautions have to be taken for biaxial tests on knitted textiles. Those tests have to be performed by taking into account the difference between global and zone of interest strains, and the global strains measurement (grips or targets for the setup proposed) should not be used as the mean zone of interest strains.

The spring system also highlight difficulties to obtain uniform initial spring forces. Springs used for this setup were commercially provided with jointed coils, inducing an initial contraction forces, and their free length was low (25 mm). Hence, each spring has been elongated on a tensile machine up to a final free length of 150 mm. Yet, this elongation can not be performed with a high enough precision to allow for an initial free length to be comprised between 150 ± 0.25 mm. On top of such defect, the knit loop dimensions initial non-uniformity induces springs attachment point placement defects. Therefore, initial spring tension present strong heterogeneities, and few springs may be totally freely bent down or in the contrary stretch excessively. Therefore, a system providing adjustable initial spring tension could be developed to tune each spring initial tension to put every spring in a similar state before loading. Yet such system may not require to provide with precise tension measurement as the initial tension only aims at straightening springs at the initial state. Hence, such tension may be easily manually evaluated without the introduction of a too large initial tension.

During tests presented in this work, two camera were used to take pictures of the sample and setup, respectively. The two cameras may be replaced by a single one having large enough field of view, coupled with an high resolution (about 16 Mpx) to provide with the capability of tracking springs and grips target movements and knitted textile structure changes. Using only one camera reduces the complexity of the camera mounting system, camera coupling software and synchronization with the tensile machine recordings, and also reduces the overall data weight as each picture usually weight around 5 Mo. Yet, such camera may, to this day, still be expensive and not always available in laboratories. Furthermore, to perform targets tracking and knit morphology computation, two different contrast settings are used due to lighting and reflection problems. Hence, using a single camera implies to define for each test pictures the knit structure zone of interest and the target location to perform two black and white level treatment, leading to largely increased computation times.

In the present study, only a small part of the data available on test pictures have been used. The focus has been kep on knit loop dimensions and shape, but sliding distance, axial deformations, textile porosity/loop density, and few more can also be computed on the images. The image processing software developed for knitted textiles can also be further improved to give access to even more precise information such as wire initial curvature and change during loading for example, and could be used as well on composites using knitted textiles as reinforcement, as long as the matrix offers enough transparency and low diffraction to analyze the textile deformation mechanisms while locked inside the matrix.

The finite element model uses an idealized knit loop geometry computed from the textile knit loops mean dimensions. It has been shown that associated standard deviation are greater than 5% (commonly assumed satisfactory deviation). Therefore, testing different knit loop geometries could lead to different mechanical behaviors, and testing real knit loop geometries may be important. To compute the real knit loops geometry in 3D, X-ray tomography could be used. To further improve the model precision, more complex material behavior model could be implemented in place of the Aurrichio behavior model.

2 Discussion and perspectives

The study presented in this thesis has only skimmed over the knitted textiles mechanical behavior comprehension. Further studies are required to complete the knowledge base on such particular textiles in order to propose concrete applications, such as the effect of the initial knit loop dimensions over the mechanical behavior of the sample or the characterization of shape-setting method in order to provide reproducible stitch dimensions after heat treatment. In such purpose, the analysis method has been presented and validated in this work to prepare future studies.

The huge interest of knitted textiles resides the wire high mobility within the structure, which is responsible for the textile high recoverable strain and damping capability, mainly. Therefore, when used as composite reinforcement, the matrix blocks the wire movement and negates such properties. The remaining aspect is the high formability and the ability to produce complex preforms without any steps subsequent to knitting. After molding is completed, the textile looses its special abilities (loss of mobility) and its mechanical behavior should become close to woven textiles, *i.e.* similar to a wire in simple tension. In such case, the cohesion between the matrix and the textile plays an important role as the wire bending may induce strong shear stresses and cut through the matrix.

In the case of biomedical use of knitted NiTi textiles, the question of organism protection may be asked. Indeed, nickel-titanium alloys may release nickel atoms in the organism which are highly allergen and can even be hazardous for the patient's health. Furthermore, chemical attacks may appears when the alloy is exposed to acidic environment such as gastric fluids (esophageal stents, for example), inducing premature damaging and braking of the implant. Finally, when aiming at using the shape-memory capacity of the alloy, the heating of the implant can prove tricky as biological tissues start to be severally damage when the temperature rises above 42^oC. Hence, coating the wire in a neutral material to provide the implant with a chemical and thermal shield can be performed. Yet, such coating implies a strong modification of the wire to wire friction coefficient, and therefore can modify greatly the knitted textile mechanical properties. And as the frictional forces rise, when sliding occurs, high tangential forces at the contact layer between the NiTi wire and its coating arise and may fracture the bond. Deep studies on the bond between nickel-titanium wires and polymer coating have to be perform to investigate the bond strength and its possible damage under such loading conditions (Thierry Rey thesis work (2014)).

Bioresorbable polymers have already been used to produce knitted stents allowing easy manufacture at low costs, controlled anisotropy and mechanical behavior, and easy removing operation [49]. Thanks to the analysis tools proposed in the present study, stents produced purely from bioresorbable wires could be developed, their mechanical properties tuned to fit the artery which they will be fitted in, to provide implants which degrades within the patient's body to remove the need of post-operative intervention to remove the stent.

Bibliography

[1] T. Alonso, "Caractérisation par essais DMA et optimisation du comportement thermomécanique de fils de NiTi - Application à une aiguille médicale déformable," PhD Thesis, Université Grenoble Alpes, 2015.

[2] D. J. Spencer, *Knitting Technology - A comprehensive handbook and practical guide*. Woodhead Publishing Limited, 2001.

[3] B. Eberhardt and a. Weber, "A particle system approach to knitted textiles," *Comput. Graph.*, vol. 23, no. 4, pp. 599–606, aug 1999. [Online]. Available: http://linkinghub.elsevier.com/retrieve/pii/S0097849399000771

[4] W. G. Klein, "Stress-Strain Response of Fabrics Under Two-Dimensional Loading: Part I: The RL Biaxial Tester," *Text. Res. J.*, vol. 29, no. 10, pp. 816–821, 1959.

[5] C. H. Reichardt, H. K. Woo, and D. J. Montgomery, "A two-dimensional load-extension tester for woven fabrics," *Text. Res. J.*, vol. 23, no. 424, 1953.

[6] L. Treloar, "Stresses and birefringence in rubber subjected to general homogeneous strain," *Proc. Phys. Soc.*, vol. 10, no. 2, pp. 135 – 144, 1948. [Online]. Available: http://iopscience.iop.org/0959-5309/60/2/303

[7] M. S. Sacks, "Biaxial mechanical evaluation of planar biological materials," *J. Elast. Phys. Sci. solids*, vol. 61, pp. 199–246, 2001. [Online]. Available: http://link.springer.com/article/10.1023/A:1010917028671

[8] E. C. Bass, F. A. Ashford, M. R. Segal, and J. C. Lotz, "Biaxial testing of human annulus fibrosus and its implications for a constitutive formulation." *Ann. Biomed. Eng.*, vol. 32, no. 9, pp. 1231–42, sep 2004. [Online]. Available: http://www.ncbi.nlm.nih.gov/pubmed/15493511

[9] Z. Xia, C. Zhou, Q. Yong, and X. Wang, "On selection of repeated unit cell model and application of unified periodic boundary conditions in micro-mechanical analysis of composites," *Int. J. Solids Struct.*, vol. 43, no. 2, pp. 266–278, jan 2006. [Online]. Available: http://linkinghub.elsevier.com/retrieve/pii/S0020768305001460

[10] T. Yoneyama and S. Miyazaki, *Shape memory alloys for biomedical applications*, T. Yoneyama and S. Miyazaki, Eds. Cambridge, England: Woodhead Publishing Limited, 2009.

[11] T. Duerig, A. Pelton, and C. Trepanier, "The Thermal Transformation from Austenite to Martensite and the Origin of Shape Memory," in *Nitinol*, T. Duerig, A. Pelton, and C. Trepanier, Eds. ASM International, 2010, vol. 1, no. 1, ch. 2, pp. 1–38.

[12] P. K. Kumar and D. C. Lagoudas, "Introduction to Shape Memory Alloys," in *Shape Mem. Alloy.*, D. C. Lagoudas, Ed. Boston, MA: Springer US, 2008, vol. 1, ch. 1, pp. 1 – 51. [Online]. Available: http://link.springer.com/10.1007/978-0-387-47685-8

[13] K. Otsuka and X. Ren, "Physical metallurgy of TiâĂŞNi-based shape memory alloys," *Prog. Mater. Sci.*, vol. 50, no. 5, pp. 511–678, jul 2005. [Online]. Available: http://linkinghub.elsevier.com/retrieve/pii/S0079642504000647

[14] M. H. Elahinia, M. Hashemi, M. Tabesh, and S. B. Bhaduri, "Manufacturing and processing of NiTi implants: A review," *Prog. Mater. Sci.*, vol. 57, no. 5, pp. 911–946, jun 2012. [Online]. Available: http://linkinghub.elsevier.com/retrieve/pii/S0079642511001058

[15] P.-Y. Manach and D. Favier, "Origin of the two-way memory effect in NiTi shape memory alloys," *Scr. Metall. Mater.*, vol. 28, pp. 1417 – 1421, 1993.

[16] T. W. Duerig and K. Bhattacharya, "The Influence of the R-Phase on the Superelastic Behavior of NiTi," *Shape Mem. Superelasticity*, vol. 1, no. 2, pp. 153–161, 2015. [Online]. Available: http://link.springer.com/10.1007/s40830-015-0013-4

[17] A. R. Horrocks and S. C. Anand, *Handbook of technical textiles*. Cambridge: Woodhead Publishing Limited, 2000.

[18] B. Bekisli and H. F. Nied, "Mechanical Properties of Thermoformed Structures with Knitted Reinforcement," in *RTS 2009 - Int. Conf. Plasturgy*. Albi: Ecoles des Mines d'Albi, 2009.

[19] Z. M. Huang and S. Ramakrishna, "Micromechanical modeling approaches for the stiffness and strength of knitted fabric composites: a review and comparative study," *Compos. Part A Appl. Sci. Manuf.*, vol. 31, no. 5, pp. 479–501, may 2000. [Online]. Available: http://linkinghub.elsevier.com/retrieve/pii/S1359835X99000834

[20] L. Heller, D. Vokoun, and P. Šittner, "From simple thin Nitinol filaments towards complex functional NiTi textiles," in *Cimtec*, 2012, pp. 1–34.

[21] L. Heller, B. Marvalova, J. Vlach, K. Janouchová, M. Syrovatkova, and J. Hanuš, "Vibration Problems ICOVP 2011," *Vib. Probl. ICOVP 2011*, vol. 139, pp. 393–398, 2011. [Online]. Available: http://link.springer.com/10.1007/978-94-007-2069-5

[22] K. H. Leong, S. Ramakrishna, Z. M. Z. Huang, and G. A. Bibo, "The potential of knitting for engineering compositesâĂŤa review," *Compos. Part A Appl. Sci. Manuf.*, vol. 31, no. 3, pp. 197–220, mar 2000. [Online]. Available: http://linkinghub.elsevier.com/retrieve/pii/S1359835X99000676

[23] M. Tercan, O. Asi, M. E. Yüksekkaya, and A. AktaÅ§, "Comparison of tensile properties of weft-knit 1ÃŮ1 rib glass/epoxy composites with a different location of layers," *Mater. Des.*, vol. 28, no. 7, pp. 2172–2176, jan 2007. [Online]. Available: http://linkinghub.elsevier.com/retrieve/pii/S0261306906001865

[24] G. Dusserre, "Modélisation du comportement mécanique des composites à renforts tricotés: influence de la contexture," in *GDR-WEEK 2012*, 2012.

[25] V. Leung, H. Yang, and F. Ko, *Biomedical Textiles for Orthopaedic and Surgical Applications*, T. Blair, Ed. Woodhead Publishing Limited, 2015. [Online]. Available: http://www.sciencedirect.com/science/article/pii/B9781782420170000052

[26] N. V. Padaki, R. Alagirusamy, and B. S. Sugun, "Knitted Preforms for Composite Applications," *J. Ind. Text.*, vol. 35, no. 4, pp. 295–321, oct 2006. [Online]. Available: http://jit.sagepub.com/cgi/doi/10.1177/1528083706060784

[27] Y. Aimene, B. Hagege, F. Sidoroff, E. Vidal-Sallé, P. Boisse, and S. Dridi, "Hyperelastic approach for composite reinforcement forming simulations," *Int. J. Mater. Form.*, vol. 1, no. SUPPL. 1, pp. 811–814, 2008.

[28] F. Dumont, C. Weimer, D. Soulat, J. Launay, S. Chatel, and S. Maison-Le-Poec, "Composites preforms simulations for helicopters parts," *Int. J. Mater. Form.*, vol. 1, no. SUPPL. 1, pp. 847–850, 2008.

[29] A. Cherouat and H. Borouchaki, "Present State of the Art of Composite Fabric Forming: Geometrical and Mechanical Approaches," *Materials (Basel).*, vol. 2, no. 4, pp. 1835–1857, nov 2009. [Online]. Available: http://www.mdpi.com/1996-1944/2/4/1835/

[30] A. Bansiddhi, T. D. Sargeant, S. I. Stupp, and D. C. Dunand, "Porous NiTi for bone implants: a review." *Acta Biomater.*, vol. 4, no. 4, pp. 773–82, jul 2008. [Online]. Available: http://www.pubmedcentral.nih.gov/articlerender.fcgi?artid=3068602&tool=pmcentrez&rendertype=abstract

[31] S. Wu, X. Liu, T. Hu, P. K. Chu, J. P. Y. Ho, Y. L. Chan, K. W. K. Yeung, C. L. Chu, T. F. Hung, K. F. Huo, C. Y. Chung, W. W. Lu, K. M. C. Cheung, and K. D. K. Luk, "A biomimetic hierarchical scaffold: Natural growth of nanotitanates on three-dimensional microporous Ti-based metals," *Nano Lett.*, vol. 8, no. 11, pp. 3803–3808, 2008.

[32] M. Duhovic and D. Bhattacharyya, "Simulating the deformation mechanisms of knitted fabric composites," *Compos. Part A Appl. Sci. Manuf.*, vol. 37, no. 11, pp. 1897–1915, nov 2006. [Online]. Available: http://linkinghub.elsevier.com/retrieve/pii/S1359835X06000133

[33] Y. Chan-vili, "Designing smart textiles based on shape memory materials," Doctoral Thesis, Heriot-Watt University, 2004. [Online]. Available: http://ethos.bl.uk/OrderDetails.do?uin=uk.bl.ethos.444799

[34] ——, "Investigating Smart Textiles Based on Shape Memory Materials," *Text. Res. J.*, vol. 77, no. 5, p. 290, may 2007. [Online]. Available: http://trj.sagepub.com/cgi/doi/10.1177/0040517507078794

[35] G. K. Stylios, Y. Chan-vili, T. Wan, S. Lam, and P. Tang, "Engineering textile aesthetics by shape and colour changing materials," in *5 th World Text. Conf. AUTEX*, no. June, Portorož, 2005, pp. 29–34.

[36] R. C. Winchester and G. K. Stylios, "Designing knitted apparel by engineering the attributes of shape memory alloy," *Int. J. Cloth. Sci. Technol.*, vol. 15, no. 5, pp. 359–366, 2003. [Online]. Available: http://www.emeraldinsight.com/10.1108/09556220310492624http://www.emeraldinsight.com/journals.htm?articleid=875550&show=abstract

[37] G. Dayananda, "NiTi Super Elastic Shape Memory Alloys for Energy Dissipation in Smart Systems for Aerospace Applications," Doctorate Thesis, Mangalore University, 2008. [Online]. Available: http://nal-ir.nal.res.in/id/eprint/9889

[38] L. Heller, A. Kujawa, P. Šittner, M. Landa, P. Sedlák, and J. Pilch, "Quasistatic and dynamic functional properties of thin superelastic NiTi wires," *Eur. Phys. J. Spec. Top.*, vol. 158, no. 1, pp. 7–14, may 2008. [Online]. Available: http://www.springerlink.com/index/10.1140/epjst/e2008-00646-6

[39] L. Heller, P. Šittner, J. Pilch, and M. Landa, "Factors Controlling Superelastic Damping Capacity of SMAs," *J. Mater. Eng. Perform.*, vol. 18, no. 5-6, pp. 603–611, feb 2009. [Online]. Available: http://link.springer.com/10.1007/s11665-009-9358-1

[40] R. Ellis, "Ballistic Impact Resistance of Graphite Epoxy Composites with Shape Memory Alloy and Extended Chain Polyethylene SpectraâĎć Hybrid Components," Master Thesis, Virginia Polytechnic Institute and State University, 1996. [Online]. Available: http://scholar.lib.vt.edu/theses/available/etd-23521427119653610/unrestricted/etd.pdf?q=graphiteepoxy

[41] F. Carpi, M. Pucciani, and D. D. Rossi, "Mechanical Models and Actuation Technologies for Active Fabrics: A Brief Survey of the State of the Art," *Multifunct. Barriers Flex. ...*, 2007. [Online]. Available: http://link.springer.com/chapter/10.1007/978-3-540-71920-5_9

[42] S. Vasile, K. E. Grabowska, I. L. Ciesielska-wróbel, and J. Githaiga, "Analysis of Hybrid Woven Fabrics with Shape Memory Alloys Wires Embedded," *FIBRES Text. East. Eur.*, vol. 18, no. 1, pp. 64–69, 2010.

[43] J. Pilch, "INVESTIGATION OF FUNCTIONAL PROPERTIES OF THIN NITI FILAMENTS FOR APPLICATIONS IN SMART STRUCTURES AND HYBRID TEXTILES," Ph.D. dissertation, BRNO UNIVERSITY OF TECHNOLOGY, 2011.

[44] Y. Li, L. Yeung, S. Chung, and J. Hu, "EVALUATION METHOD OF INNOVATIIVE SHAPE MEMORY FABRICS," pp. 1–10.

[45] J. Spillner, A. Goetzenich, A. Amerini, O. Holtmannspotter, T. Deichmann, C. Schmitz, R. Autschbach, and G. Dohmen, "New sutureless 'atrial- mitral-valve prosthesis' for minimally invasive mitral valve therapy," *Text. Res. J.*, vol. 81, no. 2, pp. 115–121, aug 2010. [Online]. Available: http://trj.sagepub.com/cgi/doi/10.1177/0040517510377825

[46] H. van der Merwe, B. Daya Reddy, P. Zilla, D. Bezuidenhout, and T. Franz, "A computational study of knitted Nitinol meshes for their prospective use as external vein

reinforcement." *J. Biomech.*, vol. 41, no. 6, pp. 1302–1309, jan 2008. [Online]. Available: http://www.ncbi.nlm.nih.gov/pubmed/18328487

[47] P. Zilla, L. Moodley, M. F. Wolf, D. Bezuidenhout, M. S. Sirry, N. Rafiee, W. Lichtenberg, M. Black, and T. Franz, "Knitted nitinol represents a new generation of constrictive external vein graft meshes," *J. Vasc. Surg.*, vol. 54, no. 5, pp. 1439–1450, 2011. [Online]. Available: http://linkinghub.elsevier.com/retrieve/pii/S0741521411010901

[48] C. Rice, "SHAPE MEMORY ALLOYS, APPLICATIONS," *Encycl. Smart Mater.*, pp. 921 – 936, 1997.

[49] T. Tokuda, Y. Shomura, N. Tanigawa, S. Kariya, A. Komemushi, H. Kojima, and S. Sawada, "Mechanical characteristics of composite knitted stents." *Cardiovasc. Intervent. Radiol.*, vol. 32, no. 5, pp. 1028–32, sep 2009. [Online]. Available: http://www.ncbi.nlm.nih.gov/pubmed/19506947

[50] J. Abel, J. Luntz, and D. Brei, "A two-dimensional analytical model and experimental validation of garter stitch knitted shape memory alloy actuator architecture," *Smart Mater. Struct.*, vol. 21, no. 8, p. 085011, aug 2012. [Online]. Available: http://iopscience.iop.org/0964-1726/21/8/085011http://stacks.iop.org/0964-1726/21/i=8/a=085011?key=crossref.9982d5843b3387ccd12cc8debc05d814

[51] B. Holschuh and E. Obropta, "Materials and textile architecture analyses for mechanical counter-pressure space suits using active materials," *Am. Inst. Aeronaut. Astronaut.*, pp. 1–17, 2012. [Online]. Available: http://arc.aiaa.org/doi/pdf/10.2514/6.2012-5206

[52] M. Ashby, T. Evans, N. Fleck, J. Hutchinson, H. Wadley, and L. Gibson, *Metal Foams: A Design Guide*. Elsevier Science, 2000. [Online]. Available: https://books.google.fr/books?id=C0daIBo6LjgC

[53] O. Ozipek, E. Bozdag, and E. Sunbuloglu, "Biaxial Testing of Fabrics-A Comparison of Various Testing Methodologies," *World Acad. Sci. Eng. Technol.*, vol. 78, pp. 652–657, 2013. [Online]. Available: http://www.waset.org/publications/1225

[54] T. Komatsu, M. Takatera, S. Inui, and Y. Shimizu, "Relationship Between Uniaxial and Strip Biaxial Tensile Properties of Fabrics," *Text. Res. J.*, vol. 78, no. 3, pp. 224–231, mar 2008. [Online]. Available: http://trj.sagepub.com/cgi/doi/10.1177/0040517507083439

[55] A. S. Kaddour, M. J. Hinton, and P. D. Soden, "Behaviour of $\pm 45^o$ glass/epoxy filament wound composite tubes under quasi-static equal biaxial tension-compression loading: Experimental results," *Compos. Part B Eng.*, vol. 34, no. 8, pp. 689–704, 2003.

[56] A. A. Alhayani, J. Rodríguez, and J. Merodio, "Competition between radial expansion and axial propagation in bulging of inflated cylinders with application to aneurysms propagation in arterial wall tissue," *Int. J. Eng. Sci.*, vol. 85, pp. 74–89, 2014. [Online]. Available: http://dx.doi.org/10.1016/j.ijengsci.2014.08.008

[57] G. Machado, G. Chagnon, and D. Favier, "Induced anisotropy by the Mullins effect in filled silicone rubber," *Mech. Mater.*, vol. 50, pp. 70–80, 2012. [Online]. Available: http://dx.doi.org/10.1016/j.mechmat.2012.03.006

[58] T. Tsakalakos, "The bulge test: a comparison of theory and experiment for isotropic and anisotropic films," *Thin Solid Films*, vol. 75, pp. 293–305, 1981.

[59] L. Meunier, G. Chagnon, D. Favier, L. Orgéas, and P. Vacher, "Mechanical experimental characterisation and numerical modelling of an unfilled silicone rubber," *Polym. Test.*, vol. 27, no. 6, pp. 765–777, 2008.

[60] D. A. Arellano Escarpita, D. Cardenas, H. Elizalde, R. Ramirez, and O. Probst, "Biaxial Tensile Strength Characterization of Textile Composite Materials," in *Compos. Their Prop.*, aug 2012.

[61] S. V. Lomov, M. Barburski, T. Stoilova, I. Verpoest, R. Akkerman, R. Loendersloot, and R. Thije, "Carbon composites based on multiaxial multiply stitched preforms. Part 3: Biaxial tension, picture frame and compression tests of the preforms," *Compos. Part A Appl. Sci. Manuf.*, vol. 36, no. 9, pp. 1188–1206, sep 2005. [Online]. Available: http://linkinghub.elsevier.com/retrieve/pii/S1359835X05000527

[62] A. Smits, D. Van Hemelrijck, T. P. Philippidis, and A. Cardon, "Design of a cruciform specimen for biaxial testing of fibre reinforced composite laminates," *Compos. Sci. Technol.*, vol. 66, no. 7-8, pp. 964–975, jun 2006. [Online]. Available: http://linkinghub.elsevier.com/retrieve/pii/S0266353805003064

[63] S. Demmerle and J. P. Boehler, "Optimal design of biaxial tensile specimens," *J. Mech. Phys. Solids*, vol. 41, no. 1, pp. 143–181, 1993.

[64] A. Hannon and P. Tiernan, "A review of planar biaxial tensile test systems for sheet metal," *J. Mater. Process. Technol.*, vol. 198, no. 1-3, pp. 1–13, mar 2008. [Online]. Available: http://linkinghub.elsevier.com/retrieve/pii/S0924013607009533

[65] V. Carvelli, C. Corazza, and C. Poggi, "Mechanical modelling of monofilament technical textiles," *Comput. Mater. Sci.*, vol. 42, no. 4, pp. 679–691, jun 2008. [Online]. Available: http://linkinghub.elsevier.com/retrieve/pii/S0927025607003072

[66] A. Willems, S. V. Lomov, I. Verpoest, and D. Vandepitte, "Optical strain fields in shear and tensile testing of textile reinforcements," *Compos. Sci. Technol.*, vol. 68, no. 3-4, pp. 807–819, mar 2008. [Online]. Available: http://linkinghub.elsevier.com/retrieve/pii/S0266353807003405

[67] H. W. Reinhardt, "On the biaxial testing and strength of coated fabrics," *Exp. Mech.*, vol. 16, no. 2, pp. 71–74, feb 1976. [Online]. Available: http://link.springer.com/10.1007/BF02328607

[68] J. P. Boehler, S. Demmerle, and S. Koss, "A New Direct Biaxial Testing Machine for Anisotropic Materials," *Exp. Mech.*, vol. 34, no. 1, pp. 1–9, 1994.

[69] K. Buet-Gautier and P. Boisse, "Experimental analysis and modeling of biaxial mechanical behavior of woven composite reinforcements," *Exp. Mech.*, vol. 41, no. 3, pp. 260–269, sep 2001. [Online]. Available: http://link.springer.com/10.1007/BF02323143

[70] M. Brieu, J. Diani, and N. Bhatnagar, "A New Biaxial Tension Test Fixture for Uniaxial Behavior of Rubber-like Materials," *J. Test. Eval.*, vol. 35, no. 4, pp. 1 – 9, 2007.

[71] V. Quaglini, C. Corazza, and C. Poggi, "Experimental characterization of orthotropic technical textiles under uniaxial and biaxial loading," *Compos. Part A Appl. Sci. Manuf.*, vol. 39, no. 8, pp. 1331–1342, aug 2008. [Online]. Available: http://linkinghub.elsevier.com/retrieve/pii/S1359835X0700125X

[72] E. Lamkanfi, W. Van Paepegem, and J. Degrieck, "Shape optimization of a cruciform geometry for biaxial testing of polymers," *Polym. Test.*, vol. 41, pp. 7–16, 2015. [Online]. Available: http://www.sciencedirect.com/science/article/pii/S0142941814002189

[73] C. Galliot and R. Luchsinger, "A simple model describing the non-linear biaxial tensile behaviour of PVC-coated polyester fabrics for use in finite element analysis," *Compos. Struct.*, pp. 1–25, 2009. [Online]. Available: http://www.sciencedirect.com/science/article/pii/S0263822309001172

[74] R. J. Basset, R. Postle, and N. Pan, "Experimental Methods for Measuring Fabric Mechanical Properties: A Review and Analysis," *Text. Res. J.*, vol. 69, no. 11, pp. 866–875, 1999.

[75] G. D. O'Connell, S. Sen, and D. M. Elliott, "Human annulus fibrosus material properties from biaxial testing and constitutive modeling are altered with degeneration." *Biomech. Model. Mechanobiol.*, vol. 11, no. 3-4, pp. 493–503, mar 2012. [Online]. Available: http://www.pubmedcentral.nih.gov/articlerender.fcgi?artid=3500512&tool=pmcentrez&rendertype=abstract

[76] K. L. Billiar and M. S. Sacks, "Biaxial mechanical properties of the natural and glutaraldehyde treated aortic valve cusp–Part I: Experimental results." *J. Biomech. Eng.*, vol. 122, no. 1, pp. 23–30, feb 2000. [Online]. Available: http://www.ncbi.nlm.nih.gov/pubmed/10790826

[77] R. J. Basset, R. Postle, and N. Pan, "Grip Point Spacing Along the Edges of an Anisotropic Fabric Sheet in a Biaxial Tensile Test," *Polym. Compos.*, vol. 20, no. 2, pp. 305 – 313, 1999.

[78] Y. Luo and I. Verpoest, "Biaxial tension and ultimate deformation of knitted fabric reinforcements," *Compos. Part A Appl. Sci. Manuf.*, vol. 33, no. 2, pp. 197–203, feb 2002. [Online]. Available: http://linkinghub.elsevier.com/retrieve/pii/S1359835X01001063

[79] S. V. Lomov, M. Moesen, R. Stalmans, G. Trzcinski, J. Van Humbeeck, and I. Verpoest, "Finite element modelling of SMA textiles: superelastic behaviour," *J. Text. Inst.*, vol. 102, no. 3, pp. 232–247, mar 2011. [Online]. Available: http://www.tandfonline.com/doi/abs/10.1080/00405001003696464

[80] M. S. Sacks and W. Sun, "Multiaxial mechanical behavior of biological materials." *Annu. Rev. Biomed. Eng.*, vol. 5, pp. 251–84, jan 2003. [Online]. Available: http://www.ncbi.nlm.nih.gov/pubmed/12730082

[81] T. Ghosh, "Apparatus and method for biaxial tensile testing of membrane materials," pp. 1 – 24, 2002. [Online]. Available: http://www.google.com/patents/US6487902

[82] M. Zemánek, J. Burša, and M. Děták, "Biaxial tension tests with soft tissues of arterial wall," *Eng. Mech.*, vol. 16, no. 1, pp. 3–11, 2009. [Online]. Available: http://dlib.lib.cas.cz/5251/

[83] A. Eilaghi, J. G. Flanagan, G. W. Brodland, and C. R. Ethier, "Strain uniformity in biaxial specimens is highly sensitive to attachment details." *J. Biomech. Eng.*, vol. 131, no. 9, p. 091003, sep 2009. [Online]. Available: http://www.ncbi.nlm.nih.gov/pubmed/19725692

[84] G. M. Cooney, K. M. Moerman, M. Takaza, D. C. Winter, and C. K. Simms, "Uniaxial and biaxial mechanical properties of porcine linea alba." *J. Mech. Behav. Biomed. Mater.*, vol. 41, pp. 68–82, jan 2015. [Online]. Available: http://www.ncbi.nlm.nih.gov/pubmed/25460404

[85] G. A. V. Leaf and A. Glaskin, "The Geometry of a Plain Knitted Loop," *J. Text. Inst. Trans.*, vol. 46, no. 9, pp. T587–T605, sep 1955. [Online]. Available: http://www.tandfonline.com/doi/abs/10.1080/19447027.1955.10750345

[86] T. Wada, S. Hirai, T. Hirano, and S. Kawamura, "Modeling of Plain Knitted Fabrics for Their Deformation Control," in *Int. Conf. Robot. Autom.*, no. 1, Albuquerque, 1997, pp. 1960–1965.

[87] M. D. Araújo, R. Fangueiro, and H. Hong, "Modelling and simulation of the mechanical behaviour of weft-knitted fabrics for technical applications- Part II : 3D model based on the elastica theory," *AUTEX Res. J.*, vol. 3, no. 4, pp. 166 – 172, 2003.

[88] ——, "Modelling and simulation of the mechanical behaviour of weft-knitted fabrics for technical applications- Part III : 2D hexagonal FEA model with non-linear truss elements," *AUTEX Res. J.*, vol. 4, no. March, pp. 4–11, 2004.

[89] Ö. Demircan, A. R. Torun, T. Kosui, and A. Nakai, "Tensile Properties And Finite Element Modelling Of Biaxial Weft Knitted Composites," in *18TH Int. Conf. Compos. Mater.*, 2011, pp. 1–4.

[90] J. G. Stannard, J. M. Gau, and M. A. Hanna, "Comparative friction of orthodontic wires under dry and wet conditions," *Am. J. Orthod.*, vol. 89, no. 6, pp. 485 – 491, 1986.

[91] M. V. Alfonso, E. Espinar, J. M. Llamas, E. Rup??rez, J. M. Manero, J. M. Barrera, E. Solano, and F. J. Gil, "Friction coefficients and wear rates of different orthodontic archwires in artificial saliva," *J. Mater. Sci. Mater. Med.*, vol. 24, no. 5, pp. 1327–1332, 2013.

[92] W. Sun, M. S. Sacks, and M. J. Scott, "Effects of Boundary Conditions on the Estimation of the Planar Biaxial Mechanical Properties of Soft Tissues," *J. Biomech. Eng.*, vol. 127, no. 4, p. 709, 2005. [Online]. Available: http://biomechanical.asmedigitalcollection.asme.org/article.aspx?articleid=1414532

[93] G. Machado, G. Chagnon, and D. Favier, "Analysis of the isotropic models of the Mullins effect based on filled silicone rubber experimental results," *Mech. Mater.*, vol. 42, no. 9, pp. 841–851, 2010. [Online]. Available: http://dx.doi.org/10.1016/j.mechmat.2010.07.001

[94] T. Rey, G. Chagnon, J. B. Le Cam, and D. Favier, "Influence of the temperature on the mechanical behaviour of filled and unfilled silicone rubbers," *Polym. Test.*, vol. 32, no. 3, pp. 492–501, 2013.

[95] J. Gager and H. Pettermann, “Numerical homogenization of textile composites based on shell element discretization,” *Compos. Sci. Technol.*, vol. 72, no. 7, pp. 806–812, apr 2012. [Online]. Available: http://linkinghub.elsevier.com/retrieve/pii/S0266353812000681